Time-resolved measurements of shock-compressed matter using x-rays

by

Michael J. MacDonald

A dissertation submitted in partial fulfillment
of the requirements for the degree of
Doctor of Philosophy
(Applied Physics)
in The University of Michigan
2016

Doctoral Committee:

Professor R Paul Drake, Chair
Associate Research Scientist Paul A. Keiter
Professor Karl M. Krushelnick
David S. Montgomery, Los Alamos National Laboratory
Professor Theodore B. Norris

ACKNOWLEDGEMENTS

I would like to acknowledge my advisor, Professor R. Paul Drake, for introducing me to the field of high-energy-density physics and providing the connections that have enabled me to work at a number of facilities throughout my graduate studies. During this time, I was given the opportunity to collaborate with scientists around the world and participate in a wide range of experiments in the field. I would especially like to thank David Montgomery for teaching me a great deal about designing and executing experiments, and for his patience during our experiments at the Trident laser facility.

I am extremely grateful for the two years of my graduate studies I spent working at SLAC National Accelerator Laboratory in the High Energy Density Sciences group. In particular, I would like to thank Luke Fletcher and Siegfried Glenzer for their guidance and support during my time at SLAC.

I would also like to thank my thesis committee for taking the time to review my work and providing feedback to improve my dissertation.

Finally, I would also like to thank the National Science Foundation for granting me the Graduate Research Fellowship, which supported three years of my graduate work.

TABLE OF CONTENTS

LIST OF FIGURES

Figure

ABSTRACT

Time-resolved measurements of shock-compressed matter using x-rays

by

Michael J. MacDonald

Chair: R. Paul Drake

Thermonuclear fusion occurs at extremely high pressures and densities. Producing thermonuclear fusion in the laboratory requires a detailed understanding of material properties beyond the scope of condensed matter or classical plasma physics, requiring experimental data to improve models describing matter in these extreme states. This thesis reports the development of two improved methods to probe highly compressed matter using x-ray diagnostics.

The first method uses time-resolved x-ray diffraction to infer the stresses in compressed polycrystalline materials. X-ray diffraction is capable of measuring strain states and densities in shock-compressed materials with significantly higher accurately than existing shock timing and velocimetry diagnostics. The analysis discussed in this thesis calculates Debye-Scherrer diffraction patterns from highly stressed polycrystalline samples in the Reuss (iso-stress) limit. In this limit, elastic anisotropy and sample texture effects are directly modeled using elastic constants to calculate lattice strains for all initial crystallite orientations. Example diffraction patterns showing the effects of probing geometry, deviatoric stresses, and sample texture are presented to highlight the versatility of the technique. Finally, I present

the design of a recent experiment conducted at the Linac Coherent Light Source to measure the strength of polycrystalline diamond whose data can be analyzed using this technique.

The second method uses x-ray fluorescence (XRF) to measure density, ionization state populations, and electron temperature in shocked materials. Spatially resolved K-α intensity measurements enable measurements of ion density profiles. Ionization state distributions and electron temperatures are constrained by comparing K-α spectra to spectra from atomic-physics simulations using the computer code CRETIN. Analysis of experimental data from the Trident laser facility measuring Ti K-α emission spectra from shock-compressed foams demonstrates the use of the technique. This work shows that XRF spectroscopy is a useful technique to complement prior diagnostics to make equation of state measurements of shocked materials containing a suitable tracer element.

CHAPTER I

Introduction

Matter exists at a vast range of densities and temperatures throughout the universe. Familiar solids and liquids are typically at densities on the order of 1 g/cm^3 and temperatures of a few hundred Kelvin. A large fraction of the interstellar medium contains only a few particles per cubic centimeter at temperatures of a fraction of an electron volt [6]. The core of the sun is at a temperature of 15 million Kelvin and has a density of 150 g/cm^3 [7]. Theoretical models have been developed to describe different states of matter based on the physical processes that determine their properties. For example, matter can be classified into groups by comparing the kinetic or potential energies of the particles in the system. Condensed matter physics describes typical solids and liquids, where potential energies dominate. In contrast, plasma physics concerns itself with the opposite case, where kinetic energies are large compared to potential energies and atoms are at least partially ionized. The intermediate states, where kinetic and potential energies are comparable, demand more sophisticated theoretical descriptions. Further development of theoretical models and validation of simulation codes require improved experimental techniques to study these conditions. This thesis reports on experimental methods to probe highly compressed matter using x-ray diagnostics.

1.1 Warm dense matter and high-energy-density physics

Warm dense matter (WDM) is a state of matter that is too hot to be considered condensed matter and too dense to be modeled by classical plasma physics. WDM exists in astrophysical bodies, is created in energetic astrophysical events, and can be produced on Earth in high-energy-density (HED) physics experiments. HED is generally defined by pressures above 1 Mbar, or one million times atmospheric pressure, which can also be written as an energy density of 10^{11} J/m^3. WDM exists in a state of partial ionization with significant ion-ion coupling, where thermal, Coulomb, and Fermi energies are comparable. Although the conditions of WDM are not present in everyday life, understanding the physics governing the regime is important to accurately model inertial confinement fusion implosions [8], planetary interiors [9], and the origin of planetary magnetic fields [10].

Two parameters are useful in quantifying the relative importance of internal energies in systems to determine which theoretical models are applicable: the Coulomb coupling parameter and degeneracy parameter. The Coulomb coupling parameter, Γ_{ee}, gives the ratio of the Coulomb energy (E_C) to the thermal energy

$$\Gamma_{ee} = \frac{E_C}{k_B T}, \quad E_C = \frac{e^2}{4\pi\epsilon_0 r_s} \tag{1.1}$$

where $r_s = (4\pi n_e/3)^{-1/3}$ is the Wigner-Seitz radius, which gives the mean separation of free electrons, n_e is free electron density, T is temperature, k_B is the Boltzmann constant, e is the elementary charge, and ϵ_0 is the vacuum permittivity. When $\Gamma_{ee} \gg 1$ the Coulomb energy dominates and the system can be considered cold, while if $\Gamma_{ee} \ll 1$ the thermal energy dominates and the system is weakly coupled.

The degeneracy parameter, Θ, is given by the ratio of the thermal energy and the Fermi energy (ϵ_F)

$$\Theta = \frac{k_B T}{\epsilon_F}, \quad \epsilon_F = \frac{\hbar^2}{2m_e}\left(3\pi^2 n_e\right)^{2/3} \tag{1.2}$$

where $\hbar$ is the reduced Planck constant and m_e is the electron mass. The degeneracy parameter is closely related to the deBroglie wavelength, λ_{dB} of thermal electrons in the system, given by

$$\lambda_{dB} = \frac{\hbar}{\sqrt{2m_e k_B T}}. \tag{1.3}$$

When $\Theta \gg 1$ the deBroglie wavelength of the electrons is much less than the average spacing of the ions and the system is non-degenerate. If $\Theta >> 1$ the deBroglie wavelength is large compared to the average interatomic spacing, resulting in significant overlap of the electron wave functions and a highly-degenerate system. Using these two parameters, we can loosely define WDM by requiring Γ_{ee} and Θ are both near unity.

A characteristic property of an ideal plasma its ability to screen electromagnetic fields as the free charges in plasmas naturally redistribute themselves to cancel the fields. Plasmas screen fields at a length scale quantified by the Debye length

$$\lambda_D = \sqrt{\frac{\epsilon_0 k_B T}{n_e e^2}}. \tag{1.4}$$

Effective screening of electromagnetic fields requires the redistribution of a large number of charges. If a small number of charges are present in the volume of a sphere on the scale of the Debye sphere, fields cannot be effectively screened and long-range order can arise in the system. This condition requires $n_e \lambda_D^3 \gg 1$, or

$$n_e \ll \left(\frac{\epsilon_0 k_B T}{e^2}\right)^3, \tag{1.5}$$

which is fulfilled for ideal plasmas at high temperatures and low densities, but is

often not the case in WDM. For this reason, long-range order and collective effects can play a significant role in the dynamics of WDM.

1.2 Fusion energy

Nearly all life on Earth depends on energy from the Sun, whether in the form of direct energy conversion in the case of photosynthesis in plants or by consuming other living organisms. The amount of energy received by the Earth from the Sun is approximately 1360 W/cm^2 [11]. After accounting for absorption and scattering in the atmosphere, this corresponds to a total power received by the Earth of approximately 89,000 TW. Assuming a global energy usage of 105,000 TWh per year, the Sun provides enough power for an entire year in under an hour and a half. A great deal of effort has gone into harnessing this energy using solar panels and thermal conversion. An alternative to capturing the energy released by the Sun is to produce fusion power directly by means of controlled thermonuclear fusion reactions.

Thermonuclear fusion occurs when the short-range attraction of the strong nuclear force overcomes electrostatic repulsion of two nuclei. Overcoming this repulsion, known as the Coulomb barrier, requires the plasma to be extremely well confined. The deuterium-tritium (DT) fusion cycle has the lowest confinement threshold and is thus the focus of nearly all major experimental fusion power efforts. The three relevant fusion reactions in a DT cycle are

$$\mathrm{D} + \mathrm{T} \rightarrow {}^4\mathrm{He}\ (3.5\ \mathrm{MeV}) + \mathrm{n}\ (14.1\ \mathrm{MeV}) \tag{1.6}$$

$$\mathrm{D} + \mathrm{D} \rightarrow {}^3\mathrm{He}\ (0.82\ \mathrm{MeV}) + \mathrm{n}\ (2.45\ \mathrm{MeV}) \tag{1.7}$$

$$\mathrm{D} + \mathrm{D} \rightarrow \mathrm{T}\ (1.01\ \mathrm{MeV}) + \mathrm{H}\ (3.02\ \mathrm{MeV}). \tag{1.8}$$

The first reaction is the primary source of energy, while the latter two will also occur

in a burning DT plasma. The majority of the energy released in the DT fusion cycle is in the form of energetic neutrons. Because neutrons do not have electric charge, extracting this energy requires a method to convert their kinetic energy to heat, which can be used to generate power with a steam turbine.

Another interesting fusion cycle is

$$\mathrm{D} + {}^{3}\mathrm{He} \rightarrow {}^{4}\mathrm{He}\ (3.6\ \mathrm{MeV}) + \mathrm{H}\ (14.7\ \mathrm{MeV}), \tag{1.9}$$

where the two products of the fusion event are both charged particles. Energy extraction from charged particles does not require the use of a heat cycle, significantly improving power conversion efficiency [12].

The majority of experimental efforts to achieve controlled thermonuclear fusion fall into one of two categories: inertial confinement fusion (ICF) or magnetic confinement fusion (MCF). ICF uses a spherical implosion to rapidly compress the fuel, initiating a fusion reaction in the central hotspot when the material converges at the center of the sphere. MCF reactors create a steady-state plasma confined using powerful magnetic fields, where the rate of fusion is controlled by adjusting the inputs of the reaction.

There are several active experimental campaigns to achieve fusion power. The National Ignition Facility (NIF) at Lawrence Livermore National Lab (LLNL) is the largest facility for ICF, with 192 laser beams producing a total of 1.8 MJ to drive fusion implosions. NIF has been in operation since 2009 (with all 192 beams) and continues to conduct experiments in an attempt to reach ignition. ITER, the International Thermonuclear Experimental Reactor, is the largest MCF facility and is currently under construction. Although ITER does not aim to be an operational power plant, the goal is to produce 500 MW of power for hundreds of seconds while only needing 50 MW to heat the plasma. At the time of this writing, the first plasma at ITER is scheduled for December 2025 [13].

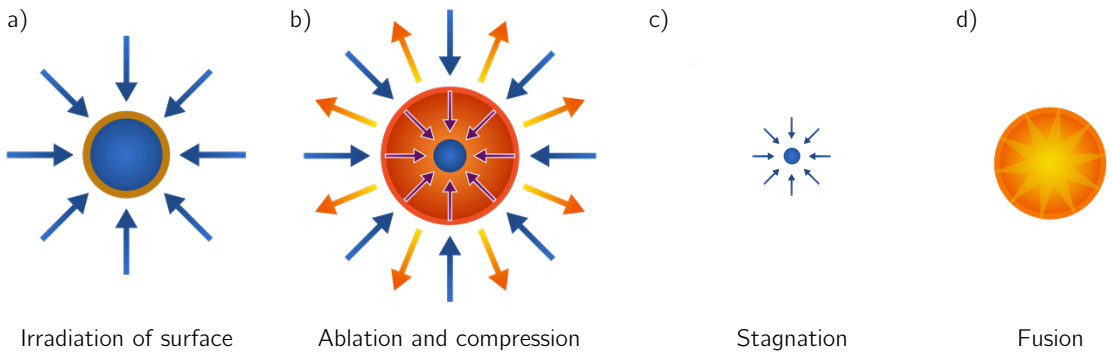

Figure 1.1: Schematic showing the basic principle of ICF. A spherical shell of fuel is a) heated by external radiation b) causing the outer material to rapidly expand, launching the remaining material inwards, resulting in c) stagnation at the center of the sphere and d) thermonuclear fusion of the remaining fuel. Adapted from wikipedia.org

1.2.1 Inertial confinement fusion

The aim of ICF is to produce the conditions required for thermonuclear fusion by compressing the fuel using converging shockwaves. Figure 1.1 shows the basic principle of ICF, where a) the outer layer of a spherical shell of fuel is heated by an intense external radiation source and b) material near the outer surface rapidly expands, acting as a rocket to force the remaining material inwards. Next, the converging material c) stagnates near the center, producing a dense core which d) ignites the fusion reaction, releasing a vast quantity of energy. The external radiation source can be in the form of direct laser irradiation (direct drive) or from thermal x-rays from a surrounding surface (indirect drive). The current design at NIF uses an indirect drive geometry, with a spherical fuel capsule placed inside a small gold cylinder, known as a hohlraum.

Early predictions for the requirements suggested that as little as 1 kJ of laser energy may be sufficient to achieve breakeven, defined by when the input energy and fusion energy output are equal, and > 100 kJ for electrical gain in a functioning power plant [14]. Following these predictions, several large laser facilities were

built to explore the physics of ICF and attempt to achieve ignition. LLNL, in particular, has built several Nd:glass laser systems since the early 70s, starting with the Long path laser, followed by the Argus, Shiva, Novette, and Nova lasers. The lessons learned from these systems ultimately led to the development of NIF.

ICF experiments at NIF have encountered several difficulties preventing ignition. Four primary areas of concerns include implosion symmetry, implosion velocity, the implosion adiabat, and fuel and hotspot mix. Achieving sufficient implosion symmetry requires careful control of the drive beam temporal and spatial profiles, both of which are complicated by the indirect drive geometry. Drive asymmetries created by the tent holding the spherical capsule in place have been especially difficult to overcome. Implosion velocity and adiabat are closely related, as operating at a higher adiabat generates higher implosion velocities at the expense of creating more entropy in the compressed fuel. The high foot campaign at NIF [15] used this approach, reaching higher compressions and neutron yields, but the additional entropy created by the higher adiabat ultimately prevents ignition. Nevertheless, probing the conditions created using this technique may prove to be useful in understanding fusion-relevant WDM physics. Finally, hydrodynamic instabilities result mixing of the layers of the target in the fuel and hotspot. This deviation from the ideal case of spherical symmetry reduces compression of the fuel and prevents ignition.

A report published in May 2016 on the status of the ignition campaign at NIF has questioned whether ignition is possible with the current configuration [16]. The report emphasizes the need to improve our understanding of the fundamental physics at play in WDM. Specifically, improved diagnostics to measure the conditions at stagnation and cross-platform data to validate theoretical models and simulation codes will be critical for the future success of ICF. The goal of the work presented in this thesis is to contribute to these areas of research.

1.3 X-ray sources

Since their discovery in 1985 by German physicist Wilhelm Röntgen, x-rays have been used to study the properties of matter. Within months of their discovery, x-rays were used to image a broken wrist [17]. Medical and dental x-ray devices use x-ray tubes to produce x-rays with energies of 30 keV or higher. X-ray tubes accelerate electrons through a vacuum tube towards an anode using a strong electric field. The accelerated electrons impact the anode, producing line emission and a broad spectrum of bremsstrahlung emission. Filters are added to attenuate low-energy x-rays to minimize the radiation dose the patient receives. X-ray tubes provide a reliable source of x-rays, but the intensity of x-rays emitted is far too low for measurements on the timescales of dynamic compression. Many x-ray diagnostics in HED physics experiments use a time-integrated detector, where the x-ray source duration determines the time resolution of the measurement. Time-resolved measurements of HED systems require high brightness x-ray sources with a sufficient flux of x-rays to probe the system in the timescale of interest.

1.3.1 He-α x-ray sources

Materials irradiated by intense laser light are common x-ray sources in HED experiments. Irradiation of materials by intense laser light on nanosecond timescales creates an ablation plasma that thermalizes on the timescale of 100s of picoseconds and the atoms become highly ionized. The laser can be tuned to create a plasma dominated by ions in the He-like state, where only two electrons are bound. Even in this highly charged state, inner-shell vacancies are quickly filled, resulting in characteristic line emission. The brightest emission line from these systems is He-α, corresponding to radiative decay with an electronic transition from the 2p to 1s orbital. He-α x-ray sources are most efficient below $\sim$10 keV, corresponding to

materials that can be efficiently ionized to the He-like state with laser irradiances on the order of 10^{15}–10^{16} W/cm^2 [18]. Because He-α x-ray energies correspond to the energies of specific electronic transitions, only specific energies are available.

1.3.2 K-α x-ray sources

For x-ray energies above $\sim$10 keV, He-α x-ray sources become inefficient due to the conditions required to ionize higher-Z atoms to the He-like state in a thermal plasma. In order to create significant K-shell emission from these higher-Z elements, higher laser intensities are needed. Ultra-high intensity pulses from short pulse lasers create a population of fast electrons, which stream through the material and create K-shell vacancies in the otherwise near-neutral atoms in the bulk material. Electrons from higher orbitals fill the K-shell vacancies, resulting in primarily K-α and K-β x-ray emission. K-α x-ray sources have better temporal resolution than He-α x-ray sources, as the duration of each is related to the duration of the laser. A primary drawback of K-α x-ray sources is that they produce fewer x-rays compared to He-α sources because short pulse lasers have lower energies than long pulse lasers. As with He-α sources, the x-ray energies from K-α sources are limited to the transition energies of available elements.

1.3.3 X-ray free electron lasers

X-ray free electron lasers (x-ray FELs) oscillate relativistic electron bunches to produce synchrotron radiation. By adjusting the parameters of the electron bunch and the alternating magnetic field structure, known as an undulator, the characteristics of the photon beam can be precisely tuned. X-ray FELs provide a bright, monochromatic, collimated source of x-rays with durations ranging from a few to 100s of fs at peak powers of 10 to 100 GW. A detailed review of the history and physics of x-ray FELs has recently been published by C. Pellegrini *et al.* [19].

1.4 Facilities

This dissertation reports on experiments conducted at two facilities: the Linac Coherent Light Source (LCLS) at SLAC National Accelerator Laboratory and the Trident laser facility at Los Alamos National Laboratory.

1.4.1 Linac Coherent Light Source

The Linac Coherent Light Source (LCLS) uses the accelerated electron beam from one-third of the linac at SLAC National Accelerator Laboratory to produce a bright, monochromic x-ray beam with photon energies ranging from 270 eV to 11.2 keV. Figure 1.2 shows a top view of LCLS. Electrons are injected at sector 20 (where Sector 0 is at the far end of the linac and each sector is 100 m in length) and accelerated by the linac in sectors 21–30. The electron beam enters the undulator hall where powerful magnetics oscillate the relativistic electron bunch to produce a coherent pulse of x-rays.

Two modes of operation are available for the x-ray beam at LCLS: self-amplified spontaneous emission (SASE) and self-seeded mode. SASE mode provides the highest total pulse energy with a few mJ per pulse for photon energies of 1.5–10 keV, where the x-ray pulse energy drops for photon energies outside this range. The bandwidth of the SASE beam is typically 0.2–0.5% for hard x-rays and 0.2–2.0% for soft x-rays [20]. The self-seeded beam has much higher peak brightness, reducing the spectral bandwidth in the hard x-ray regime by a factor of 40–50 [21]. This increase in peak brightness comes at the cost of total pulse energy, averaging 0.3 mJ per pulses, and much higher intensity fluctuations compared to SASE mode. For additional details about LCLS the reader is referred to an in-depth review of the facility published by C. Bostedt *et al.* [20].

There are currently seven hutches in operation at LCLS, three in the near exper-

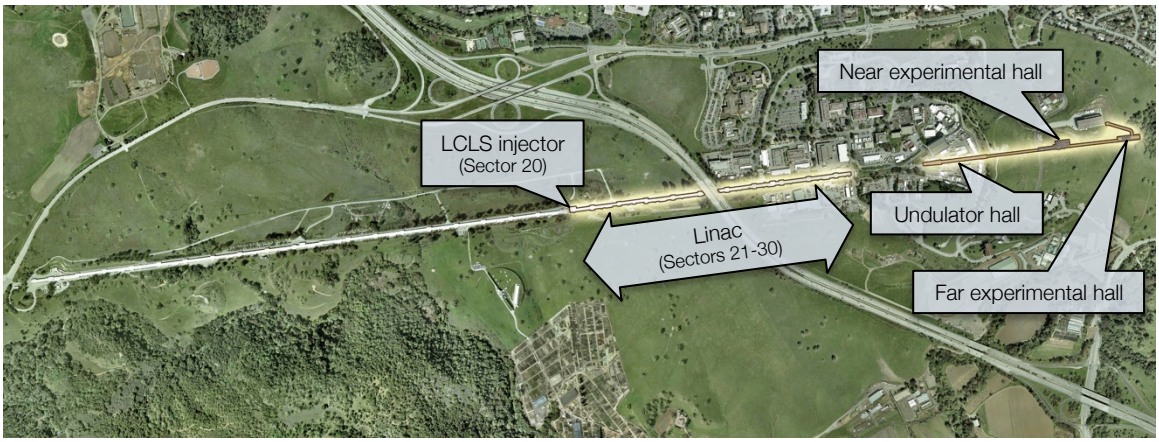

Figure 1.2: Top view of LCLS. The electrons are injected into the accelerating structure at sector 20 and accelerated by the linac in sectors 21-30. The relativistic electron bunch enters the undulator hall, where an alternating magnetic field oscillates the electron bunch to produce a coherent x-ray beam, which is then sent to the near or far experimental hall. Adapted from lcls.slac.stanford.edu

imental hall (NEH) and four in the far experimental hall (FEH). The Materials in Extreme Conditions (MEC) instrument [22, 23], located in the FEH, was designed to study HED physics and the properties of WDM. The FEL can be operated at 2.5–11.2 keV (in the first harmonic) at MEC and is focused with compound refractive beryllium lenses. MEC has an Nd:glass laser system, providing two beams (referred to as AB and EF) with approximately 1 J/ns with a maximum pulse energy of 25 J per beam. The cooling rate of the final amplifiers limits the repetition rate of these beams, requiring 7–10 minutes between shots (depending on the stability requirements of the experiment). The amplified beam is 40 mm in diameter and hybrid phase plates with focal spot sizes of 100, 150, 250, and 500 μm are available, or the system can be operated without phase plates or with phase plates provided by users. MEC also has a Ti:sapphire laser system with an output of 1 J in 50 fs at a repetition rate of 5 Hz. The Ti:sapphire system can also be fed into the final amplifier of the glass laser system to increase the energy to 7 J, although this reduces the repetition rate to the 7–10 minutes of the glass laser system.

1.4.2 Trident laser facility

The Trident laser facility at LANL is a kJ class laser with two long pulse beams and one short pulse beam. Each long pulse beam can deliver up to 200 J in a 1 ns pulse and can be frequency doubled to a wavelength of 527 nm. The experiment described in Chapter VI used the two long pulse beams and was conducted in the south target chamber.

1.5 Chapter summary

This chapter introduced WDM, a unique state of matter not accurately described by classical models. Thermonuclear fusion and the current technological challenges at NIF were discussed, motivating experiments to study the properties of WDM to directly benefit ICF research and the quest for a viable controlled thermonuclear fusion reactor. Chapter II discusses absorption of intense laser radiation by matter to model laser-driven compression and the interactions of x-rays with matter. Chapter III gives an introduction to shock physics and includes a discussion of equation of state models and material properties relevant to dynamic compression. The chapter concludes with an overview of diagnostic techniques used to study dynamically compressed matter. Chapter IV presents a method to predict and analyze x-ray diffraction patterns from highly stressed polycrystalline materials to measure dynamic material strength. Chapter V describes an experimental platform used to measure the dynamic strength of shock-compressed diamond at MEC. Chapter VI presents experimental measurements of x-ray fluorescence from shock-compressed foams at the Trident Laser Facility. Chapter VII concludes with a summary and a discussion of future work.

1.6 Role of the author

The work presented in this thesis would not have been possible without the contributions from collaborators at the University of Michigan, SLAC National Accelerator Laboratory, Los Alamos National Laboratory, Livermore National Laboratory, and others. This section has been included to clarify the author's role in each chapter. Specific contributions from others are clearly referenced when presented.

- Chapters II and III: These chapters are summaries of the background physics needed for the following chapters and have been taken from a variety of references as cited throughout the text.

- Chapter IV: The author developed the method presented in this chapter under the guidance of Luke Fletcher and Siegfried Glenzer. Density functional theory calculations used in this chapter were provided by Jan Vorberger.

- Chapter V: The experiment was designed and planned by the author and Luke Fletcher and conducted with assistance from the High Energy Density Science group and the instrument scientists at the MEC instrument at SLAC National Accelerator Laboratory.

- Chapter VI: The experimental effort was led by the author under the supervision of Paul Keiter and David Montgomery with assistance from members of the Center for Laser Experimental Astrophysics group at the University of Michigan and the laser operations staff at the Trident Laser Facility. The author performed the analysis presented in this chapter with input from the experimental team.

CHAPTER II

Direct laser irradiation of materials and x-ray physics

2.1 Introduction

This thesis describes shock compression experiments carried out at high power laser facilities using direct laser irradiation to drive shock waves in materials. The compressed states of matter are probed with a variety of time-resolved x-ray diagnostics. It is therefore worthwhile to discuss the absorption of the intense laser light by matter and provide an overview of x-ray physics relevant to the diagnostic techniques used in these experiments.

2.2 Direct laser irradiation of materials

Direct irradiation of a material by a laser creates a layer of hot plasma on the surface, known as an ablation plasma. Here we consider irradiances of 10^{12}–10^{16} W/cm^2, which are high enough to readily create a thermal ablation plasma, but low enough that multi-photon absorption leading to direct ionization is not a significant mechanism of ionization. As the laser ionizes the material, the free electron density of the plasma rises, increasing the electron plasma frequency, ω_{pe}, given by

$$\omega_{pe} = \sqrt{\frac{4\pi n_e e^2}{m_e}} \text{ (cgs)} = \sqrt{\frac{n_e e^2}{m_e \epsilon_0}} \text{ (SI)}, \tag{2.1}$$

where n_e is the free electron density and c is the speed of light.

Light can propagate in a plasma when the laser frequency is less than the electron plasma frequency. When the electron plasma frequency is greater than or equal the laser frequency the free electrons can oscillate at the laser frequency, forming a reflecting surface. The depth at which the plasma frequency is equal to the frequency of the laser is known as the critical surface. The critical electron density, n_c, is the electron density of the critical surface, given by

$$n_c = \frac{\pi m_e c^2}{e^2}\frac{1}{\lambda^2}\ \text{(cgs)} = \frac{4\pi^2 \epsilon_0 m_e c^2}{e^2}\frac{1}{\lambda^2}\ \text{(SI)} \tag{2.2}$$

where λ is the wavelength of the laser, or in typical units

$$n_c = 1.1 \times 10^{21} \lambda_{\mu m}^{-2}\ \text{cm}^{-3}, \tag{2.3}$$

where $\lambda_{\mu m}$ is the wavelength of the laser in microns. Eq. (2.3) shows that reducing the wavelength of the drive laser increases the critical electron density. This effect allows lasers with shorter wavelengths to penetrate deeper into a plasma with a density gradient, such as an ablation plasma, resulting in increased coupling efficiency and higher ablation pressures.

Dynamic compression experiments using lasers to drive the pressure wave typically involve irradiating a flat surface to produce a planar disturbance in the material. When irradiating a flat surface, the critical surface defines the maximum depth the laser energy can penetrate into the plasma. Beyond this depth, electron heat transport carries a fraction of the energy to the shock front.

2.2.1 Ablation pressure and electron heat transport

The rapid expansion of an ablation plasma exerts pressure on the remaining material. This pressure created by the rapidly expanding plasma is known as the

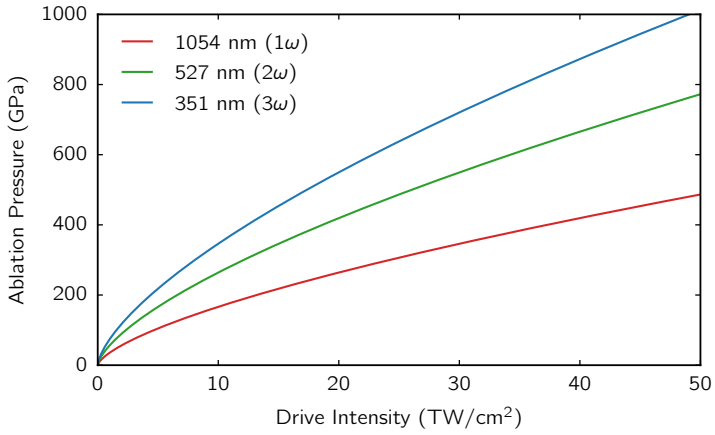

Figure 2.1: Ablation pressure for 1st, 2nd, and 3rd harmonic of Nd:glass laser systems with a fundamental wavelength of 1054 nm. Doubling or tripling the laser frequency (2ω and 3ω) can significantly increase the ablation pressure for a given driving intensity.

ablation pressure. Using a flux-limited transport model with reasonable assumptions for laboratory systems, the ablation pressure can be estimated by [24]

$$P_{abl} = 2 n_c k_B T_e \frac{Z+1}{Z} \tag{2.4}$$

For the case of $Z = 3$ and $T_e/T_i = 3$, which one might expect for an ablation plasma from a plastic surface, we can estimate the ablation pressure using the empirical formula

$$P_{abl} = 8.0\ I_{14}^{2/3} \lambda_{\mu m}^{-2/3}\ \text{MBar}, \tag{2.5}$$

where I_{14} is the laser irradiance in units of 10^{14} W/cm^2. Figure 2.1 shows ablation pressures calculated using Eq. (2.5) for a range of irradiances for the 1st, 2nd, and 3rd harmonic of Nd:glass laser systems.

Laser energy can only directly penetrate to the critical surface of the ablation plasma, after which the delivery of energy to the shock front occurs primarily by electron heat transport. Consequently, electron heat transport in a material plays a

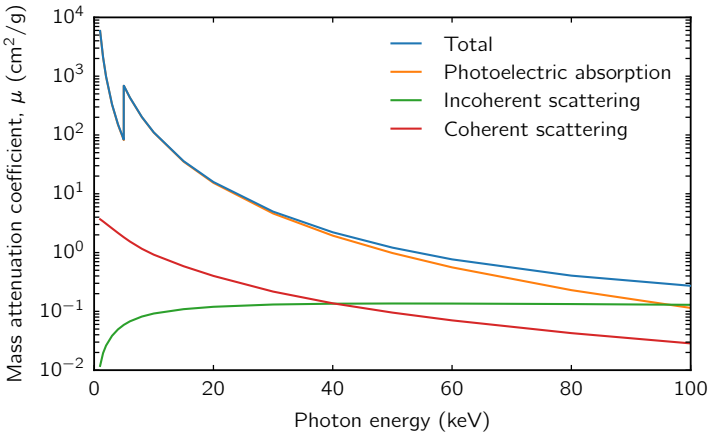

Figure 2.2: X-ray cross sections for unionized Ti. Photoelectric absorption is the dominant interaction for photon energies below ∼80 keV.

vital role in the ability to drive steady shocks using laser systems. The interaction of the laser and the material can be divided into the absorption region and the electron transport region. The absorption region has the lowest electron density, with the boundary defined by the depth with the critical electron density. This zone is where the laser heats the material, directly depositing energy into the system. Electron thermal transport dominates the dynamics in the electron transport region, where the electron density too high for the laser light to propagate.

2.3 X-ray physics

For x-ray energies below ∼100 keV the three primary mechanisms of interaction with matter are photoelectric absorption, coherent scattering, and incoherent scattering. Figure 2.2 shows the energy-dependent cross sections of these mechanisms for unionized titanium. At low photon energies, photoelectric absorption is the dominant interaction mechanism. At energies far above the highest electron binding energies incoherent and coherent scattering become significant.

2.3.1 Photoelectric absorption

Photoelectric absorption describes the absorption of an x-ray by an electron, destroying the x-ray and transferring its energy to the electron. Photoelectric absorption has the highest cross section at x-ray energies below $\sim$50 keV for mid-Z elements. The photoelectric absorption characteristics depend on the electronic structure of the elements in the material. This makes the cross section highly sensitive to bonding in cold matter and ionization state in plasma conditions.

2.3.1.1 Shells and edges

Photoelectric absorption cross sections have characteristic edges (abrupt changes in the cross section) corresponding to binding energies of electrons in atomic orbitals. The most prominent edge is the K-edge, corresponding to the energy required to remove a K-shell electron from an atom. The K-edge can be seen in the cross section of unionized Ti at 4.97 keV in Figure 2.2. For higher ionization states, the screening of the nuclear charge is reduced and the inner-shell electrons are bound more tightly. The change in K-shell binding energy shifts the K-edge, as shown for the case of Ti in Figure 2.3. X-rays just below the energy of an absorption edge do not have enough energy to remove an electron from the atomic shell and are unable to interact with those electrons. X-rays just above an absorption edge couple strongly to the electrons in the corresponding shell and are readily absorbed, resulting in the removal of an electron and the creation of the vacancy in that shell.

2.3.1.2 Radiative decay of excited states

A number of decay mechanisms can fill inner-shell electron vacancies. Radiative decay and Auger decay compete to fill vacancies in the K shell and L_3 subshell. Radiative decay occurs when an electron from a higher orbital fills the vacancy, resulting in the emission of an x-ray with energy equal to the difference in binding

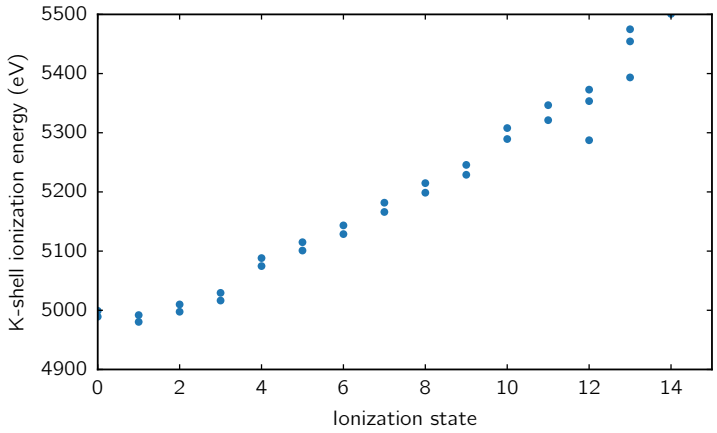

Figure 2.3: Ti K-edge energies as a function of ionization state calculated using CRETIN. Credit: Howard Scott.

energies of the two states. In the case of Auger decay, the transition energy is transferred to an electron in a higher orbital, ejecting it from the atom. The Coster-Kronig nonradiative process [25] further complicates the filling of vacancies in the L_1 and L_2 subshells, where the vacancy can move within the same subshell (e.g. $L_1 \rightarrow L_2$, $L_1 \rightarrow L_3$, or $L_2 \rightarrow L_3$) before radiative or Auger decay occur. The work presented here is only concerned with K-shell vacancies, where only radiative and Auger decay need to be considered.

Lower-Z elements with a K-shell vacancy have higher probabilities of decaying via Auger decay, while higher Z elements tend to decay via radiative decay. The fluorescence and Auger yields define the probabilities of each decay mode and have been calculated using a number of methods [26, 27]. Figure 2.4 shows tabulated fluorescence and Auger yields [1] for atoms with a single K-shell vacancy.

2.3.1.3 Effects of screening and bonding

The presence of bound electrons reduces the binding energy of other bound electrons. This phenomenon, known as the screening or shielding effect, alters the electronic structure of the atom and affects K-shell emission energies. Ionization

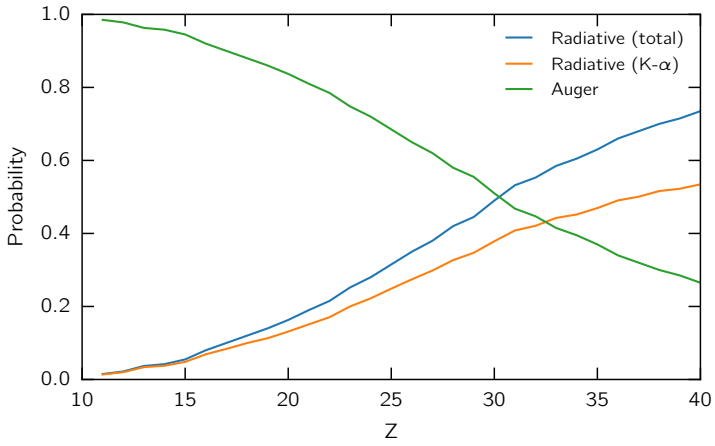

Figure 2.4: Probabilities of decay for elements with a K-shell vacancy [1]. For low-Z elements Auger decay is the dominant mechanism of decay, while for higher-Z elements radiative decay becomes significant.

reduces the screening of the nuclear charge and the K-shell electrons are bound more tightly, as shown for Ti in Figure 2.3. X-ray fluorescence energies are related to binding energies and therefore also affected by reduced screening. For example, He-α emission is simply K-α emission from an ion in the He-like state. In cold material, bonding and chemical properties such as oxidation state can affect x-ray fluorescence energies [28].

2.3.2 Coherent scattering and x-ray diffraction

Coherent scattering is defined as a scattering event that preserves the phase relationship of the incident wave. X-ray diffraction is an example of coherent elastic scattering of x-rays, where the periodic nature of crystal lattices can give rise to constructive interference of scattered radiation. The spacing between atoms in solids is on the order of Angstroms, corresponding to the wavelength of x-rays. The condition for constructive interference is satisfied when an incident beam reflecting off two crystal planes have a path length difference equal to an integer multiple of the wavelength of the radiation. The path length difference for reflections from two

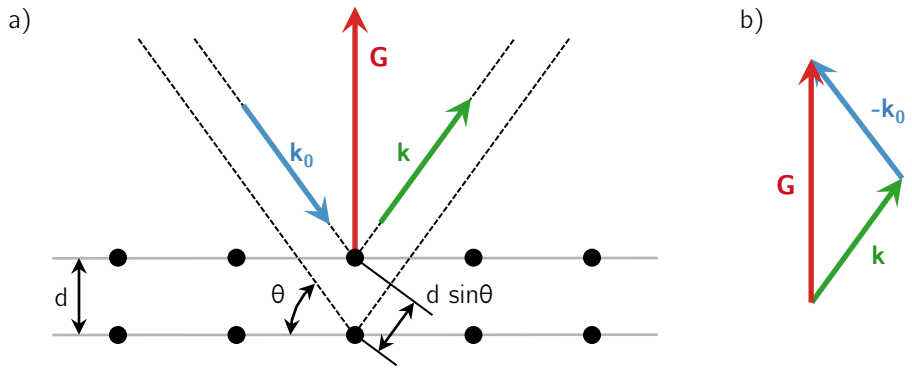

Figure 2.5: Two incident beams with equal wavelength and phase reflect off two atomic planes in a crystal. a) The beam reflecting off the lower surface travels an additional distance equal to $2d\sin\theta$. When this length is equal to an integer multiple of the x-ray wavelength the beams constructively interfere. b) In the Laue formulation, the condition for constructive interference is satisfied when $\mathbf{k} - \mathbf{k}_0 = \mathbf{G}$.

planes with separation d is given by $d\sin\theta$, where θ is the angle between the beam and the plane normal as shown in Figure 2.5a. This leads to the Bragg condition for x-ray diffraction, given by

$$n\lambda = 2d\sin\theta, \tag{2.6}$$

where n is an integer and λ is the wavelength of the incident radiation. Diffraction can also be considered in reciprocal space using the Laue diffraction condition,

$$\mathbf{k} - \mathbf{k}_0 = \mathbf{G}, \tag{2.7}$$

where $\mathbf{k}_0$ and $\mathbf{k}$ are the probe and scattered x-ray wave vectors, respectively, and $\mathbf{G}$ is the reciprocal lattice vector, as shown in Figure 2.5b. The magnitude of the probe wave vector is given by $k_0 = 2\pi/\lambda$ and x-ray diffraction is an elastic scattering process, requiring $|\mathbf{k_0}| = |\mathbf{k}|$. The reciprocal lattice vector is normal to the diffracting plane (in real space) with a magnitude of

$$\mathbf{G} = \frac{2\pi}{d}. \tag{2.8}$$

The Bragg condition is often more intuitive because it is formulated in real space, but the Laue condition is often more powerful in the analysis of diffraction patterns. Although these two formulations are equivalent, it is common to refer to diffraction in the reflecting geometry as Bragg diffraction and diffraction in the transmission geometry as Laue diffraction, for historical reasons.

There are two common diffraction configurations used in dynamic compression experiments for crystalline materials, which probe either single crystals or polycrystalline materials. Experiments on single crystals use a broadband x-ray source, such as a capsule implosion. The wide bandwidth of the x-ray source meets the diffraction condition for several planes in the sample and diffraction spots are recorded. This measurement is typically referred to as a Laue diffraction pattern. The orientation and compression of each plane in the compressed state are calculated from the locations of the diffraction spots. Monochromatic x-ray sources, such as an x-ray FEL, require polycrystalline samples. A polycrystalline material contains crystallites at a wide range of orientations, some fraction of which can meet the diffraction condition for a given state. In this case, diffraction rings, known as Debye-Scherrer diffraction rings, are produced by the polycrystalline sample.

2.3.2.1 Miller indices

Three primitive lattice vectors define the unit cell for a crystal lattice in real space, denoted $\mathbf{a}$, $\mathbf{b}$, and $\mathbf{c}$. For the simplest case of a cubic unit cell, the primitive lattice vectors are mutually orthogonal and their magnitudes are equal $(a = b = c)$.

Miller indices are the standard form of notation for planes and directions within a crystal system. Specific planes are denoted (hkl), while families of equivalent planes (by symmetry) are denoted $\{hkl\}$. Similarly, specific crystallographic direc-

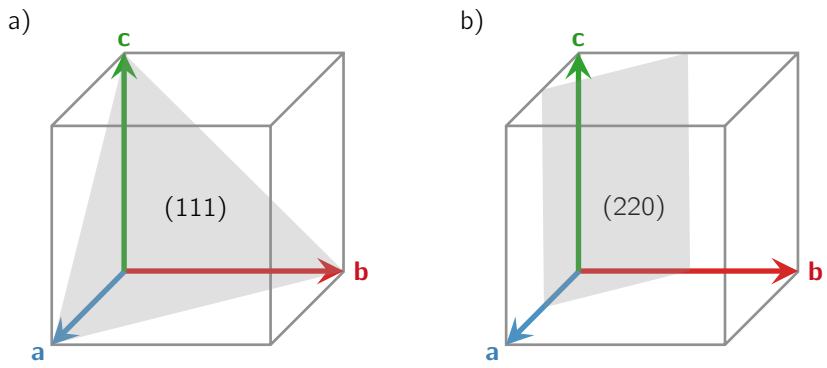

Figure 2.6: Examples of crystal planes defined using Miller indices, showing the a) (111) and b) (220) planes in a cubic crystal system.

tions are written $[hkl]$ and sets of equivalent directions are written $\langle hkl \rangle$. The plane (hkl) intersects the three primitive lattice vectors at points $\mathbf{a}/h$, $\mathbf{b}/k$, and $\mathbf{c}/l$, as shown for the (111) and (220) planes in a cubic system in Figure 2.6. An overbar denotes negative Miller (e.g. $1\bar{1}1$) and if any of the Miller indices are 0 for a given plane, the corresponding primitive lattice vector is parallel to the plane. The vector $[hkl]$ is defined by

$$\mathbf{v} = h\mathbf{a} + k\mathbf{b} + l\mathbf{c}. \tag{2.9}$$

The d spacing in crystal planes can be defined in terms of Miller indices and lattice parameters. For the common cases of cubic and hexagonal crystals, the d spacings are given by

$$\frac{1}{d^2} = \frac{h^2 + k^2 + l^2}{a^2} \qquad \text{(cubic)} \tag{2.10}$$

$$\frac{1}{d^2} = \frac{4}{3}\left(\frac{h^2 + hk + k^2}{a^2}\right) + \frac{l^2}{c^2} \qquad \text{(hexagonal)} \tag{2.11}$$

where $a = b$ for the hexagonal lattice.

Calculating d spacings for other unit cells becomes increasingly complicated,

making it useful to work in reciprocal space where all unit cells can be treated in the same way. The primitive lattice vectors in reciprocal space are given by

$$\mathbf{a}^* = \frac{2\pi}{V}\mathbf{b}' \times \mathbf{c}' \tag{2.12}$$

$$\mathbf{b}^* = \frac{2\pi}{V}\mathbf{c}' \times \mathbf{a}' \tag{2.13}$$

$$\mathbf{c}^* = \frac{2\pi}{V}\mathbf{a}' \times \mathbf{b}', \tag{2.14}$$

where V is the volume of the unit cell. The reciprocal lattice vector for plane (hkl) is defined by

$$\mathbf{G} = h\mathbf{a}^* + k\mathbf{b}^* + l\mathbf{c}^*, \tag{2.15}$$

and the d spacing of any plane is calculated using $d = 2\pi/G$.

2.3.3 X-ray Thomson scattering

X-ray Thomson scattering (XRTS) can be used to infer electron temperature, free electron density, and ionization state in HED plasmas from spectral shifts in scattered x-rays [29]. To provide a brief overview of XRTS, we begin with the double-differential cross section for a locally isotropic plasma, given by

$$\frac{\partial^2\sigma}{\partial\omega\partial\Omega} = \sigma_T \frac{\omega_s}{\omega_0}\frac{1}{2}\left(1 + \cos^2\theta\right) S(k,\omega), \tag{2.16}$$

where σ_T is the Thomson scattering cross section, ω_i (ω_s) is the frequency of the incident (scattered) radiation, $\omega = \omega_0 - \omega_s$ is the frequency shift, and $k = |k_0 - k_s| = 2\omega_0 \sin(\theta/2)/c$ is the scattering wave number at angle θ, and $S(k,\omega)$ is the dynamic structure factor (DSF).

The DSF contains all information about the time-dependent electron-electron

correlations in the system. It can be decomposed into two terms, accounting for elastic and inelastic scattering

$$S(k,\omega) = S_{el}(k,\omega) + S_{in}(k,\omega), \tag{2.17}$$

where the elastic and inelastic DSFs are given by

$$S_{el}(k,\omega) = |f(k) + q(k)|^2 S_{ii}(k,\omega) \tag{2.18}$$

and

$$S_{in}(k,\omega) = Z_f S^0_{ee}(k,\omega) + Z_b \int d\omega' S_{ce}(k,\omega-\omega') S_s(k,\omega'), \tag{2.19}$$

where Z_f (Z_b) is the number of free (bound) electrons per atom. In the elastic term, $f(k)$ is the atomic form factor, $q(k)$ represents the weighting from the electron screening cloud, and $S_{ii}(k,\omega)$ is the ionic DSF. The first term in the inelastic DSF describes inelastic scattering from free electrons, where $S^0_{ee}(k,\omega)$ is the free electron DSF. The second term describes inelastic scattering from bound-free electronic transitions, S_{ce}, modulated by the motion of the ions, S_s. Plasma parameters such as the electron temperature, free electron density, and ionization state affect the DSF and can be inferred by fitting XRTS spectra.

2.4 Chapter summary

This chapter presented an overview of the interaction between photons (optical and x-rays) with matter needed for shock-compression experiments. The absorption of laser light drives compression waves in materials, producing states of high pressure, density, and temperature. Adjusting the parameters of the laser drive enable precise control of the conditions in the compressed state. X-rays provide an

excellent tool to probe the dense matter created in these experiments.

CHAPTER III

Shock physics and relevant material properties

3.1 Introduction

Shock waves are the result of a disturbance moving through a medium faster than the material can respond. Although shocks are usually associated with chaotic events, such as explosions or impacts, they are present in systems all around us. Shocks exist on a vast range of spatial scales, including light years in the case of collisionless shocks in the interstellar medium, more familiar scales in sonic booms created by fighter jets, and down to microscopic scales in shock waves created by cavitation of bubbles in a fluid. The behavior of materials under dynamic compression is of interest to several fields including the modeling of planetary interiors and meteor impact events [9], exploring high-pressure phase changes [30–32], and understanding the initial compression phase of inertial confinement fusion implosions [8]. By studying the response of materials to powerful shock waves in the laboratory we are able to better understand the physical processes in such events. Excellent texts exist on shock physics including Zel'dovich and Raizer [33], Asay and Shahinpoor [2], and Drake [24]. This chapter presents a brief summary of shock physics along with an overview of material properties relevant to compressed solids and diagnostics for dynamic compression experiments.

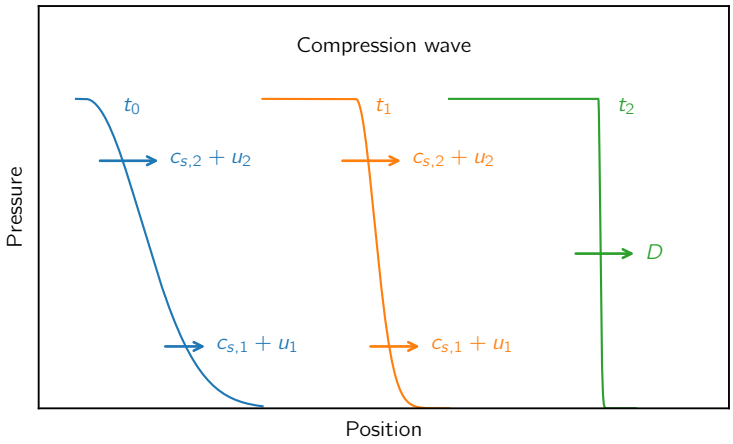

Figure 3.1: Diagram showing how a strong compression wave in a material steepens to form a shock by examining two points on the compression wave. The sound speed in most materials increases with pressure, so $c_{s,2} > c_{s,1}$ and the trailing point catches up to the leading edge creating a single, sharp interface moving at velocity D.

3.2 Fundamentals of shock physics

A shock is a disturbance in a material that moves faster than the sound speed (c_s) in the unperturbed material. This results in an abrupt change in the state of the medium, compressing and heating material as it propagates. The sound speed in the shocked material is higher due to the increased pressure, making the motion of the shocked material subsonic relative to the shock front. For most materials and pressure ranges, c_s increases with increasing pressure, causing an initial pressure gradient to steepen into a shock as shown in Figure 3.1. In this example, we consider two points on the initial pressure gradient, each with a local sound speed and particle velocity. Because c_s increases with pressure, $c_{s,2} > c_{s,1}$ and the trailing material at higher pressure moves faster than the leading edge of the disturbance. This results in the steepening of the shock and the creation of an abrupt interface traveling at a single shock velocity, D. In this thesis shock velocities are denoted by D and particle velocities by u to minimize confusion.

Although shocks are defined by an abrupt change in material conditions, the

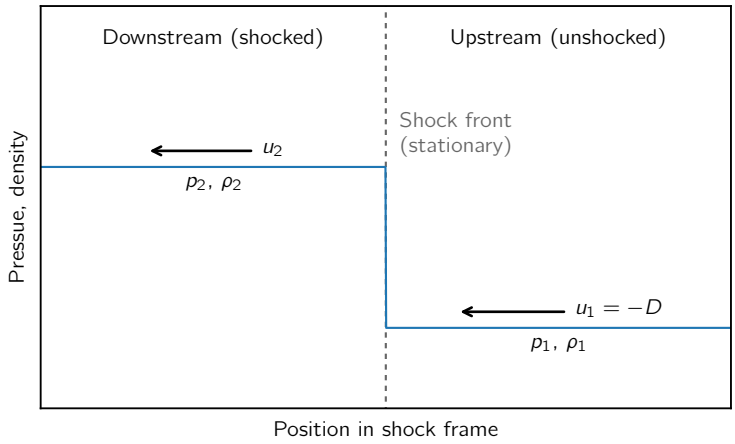

Figure 3.2: Diagram of a steady shock in the shock frame, where the shock front stationary. The material ahead of the shock is referred to the upstream material and the shocked region is downstream.

disturbance is still subject to the Euler equations, enforcing conservation of mass, momentum, and energy. The conservation equations are given in differential form by

$$\frac{\partial \rho}{\partial t} = -\nabla \cdot (\rho \mathbf{u}) \tag{3.1}$$

$$\frac{\partial}{\partial t}(\rho \mathbf{u}) = -\nabla \cdot (\rho \mathbf{u}\mathbf{u}) - \nabla p \tag{3.2}$$

$$\frac{\partial}{\partial t}\left(\frac{\rho u^2}{2} + \rho\epsilon\right) = -\nabla \left[\rho \mathbf{u}\left(\epsilon + \frac{u^2}{2}\right) + p\mathbf{u}\right] \tag{3.3}$$

where ρ is material density, $\mathbf{u}$ is the fluid velocity, p is the pressure of the fluid, and ϵ is specific internal energy. Here we have ignored radiation terms, which can be important in the case of strong shocks in low-density, high-Z materials.

The continuity equations given by Eqs. (3.1)–(3.3) can be written for a generalized conserved quantity, Q, as

$$\frac{\partial \rho_Q}{\partial t} = -\nabla \cdot \Gamma_Q. \tag{3.4}$$

If we consider a planar shock and move to the inertial frame where the shock front is stationary, as shown in Figure 3.2, we can define a Gaussian pillbox spanning the discontinuity. In this frame, known as the shock frame, the material ahead of the shock is referred to as the upstream material, and the post-shock material is downstream. Integrating over the pillbox yields

$$\int_{x1}^{x2} \frac{\partial}{\partial t}\rho_Q dx' = -\int_{x1}^{x2} \frac{\partial}{\partial x}\Gamma_Q(x')dx' = \Gamma_Q(x_2) - \Gamma_Q(x_1). \tag{3.5}$$

In the limit of a discontinuity, where $x_1 - x_2 \to 0$, the first term goes to 0 and the fluxes are equal: $\Gamma_Q(x_2) = \Gamma_Q(x_1)$. Applying this to the continuity equations, the jump conditions for a shock in one dimension are given by

$$\rho_1 u_1 = \rho_2 u_2 \tag{3.6}$$

$$\rho_1 u_1^2 + p_1 = \rho_2 u_2^2 + p_2 \tag{3.7}$$

$$\rho_1 u_1 \left(\epsilon_1 + \frac{u_1^2}{2}\right) p_1 u_1 = \rho_2 u_2 \left(\epsilon_2 + \frac{u_2^2}{2}\right) p_2 u_2 \tag{3.8}$$

An ideal material obeying the Euler equations would have an infinitely sharp discontinuity at the shock front. Real materials have a finite shock thickness, determined by viscosity and thermal conduction. The Swagle-Grady relationship [34] is an empirical fit to experimental data, showing that strain rate is proportional to the applied stress to the fourth power. For this reason, shocks in typical HED experiments have extremely high strain rates, forming a narrow shock front and can be considered to be a discontinuity.

3.2.1 Rankine-Hugoniot relation

Shock compression can reach a wide range of material states by varying the initial conditions and shock strength. The Rankine-Hugoniot relation defines the

set of states attainable from a given initial condition, commonly referred to as the shock Hugoniot, or simply the Hugoniot. This function depends on the initial state of the material, where the principal Hugoniot is the function with ambient initial conditions. Although the Hugoniot can be defined for a variety of state variables, here we consider the relationship between pressure and density, $p_2(p_1, 1/\rho_1, 1/\rho_2)$, or using the more common form with specific volume, $p_2(p_1, V_1, V_2)$, where $V = 1/\rho$.

The jump conditions given by Eqs. (3.6)–(3.8) are calculated in the shock frame, while measurements of shock velocity and postshock fluid velocity are made in the laboratory frame, where the upstream material is typically at rest. For the simple case of a shock moving through a medium initially at rest, the postshock fluid velocity is $u_p = u_1 - u_2$. The jump conditions (3.6)–(3.8) can be solved to calculate ρ_2, p_2, and ϵ_2 from measurements of D and u_p

$$\frac{\rho_2}{\rho_1} = \frac{D}{D - u_p} \tag{3.9}$$

$$p_2 - p_1 = \rho_1 D u_p \tag{3.10}$$

$$\epsilon_2 - \epsilon_1 = \frac{p_1 u_p}{\rho_1 D} + \frac{u_p^2}{2} \tag{3.11}$$

The change in pressure across the shock front is calculated by combining Eqs. (3.9) and (3.10) to eliminate the postshock particle velocity, giving

$$p_2 - p_1 = \rho_1 D^2 \left(1 - \frac{\rho_1}{\rho_2}\right) = \frac{D^2}{V_1}\left(1 - \frac{V_2}{V_1}\right). \tag{3.12}$$

If the shock Hugoniot for a material is known, the velocity of a shock can be calculated using Eq. (3.12)

$$D = \frac{1}{\rho_1}\sqrt{\frac{p_2 - p_1}{1/\rho_1 - 1/\rho_2}} = V_1\sqrt{\frac{p_2 - p_1}{V_1 - V_2}} \tag{3.13}$$

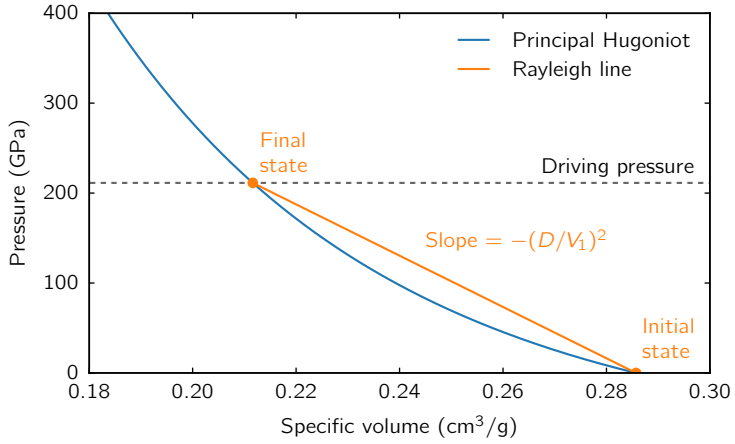

Figure 3.3: An example of a principle Hugoniot curve and Rayleigh line. The Rayleigh line connects the initial state to the final state at the driving pressure of the shock. The shock velocity for a single shock with a given driving pressure can be calculated from the slope of the Rayleigh line.

The line connecting the initial and final states in p-V space is known as the Rayleigh line, with a slope given by

$$\text{Slope} = -\left(\frac{D}{V_1}\right)^2 \tag{3.14}$$

as illustrated in Figure 3.3. This demonstrates the importance of knowing the shock Hugoniot to a high degree of accuracy for applications that require precise shock timing.

3.2.2 Shock stability

As shown in Figure 3.1, a shock is formed when the disturbance steepens and forms a discontinuity as a result of the sound speed increasing with pressure. In order for a sharp discontinuity to be maintained, disturbances behind the shock (traveling at $c_{s,2} + u_2$) must move at least as fast as the shock, otherwise they would lag behind and the discontinuity would dissipate. Similarly, small disturbances ahead of the shock must move slower than the shock or they would outrun the shock. These

conditions lead to three requirements for shock stability: the sound speed increases with increasing pressure, the disturbance is subsonic in the shocked material, and the shock is supersonic in the unshocked material

$$\frac{dc_s}{dp} > 0 \tag{3.15}$$

$$c_{s,2} + u_2 \geq D \tag{3.16}$$

$$D > c_{s,1} \tag{3.17}$$

where c_s is the adiabatic sound speed, given by

$$c_s = \sqrt{\left(\frac{\partial p}{\partial \rho}\right)_s} = V\sqrt{\left(-\frac{\partial p}{\partial V}\right)_s}. \tag{3.18}$$

Substituting Eq. (3.13) and (3.18) into Eq. (3.17) yields

$$\frac{p_2 - p_1}{V_1 - V_2} > -\left(\frac{\delta p}{\delta V}\right)_{s,1}. \tag{3.19}$$

The left side of the inequality is the (negative) slope of the Rayleigh line and the right side is the slope of the isentrope centered at the initial state, where the isentrope is the curve through phase space for a material under isentropic compression. Although the isentrope and Hugoniot are different curves in phase space, it can be shown that the isentrope and Hugoniot are tangent at the initial state [2]. Therefore, the slope of the Rayleigh line must be steeper than the Hugoniot at the initial state. Similarly, it can be shown that the slope of the Rayleigh line must be less than the slope of the Hugoniot at the final state

$$\frac{p_2 - p_1}{V_1 - V_2} \leq -\left(\frac{\delta p}{\delta V}\right)_{H,2}. \tag{3.20}$$

The conditions given by Eqs. (3.19) and (3.20) specify that the Hugoniot must

be concave up over the region spanned by the shock. This condition can also be shown by considering the requirement that the sound speed increases with pressure, and therefore with density as well. For simplicity, we work with c_s^2, which must follow the same trend.

$$\frac{\partial c_s^2}{\partial \rho} > 0 \tag{3.21}$$

Eq. (3.18) can be rewritten in the form

$$\frac{\partial c_s^2}{\partial \rho} = \frac{\partial^2 p}{\partial \rho^2} = 2V^3 \frac{\partial^2 p}{\partial V^2} \tag{3.22}$$

and inserted into Eq. (3.21), demonstrating that Eq. (3.21) is equivalent to

$$\frac{\partial^2 p}{\partial V^2} > 0. \tag{3.23}$$

This condition is a good rule of thumb, but not entirely general. In the cases of elastic-plastic failure (discussed in Section 3.6) or shock-induced phase transitions, the p-V curve may have additional features and the behavior in the intermediate region needs to be considered.

3.3 Equation of state

The equation of state (EOS) of a material specifies the relationship between two or more thermodynamic state variables, such as pressure, density, and temperature. Solving the jump conditions given by Eqs. (3.9)–(3.11) for a shocked system requires this additional constraint. It is often difficult to study the EOS at WDM conditions due to the small volumes of material created and short timescales the conditions exist in the laboratory. Additionally, EOS data is generally given for materials at thermodynamic equilibrium, while many WDM experiments create

conditions far from equilibrium.

3.3.1 Ideal gas EOS

The ideal gas EOS is often used for weakly coupled, non Fermi-degenerate systems, or as a first approximation due to its simplicity. In this model, the pressure of an ionized plasma is given by

$$p = Nk_BT = \frac{\rho(1 + \langle Z \rangle)k_BT}{Am_p}, \tag{3.24}$$

where $\langle Z \rangle$ is the mean ionization state in the plasma, A is the average atomic mass number of the ions in the plasma, m_p is the proton mass, and $N = 1 + \langle Z \rangle$ is the number of particles in the system.

The specific energy in an ideal gas is given by

$$\rho\epsilon = \frac{p}{\gamma - 1}, \tag{3.25}$$

where γ is the polytropic index of the material, defined by the ratio of specific heats at constant pressure and volume, $\gamma = C_p/C_V$. The number of degrees of freedom for each element in the system, ν, is related to the polytropic index by

$$\gamma = 1 + \frac{2}{\nu}. \tag{3.26}$$

For a monatomic gas with only three degrees of freedom $\gamma = 5/3$, which is a good approximation for highly ionized, weakly coupled plasmas. The sound speed in an ideal gas is given by

$$c_s = \sqrt{\frac{\gamma p}{\rho}}. \tag{3.27}$$

In the strong shock limit, it can be shown that the compression of an ideal gas

is given by [24]

$$\frac{\rho_2}{\rho_1} = \frac{\gamma + 1}{\gamma - 1}. \tag{3.28}$$

For $\gamma = 5/3$, this gives a maximum compression of 4. The fact that larger compressions are often created in HED experiments can be interpreted in two ways. First, most materials have more than three degrees of freedom (such as rotational or vibrational modes), which reduces γ and increases the maximum compression for a single shock. γ can then be fit to compression measurements and arguments can be made to justify the choice of γ. More likely, the ideal gas EOS is not an appropriate model for detailed analysis of many HED systems where the assumption of weakly coupled matter is not appropriate.

3.3.2 Tabular EOS

The wide range of conditions present in HED systems often makes them difficult to describe using a single EOS model. For example, in a typical laser-driven compression experiment, the laser heats an initially solid-density ablator material, creating a weakly coupled ablation plasma and compressed material that may be in the WDM regime. In the case of multi-shock systems, each shock encounters material at a different initial condition. While the first shock may encounter ambient material with a well-understood EOS, the shocked material upstream of the second shock may be in an entirely different regime. In particular, complex materials such as the low-density foams used in the x-ray fluorescence experiments described in a later chapter provide a unique challenge for EOS models. The porous nature of the foams creates complicated behavior, such as the collapse of the internal microstructure under strong compression, resulting in different compressions and temperatures than would be predicted by simple analytical models assuming a homogeneous material.

A common solution to this problem is to create a table of EOS data for a given

material, containing experimental and computational data for a variety of conditions. This method does not depend on a single model and can incorporate both experimental and theoretical data. Additionally, tabular data can be easily loaded into simulation packages, providing detailed EOS data without requiring additional computation.

The SESAME EOS library [35], maintained by Los Alamos National Laboratory, is widely used in the HED physics community, providing EOS data over a vast range of parameter space. The SESAME database currently contains data for around 150 materials, including elements, compounds, metals, polymers, and mixtures. Tables are populated with various theoretical models to fit experimental data with interpolation where necessary.

3.4 Blast waves

Blast waves are the inevitable result of a shock wave driven with a finite amount of initial energy. Blast waves are formed when a release wave, referred to as a rarefaction, from the driven surface overtakes the shock front. This occurs when the pressure source for the shock decays and can no longer maintain a steady shock. As material releases from the drive surface, the rarefaction approaches the shock front and eventually overtakes it, creating a sharp spike in pressure. Figure 3.4 shows the evolution from a strong shock to a blast wave.

3.4.1 Self-similar analysis of blast wave profiles

A self-similar model can greatly simplify the analysis of systems where the ρ_0 and R have the same functional form. The density, pressure, and fluid velocity profiles in blast waves can be calculated by assuming time-invariant profiles using similarity solutions. In this analysis, similarity variables are used to convert the partial dif-

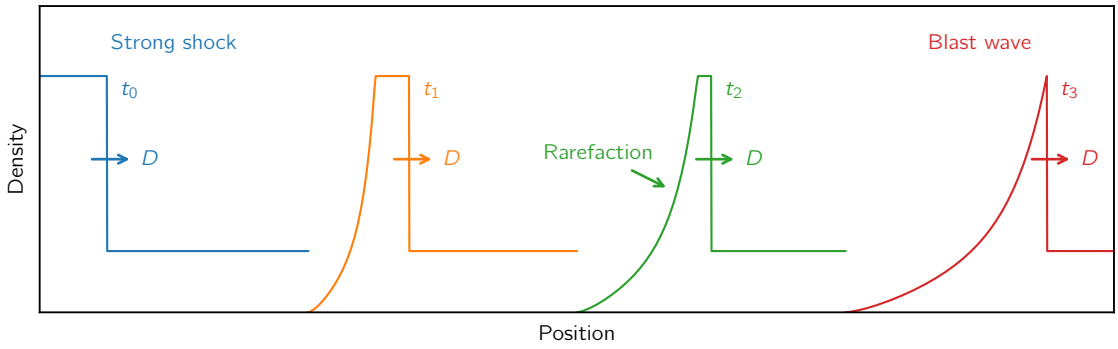

Figure 3.4: Diagram showing the transition from a strong shock to a blast wave. When the driving force maintaining the steady shock is removed material begins to release from the rear surface, creating a rarefaction. The rarefaction moves through the shocked material until it reaches the shock front and a sharp spike in pressure and density is created, known as a blast wave.

ferential equations of (3.1)–(3.3) into a set of ordinary differential equations. This derivation closely follows that from Drake [24], with a minor change in the final result to account for different symmetries. We begin by considering a blast wave traveling through an ideal gas and rewrite Eq. (3.3) in the form

$$\left(\frac{\partial}{\partial t} + \mathbf{u}\cdot\nabla\right) p - \frac{\gamma p}{\rho}\left(\frac{\partial}{\partial t} + \mathbf{u}\cdot\nabla\right)\rho = 0. \tag{3.29}$$

In order for the continuity equations to be converted to a self-similar form u, ρ, and p must be written as functions of a dimensionless similarity variable. Here, we use the similarity variable $\xi = r/R$, describing the spatial profile of the fluid parameters. The fluid velocity, density, and pressure are given by

$$u = \dot{R}U(\xi) \tag{3.30}$$

$$\rho = \rho_0(r,t)\Omega(\xi) \tag{3.31}$$

$$p = \rho_0(r,t)\dot{R}^2 P(\xi) \tag{3.32}$$

Eqs. (3.30)–(3.32) are then substituted into Eqs (3.1), (3.2), and (3.29) to give

$$\frac{\dot{\rho_0}}{\rho_0}\frac{R}{\dot{R}}\Omega(\xi) + \frac{\rho_0'}{\rho_0}U(\xi)\Omega(\xi) + [U(\xi)-\xi]\,\Omega'(\xi) + \Omega(\xi)U'(\xi) + \frac{s}{\xi}U(\xi)\Omega(\xi) = 0 \tag{3.33}$$

$$\frac{\rho_0' R}{\rho_0}P(\xi) + \frac{R\ddot{R}}{\dot{R}^2}U(\xi)\Omega(\xi) + [U(\xi)-\xi]\,U'(\xi)\Omega(\xi) + P'(\xi) = 0 \tag{3.34}$$

$$\begin{aligned}\frac{\dot{\rho_0}}{\rho_0}\frac{R}{\dot{R}}(1-\gamma)P(\xi) + \frac{\rho_0' R}{\rho_0}U(\xi)(1-\gamma)P(\xi) + 2\frac{R\ddot{R}}{\dot{R}^2}P(\xi) + \\ [U(\xi)-(\xi)]\left(P'(\xi) - \gamma P(\xi)\frac{\Omega'(\xi)}{\Omega(\xi)}\right) = 0\end{aligned} \tag{3.35}$$

where the primed state functions represent derivatives with respect to ξ, ρ_0' is the spatial derivative of ρ_0, and s = 0, 1, 2 for planar, cylindrical, and spherical symmetry, respectively. The case of a uniform initial density profile, where $\dot{\rho_0} = \rho_0' = 0$, simplifies these equations, yielding

$$[U(\xi)-\xi]\,\Omega'(\xi) + \Omega(\xi)U'(\xi) + \frac{s}{\xi}U(\xi)\Omega(\xi) = 0 \tag{3.36}$$

$$\frac{R\ddot{R}}{\dot{R}^2}U(\xi)\Omega(\xi) + [U(\xi)-\xi]\,U'(\xi)\Omega(\xi) + P'(\xi) = 0 \tag{3.37}$$

$$2\frac{R\ddot{R}}{\dot{R}^2}P(\xi) + [U(\xi)-(\xi)]\left(P'(\xi) - \gamma P(\xi)\frac{\Omega'(\xi)}{\Omega(\xi)}\right) = 0 \tag{3.38}$$

Next, we assume a power-law solution and write the spatial function

$$R = R_0 t^{\alpha}, \tag{3.39}$$

where the units involved in the system define the exponent α, determined by the form of the energy of the initial impulse. For a spherical blast wave, the energy is the total energy of the initial explosion, while in a planar blast wave the energy is given in units of energy per unit area. For planar and spherical symmetry one finds the following exponents for r and t to make the quantity dimensionless

$$\frac{E_{0,p}t^2}{\rho_0 r^3} = \text{constant (planar)} \qquad \text{and} \qquad \frac{E_{0,s}t^2}{\rho_0 r^5} = \text{constant (spherical)}, \tag{3.40}$$

where $E_{0,p}$ is the initial energy per unit area for the planar case and $E_{0,s}$ in the initial energy in the spherical case. α and s are thus related by

$$\alpha = \frac{2}{3+s}, \tag{3.41}$$

and the functional form for the spatial extent of the blast waves becomes

$$R = \frac{1}{Q}\left(\frac{E_0}{\rho_0}\right)^{\alpha/2} t^{\alpha}, \tag{3.42}$$

where Q is a constant that can be calculated by integrating over the blast wave profile and normalizing to the initial energy.

By taking time derivatives of Eq. (3.39), we find

$$\frac{R\ddot{R}}{\dot{R}^2} = 1 - \frac{1}{\alpha} = -\left(\frac{1+s}{2}\right), \tag{3.43}$$

which can be inserted into Eqs. (3.36)–(3.38) to obtain the equations for a blast wave propagating through a uniform medium assuming self-similar motion:

$$[U(\xi) - \xi]\,\xi\Omega'(\xi) + [\xi U'(\xi) + sU(\xi)]\,\Omega(\xi) = 0 \tag{3.44}$$

$$-\left(\frac{1+s}{2}\right)\Omega(\xi)U(\xi) + [U(\xi) - \xi]\,\Omega(\xi)U'(\xi) + P'(\xi) = 0 \tag{3.45}$$

$$-(1+s)\,\Omega(\xi)P(\xi) + [U(\xi) - \xi]\,[\Omega(\xi)P'(\xi) - \gamma P(\xi)\Omega'(\xi)] = 0 \tag{3.46}$$

Solving these equations requires three boundary conditions. We assume the case of a strong shock and set the boundary conditions at the shock front, given by

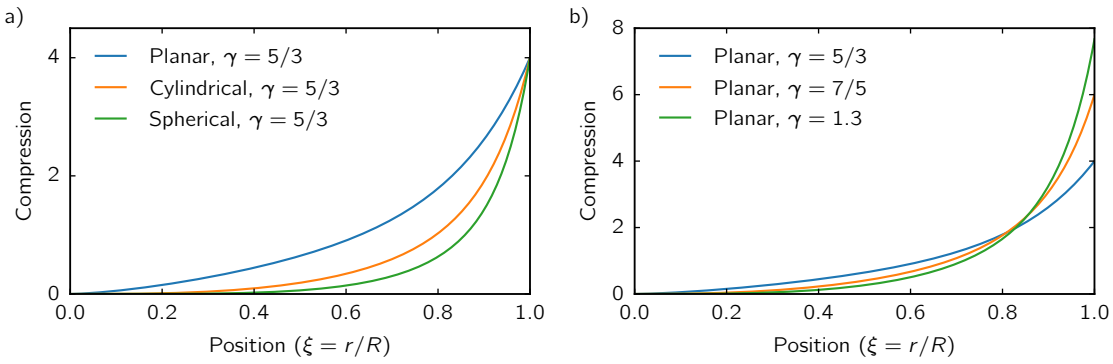

Figure 3.5: Calculated density profiles for self-similar blast waves showing the effect of a) symmetry and b) adiabatic index.

$$U(1) = P(1) = \frac{2}{\gamma + 1} \tag{3.47}$$

$$\Omega(1) = \frac{\gamma + 1}{\gamma - 1} \tag{3.48}$$

Figure 3.5a shows density profiles of blast waves for planar, cylindrical, and spherical symmetry calculated for $\gamma = 5/3$. Figure 3.5b shows the effect of changing γ for a planar blast wave, where reducing γ results in a larger compression at the shock front and a narrower density profile near the leading edge of the blast wave. The flexibility provided by adjusting γ enables a wider range of experimental data to be fit using this model, but as discussed in Section 3.3.1 it is important to keep in mind that this is a simple model and a good fit does not guarantee that the correct physics is being modeled.

3.5 Shocks in solids

3.5.1 Stress-strain relationship

Before investigating the response of materials to shocks, it is worthwhile to discuss how materials respond to forces in more general terms. A stress-strain relation-

ship characterizes the response of materials to an applied stress. Stress is a measure of the pressure on the system and strain is a dimensionless quantity defining the deformation of a sample.

Several definitions of strain exist for various applications. Perhaps the most ubiquitous definition is the engineering strain, which is valid in the limit of small strains, given by

$$\epsilon_e = \frac{l}{l_0} - 1, \tag{3.49}$$

where l_0 and l are the lengths of the sample before and after the deformation, respectively. True strain provides a more accurate measure of strain for large deformations, taking into account higher order strain terms, given by

$$\epsilon_t = \ln \frac{l}{l_0} \tag{3.50}$$

$$= \ln(1 + \epsilon_e) = \epsilon_e - \frac{\epsilon_e^2}{2} + \frac{\epsilon_e^3}{3} - ... \tag{3.51}$$

Eq. (3.51) shows that the engineering strain is a good approximation for small strains, where higher order terms can be neglected.

The stress-strain relationship of materials can be quantified by the bulk modulus, shear modulus, Young's modulus, and Poisson's ratio. The bulk modulus, K, is a measure of the ability of a material to resist hydrostatic compression and can be thought of as the stiffness of the material. It is defined by the change in pressure with respect to volume or density

$$K = -V\frac{dp}{dV} = \rho\frac{dp}{d\rho}. \tag{3.52}$$

Characterizing the stress-strain relationship for directional stresses requires two

moduli. Young's modulus, E, is a measure of the ability of a material to resist compressive or tensile stresses and the shear modulus, μ, for shear stresses, defined by

$$E = \frac{\partial \sigma}{\partial \epsilon} \qquad \text{and} \qquad \mu = \frac{\partial \tau}{\partial \gamma}, \tag{3.53}$$

where σ is a normal stress, ϵ is normal strain, τ is shear stress, and γ is shear strain.

Poisson's ratio quantifies the strain in the transverse directions when a material is strained in one direction

Poisson's ratio, ν, is another important material property, which describes the relationship between strains in the loading and transverse directions. Poisson's ratio quantifies the transverse expansion of a material under uniaxial compression. It is defined by the negative ratio of transverse to axial strain,

$$\nu = -\frac{d\epsilon_{tr}}{d\epsilon_{ax}}. \tag{3.54}$$

For a more rigorous understanding of stresses and strains, it is necessary to use their tensor forms. Working in the small strain limit, the components of the strain tensor are defined by

$$\epsilon_{ij} = \frac{1}{2}\left(\frac{\partial u_i}{\partial x_j} + \frac{\partial u_j}{\partial x_i}\right), \tag{3.55}$$

where $\mathbf{x}$ defines a Cartesian coordinate system and $\mathbf{u}$ is the displacement vector created by the strain. This definition makes it clear that the strain tensor must be symmetric and can, therefore, be written

$$\epsilon = \begin{pmatrix} \epsilon_x & \gamma_{xy} & \gamma_{xz} \\ \gamma_{xy} & \epsilon_y & \gamma_{yz} \\ \gamma_{zx} & \gamma_{yz} & \epsilon_z \end{pmatrix}. \tag{3.56}$$

The diagonal terms ($\epsilon_{ii} = \epsilon_i$) are normal strains and the off-diagonal terms are shear strains.

Similarly, the Cauchy stress tensor defines the applied stresses

$$\sigma = \begin{pmatrix} \sigma_x & \tau_{xy} & \tau_{xz} \\ \tau_{xy} & \sigma_y & \tau_{yz} \\ \tau_{xz} & \tau_{yz} & \sigma_z \end{pmatrix}, \tag{3.57}$$

where σ_i is a compressive stress in the i direction and τ_{ij} is a shear stress applied to the i face in the j direction. Here, we use the convention of using τ_{ij} to denote shear stresses to clearly differentiate between compressive and shear stresses, but σ_{ij} is also common in the literature.

3.5.2 Vinet EOS

The Vinet EOS is a commonly used model to predict the isothermal compression of various solids [36, 37]. The Vinet EOS model takes advantage of the fact that the compressibility of solids is generally dominated by the interaction of overlapping electron orbitals, allowing a single functional form to fit compressibility data for all classes of solids. The model only applies to materials under compression, as this assumption is not valid for materials in tension.

The pressure is given in as a function of strain, where $X = (V/V_0)^{1/3}$, and temperature, T, by

$$p(X, T) = 3K_0 \frac{1 - X}{X^2} \exp\left[\eta(1 - X)\right], \tag{3.58}$$

where K_0 is the bulk modulus in the uncompressed state and η is a function of the pressure derivative of the bulk modulus, given by

$$\eta = \frac{3K_0' - 1}{2}, \tag{3.59}$$

where $K_0' = (\partial K_0/\partial p)_{p=0}$. Eq. (3.58) can be used to plot $p(X,T)$ if K and K' are known. For example, the hydrostatic compression of diamond has been fit using $K_0 = 438$ GPa and $K_0' = 3.38$ [38].

3.5.3 Linear elastic theory

Linear elastic theory is valid in the small strain limit, where the stress-strain relationship obeys the generalized form of Hooke's law

$$\sigma = \mathbf{C}\epsilon, \tag{3.60}$$

where $\mathbf{C}$ is the elastic stiffness tensor. This equation can be rewritten using the elastic compliance tensor, $\mathbf{S}$, where $\mathbf{S} = \mathbf{C}^{-1}$, yielding

$$\epsilon = \mathbf{S}\sigma. \tag{3.61}$$

For the work presented here, elastic constants refer to elastic stiffness coefficients.

The general form of the elastic stiffness tensor is a 6×6 matrix with 36 terms. This tensor must be symmetric [39], reducing the maximum number of independent terms to 21:

$$\begin{pmatrix} C_{11} & C_{12} & C_{13} & C_{14} & C_{15} & C_{16} \\ C_{12} & C_{22} & C_{23} & C_{24} & C_{25} & C_{26} \\ C_{13} & C_{23} & C_{33} & C_{34} & C_{35} & C_{36} \\ C_{14} & C_{24} & C_{34} & C_{44} & C_{45} & C_{46} \\ C_{15} & C_{25} & C_{35} & C_{45} & C_{55} & C_{56} \\ C_{16} & C_{26} & C_{36} & C_{46} & C_{56} & C_{66} \end{pmatrix}. \tag{3.62}$$

Although linear elastic coefficients are only valid for small strains, if they are calculated for highly-stressed initial conditions, the pressure range of their validity

can be greatly increased. This is the method used in the diffraction analysis presented in Chapter IV, where density functional theory (DFT) calculations were used to calculate linear elastic coefficients for diamond at hydrostatic pressures up to 700 GPa.

3.5.3.1 Cubic crystal systems

For crystal systems, symmetries reduce the number of independent elastic coefficients. Cubic systems, for example, have independent elastic constants: C_{11}, C_{12}, and C_{44}. The stress-strain relationship for a cubic system is thus

$$\begin{pmatrix} \sigma_{xx} \\ \sigma_{yy} \\ \sigma_{zz} \\ \tau_{yz} \\ \tau_{zx} \\ \tau_{xy} \end{pmatrix} = \begin{pmatrix} C_{11} & C_{12} & C_{12} & 0 & 0 & 0 \\ C_{12} & C_{11} & C_{12} & 0 & 0 & 0 \\ C_{12} & C_{12} & C_{11} & 0 & 0 & 0 \\ 0 & 0 & 0 & C_{44} & 0 & 0 \\ 0 & 0 & 0 & 0 & C_{44} & 0 \\ 0 & 0 & 0 & 0 & 0 & C_{44} \end{pmatrix} \begin{pmatrix} \epsilon_{xx} \\ \epsilon_{yy} \\ \epsilon_{zz} \\ \gamma_{yz} \\ \gamma_{zx} \\ \gamma_{xy} \end{pmatrix}. \tag{3.63}$$

The bulk elastic parameters described in Section 3.5.1 can be written in terms of the elastic constants. For cubic crystal systems, they are given by

$$K = \frac{C_{11} + 2C_{12}}{3} \tag{3.64}$$

$$E = \frac{C_{11}^2 + C_{11}C_{12} - 2C_{12}^2}{C_{11} + C_{12}} \tag{3.65}$$

$$\mu = \frac{C_{11} - C_{12}}{2} \tag{3.66}$$

$$\nu = \frac{C_{12}}{C_{11} + C_{12}}. \tag{3.67}$$

3.5.4 Elastic anisotropy

Elastically isotropic materials have the same elastic properties regardless of orientation with respect to an applied stress. In the case of isotropic cubic crystals, two independent stiffness coefficients fully describe the material, C_{11} and C_{12}, where the third coefficient, C_{44}, is defined by $C_{44} = (C_{11} - C_{12})/2$. The Zener anisotropy ratio [39], A, quantifies the elastic anisotropy of a material, defined by the ratio

$$A = \frac{2C_{44}}{C_{11} - C_{12}}. \tag{3.68}$$

If $A = 1$ the material is isotropic and will have identical elastic properties in all directions. When A deviates from unity the stress-strain relationship of the material becomes directionally dependent. Table 3.1 gives the elastic constants for a variety of solids at ambient conditions along with the calculated anisotropy factor. Most cubic metals have $A > 1$, meaning they are softer when compressed along the $\langle 100 \rangle$ direction than along $\langle 111 \rangle$. Tungsten is an interesting case, where $A = 1.00$, and is therefore elastically isotropic at ambient conditions.

3.5.5 Reuss and Voigt limits

Modeling the stress-strain behavior of polycrystalline materials poses an interesting challenge due to interactions of crystal grains within the sample in addition to the interaction of atoms within each crystallite. Analytical models of the stress-strain relationship for polycrystalline materials require assumptions on the behavior at the grain boundaries. The Voigt limit [41] assumes continuous strain across grain boundaries while the Reuss limit [42] assumes continuous stress. This behavior is shown schematically for two crystallites with equal initial lengths but different Young's moduli in Fig 3.6, where in the a) Voigt limit both crystallites experience identical strain and in the b) Reuss limit each crystallite is exposed to the same

Class	Material	$\mathbf{C_{11}}$ ($\mathbf{10^{10}\ N/m^2}$)	$\mathbf{C_{12}}$ ($\mathbf{10^{10}\ N/m^2}$)	$\mathbf{C_{44}}$ ($\mathbf{10^{10}\ N/m^2}$)	$\mathbf{A}$ $\mathbf{2C_{44}/(C_{11}-C_{12})}$
Metals	Ag	12.4	9.3	4.6	2.94
	Al	10.8	6.1	2.9	1.23
	Au	18.6	15.7	4.2	2.86
	Cu	16.8	12.1	7.5	3.23
	α-Fe	23.7	14.1	11.6	2.44
	Mo	46.0	17.6	11.0	0.78
	Na	0.73	0.63	0.42	8.33
	Ni	24.7	14.7	12.5	2.50
	Pb	5.0	4.2	1.5	3.70
	W	50.1	19.8	15.1	1.00
Covalent solids	Si	16.6	6.4	8.0	1.56
	Diamond	107.6	12.5	57.6	1.20
	TiC	51.2	11.0	17.7	0.88
Ionic solids	LiF	11.2	4.6	6.3	1.92
	MgO	29.1	9.0	15.5	1.54
	NaCl	4.9	1.3	1.3	0.72

Table 3.1: Stiffness coefficients and Zener anisotropy ratios for selected cubic materials [40].

stress.

The Voigt limit simplifies modeling diffraction from polycrystalline materials due to the geometrical nature of the compression. All crystallites are assumed to compress the same, making it possible to construct analytical models the final positions of all initial crystallite planes. Applied stresses are calculated using the applied strains and the bulk elastic properties from Section 3.5.1. The Voigt limit is a reasonable model for polycrystalline materials consisting of a single, elastically isotropic material.

The Reuss limit requires an understanding of how crystals respond to forces in various directions, which can be calculated using the elastic stiffness tensor. This is important when materials have large elastic anisotropies, where strains depend on crystallite orientation, or in mixtures of materials with different elastic properties. In this limit, strains are calculated directly from an applied stress field, but a brute force method to apply the correct stress tensor to crystallites with each initial ori-

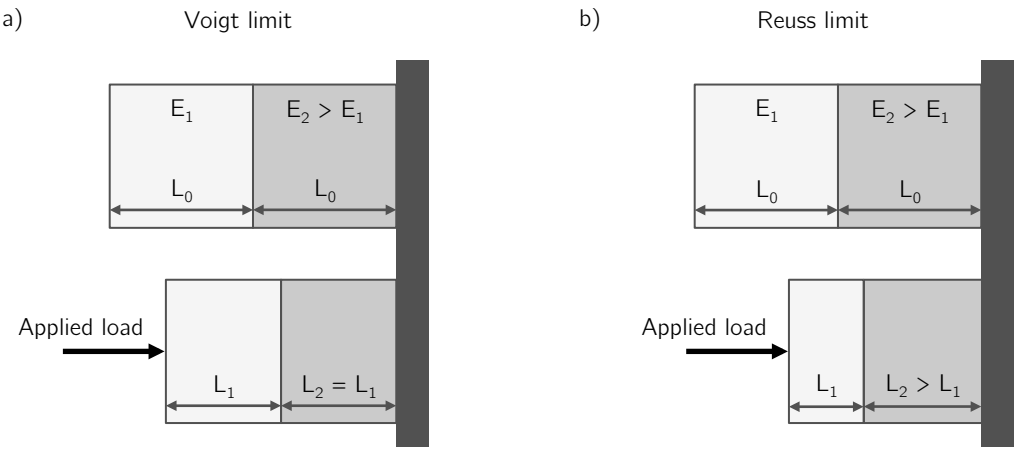

Figure 3.6: Comparison of the a) Voigt and b) Reuss limits used to model the behavior of compressed polycrystalline materials. Here we consider the simple case of two crystallites with the same initial length, L_0, but with different Young's moduli ($E_2 > E_1$). The Voigt limit assumes all crystallites experience identical strains and therefore the final lengths are equal ($L_1 = L_2$). The Ruess limit applies equal stresses to each crystallite, thus accounting for the Young's modulus of each crystallite, resulting in different final strain states ($L_1 < L_2$).

entation present in the sample is required. The distribution of strains created by a single stress field in the Reuss limit is not present in Voigt limit models.

3.6 Elastic-plastic response of solids

The ability of solids to support shear stresses has a profound impact on shock propagation. Shocks at low driving pressures create elastic waves that move through the material without rearrangement of the crystal structure. If the shock strength is above a threshold where the crystal structure begins to fail, known as the Hugoniot elastic limit (HEL), a plastic deformation wave is created. This two-wave structure can be understood by considering the Rayleigh lines for a material with an elastic compression region, as shown in Figure 3.7. The plastic deformation wave creates disorder in the crystal and relieves shear stresses in the lattice, reducing the difference in stresses between the shock and transverse directions. If the pressure is

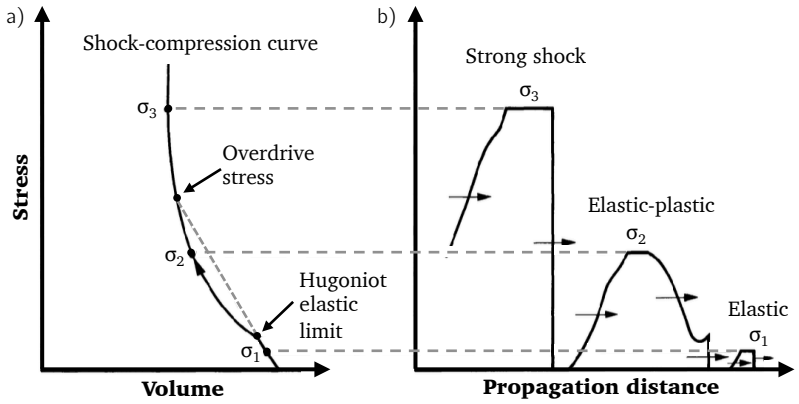

Figure 3.7: Example shock Hugoniot and pressure profiles. a) Example shock-compression curve for a solid with strength, with a linear elastic region below the HEL and the overdrive stress defined by the intersection of the elastic Rayleigh line with the shock-compression curve. b) Stress profiles for shocks with varying driving pressures. Pressures below the HEL or above the overdrive stress result in a single-wave structure, while intermediate driving pressures create a two-wave structure. Figure adapted from Asay and Shahinpoor [2].

above the overdrive stress threshold, defined by the point where the elastic Rayleigh line intercepts the Hugoniot, the plastic wave overtakes the elastic wave, forming a single-wave structure. If the driving pressure is between the HEL and the overdrive stress threshold, a two-wave structure will form with an elastic precursor followed by a plastic deformation wave.

3.6.1 Elastic waves

Elastic waves do not allow for stress relief within the crystal via dislocations or slip planes, resulting in a state of uniaxial strain, where all compression is in the direction of the shock. The elastic wave is a precursor in the system, encountering unperturbed material. Using Eq. 3.12 and using the specific volume of the compressed material, the pressure of the postshock material in the elastic wave is given by

$$P_{el} = \rho_0 D^2 \left(1 - \rho_0 V_{el}\right) = -\left(\rho_0 D\right)^2 V_{el} + \rho_0 D^2. \tag{3.69}$$

The shock velocity of the elastic wave is independent of pressure, making this a linear equation in V_{el} with the slope given by $-\left(\rho_0 D\right)^2$ and intercept of $\rho_0 D^2$.

3.6.2 Plastic waves

If the shock pressure is above the HEL and below the overdrive stress, the line connecting the initial and final states does not meet the stability conditions given by Eq. (3.19). This results in an elastic wave being launched at the HEL with a slower plastic wave trailing behind. The plastic wave creates disorder in the crystal structure and allows for stress relief within the lattice. The dislocation model of plasticity considers stress relief via movement of defects in the crystal, which have a lower threshold than the movement of entire crystal planes. The flow of dislocations is thought to be the primary method of stress relaxation in uniaxially compressed materials. Dislocations in the crystal can be preexisting within a material or created spontaneously in a process known as homogeneous nucleation.

The plastic deformation wave propagates through material perturbed by the elastic precursor. To calculate the pressure of this wave we consider a two-shock system where we assume the velocity of each shock is known. Solving for the particle velocities in each shock we find

$$u_1 = D_1 \left(1 - \frac{\rho_0}{\rho_1}\right) \tag{3.70}$$

$$u_2 = D_2 \left(1 - \frac{\rho_1}{\rho_2}\right) + D_1 \left(\frac{\rho_1 - \rho_0}{\rho_2}\right), \tag{3.71}$$

where the subscripts 0, 1, and 2 refer to the unshocked material, elastic precursor, and plastic regions, respectively. The stress in the shock (z) direction is given by

$$\sigma_{z2} = \rho_0 D_1 u_1 + \rho_1 \left(D_2 - u_1\right)\left(u_2 - u_1\right), \tag{3.72}$$

which is a function of D_1, D_2, and ρ_1. This gives a value for the stress in the shock direction, leaving the stresses in the transverse directions unconstrained. Chapter IV discusses a method to infer applied stresses from x-ray diffraction patterns.

3.6.3 Material strength

The strength of a material describes its ability to support shear stresses and deviate from the hydrostatic response when subjected to an anisotropic stress. When modeling the stress applied to a material it is convenient to separate the stress tensor into hydrostatic and deviatoric components. The hydrostatic component provides the mean stress and the deviatoric component allows additional stress to be applied in the direction of compression. The decomposed stress tensor in the laboratory frame is written [43]

$$\sigma = \sigma_{\mathbf{h}} + \sigma_{\mathbf{d}} = \begin{pmatrix} \sigma_h & 0 & 0 \\ 0 & \sigma_h & 0 \\ 0 & 0 & \sigma_h \end{pmatrix} + \begin{pmatrix} -t/3 & 0 & 0 \\ 0 & -t/3 & 0 \\ 0 & 0 & 2t/3 \end{pmatrix}, \tag{3.73}$$

where $\sigma_{\mathbf{h}}$ and $\sigma_{\mathbf{d}}$ are the hydrostatic and deviatoric stress tensors and t is the uniaxial stress component. Using the von Mises yield criterion, the yield strength, σ_Y, and shear strength, τ_Y, are given by

$$\sigma_Y = 2\tau_Y = t. \tag{3.74}$$

The yield strength is the maximum difference in stresses the crystal can support between any two directions. For dynamic compression experiments, this corresponds to the difference between stresses in the loading direction and stresses in the trans-

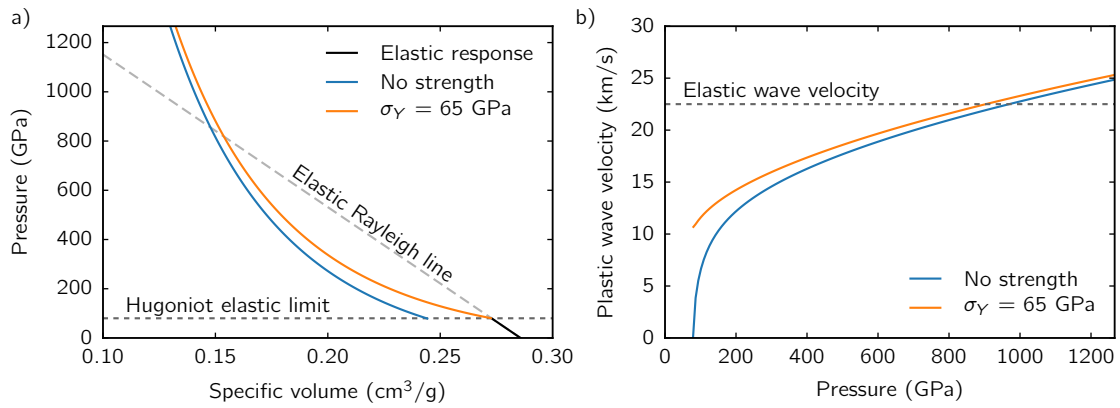

Figure 3.8: The effect of material strength in diamond, showing a) the change in overdrive stress calculated by the intersection of the elastic Rayleigh line and the Hugoniot and b) the calculated plastic wave velocity as a function of driving pressure for an example yield strength of $\sigma_Y = 65$ GPa.

verse directions.

At pressures above the HEL, there are two cases of crystal failure to consider: the elastic-hydrostatic and elastic-plastic responses. Complete loss of material strength defines the elastic-hydrostatic limit, creating a state of hydrostatic compression where the shocked material is unable to support any shear stresses. Alternatively, the elastic-plastic response is characterized by the retention of strength after initial yielding. Materials with high HELs are often brittle solids with low thermal conductivity, which tend to exhibit significant loss of strength under inelastic compression. This is thought to be a result of heat localized in shear zones, softening the lattice and possibly melting upon failure. Meanwhile, materials with lower HELs and high thermal conductivity, such as metals, typically retain more strength after the onset of plastic deformation. These materials allow thermal energy to dissipate before a catastrophic failure of the lattice occurs.

Figure 3.8a shows the shock-compression curve for diamond for the cases of no strength (the elastic-isotropic response, $\sigma_Y = 0$) and for the elastic-plastic case with $\sigma_Y = 65$ GPa. Rayleigh lines can be drawn to calculate the plastic wave velocity as

a function of driving pressure, using the HEL conditions as the initial state. Figure 3.8b shows the calculated plastic wave velocities as a function of driving pressure for each case.

3.7 Dynamic compression of materials using lasers

A number of experimental methods have been developed to produce shock waves to study the behavior of materials at high pressure. Early methods used high explosives, gas guns, and electromagnetic guns to launch projectiles at high speed to impact sample materials [2]. This thesis describes experiments conducted at high-energy laser facilities, and discussion of experimental methods is restricted to laser-driven dynamic compression.

3.7.1 Spatial drive considerations

Driving shocks using lasers requires a smooth spatial profile of the laser focus to create homogenous conditions that can be well characterized. Fluctuations in the spatial profile of the beam result in intensity variations on the irradiated surface, driving localized regions at higher pressures. In order to create uniform conditions, the laser drive must drive a planar shock.

Because drive pressure is a function of irradiance, the maximum power of the laser sets constraints on the pressures achievable for a minimum acceptable area of shock planarity. As the shock travels through the material the width of the planar region shrinks as rarefactions enter from the sides. Carefully considering the required spatial extent of the planar region to make accurate measurements with these constraints in mind is critical in performing well-characterized dynamic compression experiments.

Several approaches exist to increase the spot of the drive beam to increase the

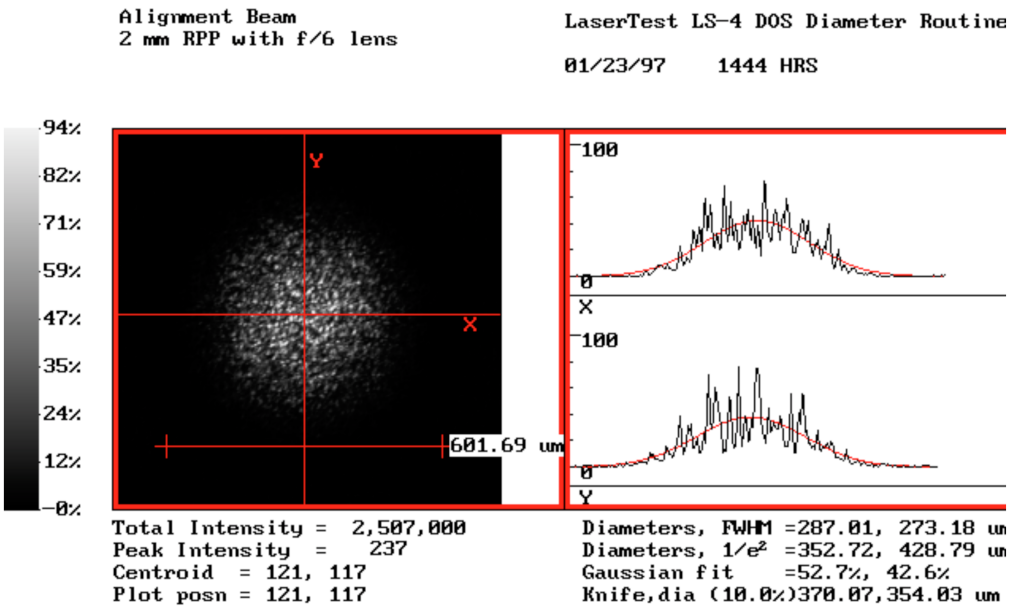

Figure 3.9: Example of a focal spot using a phase plate at the Trident laser facility [3]. The left side shows an image of the focal spot after a random phase plate with 2 mm hexagonal elements, focused with an f/6 lens and the right side shows intensity lineouts along the horizontal and vertical directions. The overlapping beamlets from the phase plate smooth the overall profile of the focal spot at the expensive of introducing high frequency structure. The high frequency spikes can be removed by allowing the shock front to anneal as it propagates.

spatial extent of the planar drive. A simple way to produce a larger focal spot is to defocus the beam on the target surface. This can help remove some spatial fluctuations, but it is not an ideal method to drive planar shocks because the intensity profile will have significant spatial structure created by phase variations introduced by optical components in the laser chain.

The experiments described in this thesis at LCLS and the Trident laser facility used phase plates to improve the spatial profiles of the drive beams. Phase plates smooth the spatial profile of laser beams by overlapping a large number of beams in the same region with different phases [44]. Phase plates consist of an array of elements with varying thicknesses, inducing phase delays in each transmitted beamlet. The apertures of the beamlets define a new length scale for the optic,

increasing the f-number of the optical system and setting the minimum spot size of the focused beam. Smaller spot sizes require larger phase plate elements, and therefore a beam with a given input diameter passes through fewer elements. The limited number of phase plate elements for small focal spots can lead to significant spatial structure in the focused beams. The overlapping profiles from the focused beamlets help to smooth the envelope of the focal spot, but they introduce high-frequency spatial structure in the beam. Figure 3.9 shows an image of a focal spot at the Trident laser facility using a random phase plate with 2 mm hexagonal elements and a f/6 focusing lens showing the high-frequency spatial structure in the intensity lineouts on the right. The high-frequency spatial structure introduced by phase plates can be removed by allowing the shock front to anneal as it propagates. This is usually done by allowing the shock to propagate through a separate ablator material before entering the sample layer.

3.7.2 Temporal pulse shape considerations

By varying the temporal profile of the drive laser, dynamic compression experiments can access a wide range of p-V space. These include accessing Hugoniot states via shock compression, as well as off-Hugoniot states using carefully designed pulse shapes.

The simplest case is that of a strong shock driven into a sample, with a constant driving force creating a uniform post-shock state. Over short timescales, a simple square pulse laser drive can achieve this. For steady shocks, the drive intensity must be increased throughout the drive to compensate for loss of driving pressure as the critical surface moves farther away from the shock front. Reaching off-Hugoniot states requires a more complicated pulse shape. By slowly ramping up the intensity of the drive laser, near isentropic compression can be achieved. Ramp compression experiments at the NIF reached pressures as high as 5 TPa [45].

3.8 Diagnostics for high pressure physics

3.8.1 Shock timing diagnostics

Early diagnostics for shock compression experiments measured the arrival time of the shock at various locations, allowing shock velocities to be calculated if the precise locations of the probes were known. Two examples of shock timing diagnostics are electrical pins and fiber optic pins. Charged electrical pins are discharged by the arrival of the shock and the resulting signal can be measured using an oscilloscope. Fiber optic pins work in a similar manner, but changes in optical behavior are recorded instead.

A more advanced technique, known as VISAR, or Velocity Interferometer System from Any Reflector [46, 47], simultaneously measures shock timing and surface velocities. VISAR works by using reflecting surfaces on the target in an interferometer setup and records interference fringes on an optical streak camera. Surface velocity histories and shock timing are encoded in the streaked interference fringes. By imaging a strip of the target, spatial structure in the shock can be measured and multiple surfaces within a target can be monitored simultaneously.

If the only goal of the VISAR system is to measure shock timing and planarity, the reference beam in the VISAR system can be blocked. This provides a streaked image with no fringes, where the shock arrival at a surface can be measured by a change in reflectivity. The lack of fringes removes the ability to measure surface velocities, but the absence of fringes provides much better spatial resolution while still measuring shock timing.

3.8.2 X-ray diagnostics

A variety of x-ray diagnostics have been developed to study shock-compressed matter. Here the discussion is limited to the techniques directly related to the work

presented in this thesis: x-ray diffraction (XRD), x-ray Thomson scattering (XRTS), and x-ray fluorescence (XRF).

XRD, discovered by Max von Laue in 1912, is a powerful diagnostic used to directly measure atomic structure by probing lattice dimensions [48]. XRD has been the standard technique to study statically compressed materials in diamond anvil cells. The nature of static compression experiments does not require a bright x-ray source for XRD studies, provided enough time for data collection. Diagnosing dynamic compression experiments with x-ray diffraction does not have this luxury, requiring bright x-ray sources capable of producing a sufficient flux of x-rays in the timescale of interest. The first time-resolved study of shock-compressed matter using XRD at a large-scale laser facility was published in 1987 [49], achieving time resolution of 100 ps using a He-α x-ray source. With the advent of x-ray free electron lasers, such as LCLS, dynamic compression experiments can now be diagnosed with XRD with time resolution of tens of femtoseconds. This timescale is shorter than the smallest phonon period in shocked systems, allowing lattice dynamics to be studied without temporal smearing.

XRTS can measure plasma conditions in dynamically compressed materials, such as density, temperature, and ionization. By using an imaging spectrometer these measurements can be made along the shock profile to infer density profiles [50] as well as plasma conditions in each layer of a shocked system [51].

XRF provides a measurement of ion density and ionization states present in the plasma system. An external source of x-rays induces XRF and the emission is imaged to measure the density of fluorescing ions [52]. Additionally, the ionization state of the fluorescing ions can be calculated from the spectral shift in the emission lines. Atomic kinetic models can then be used to infer plasma conditions via spectroscopic modeling. Chapter VI describes an XRF experiment and the detailed analysis of these measurements.

3.9 Conclusions

This chapter discussed the fundamentals of shock physics and the properties of compressed materials. EOS models were introduced as a method to relate thermodynamic properties of a system. Accurate EOS data are critically important for reliable models to be created for compressed states of matter. The chapter included a brief discussion of experimental considerations and diagnostics for shock-compression experiments.

CHAPTER IV

Calculation of diffraction patterns from highly stressed polycrystalline materials

4.1 Introduction

This chapter describes a method to calculate Debye-Scherrer diffraction patterns from highly stressed polycrystalline materials, the development of which was motivated by the capabilities of LCLS to probe shock-compressed matter. This work represents the first method to calculate Debye-Scherrer diffraction patterns for uniaxially compressed materials in the Reuss (iso-stress) limit beyond the small-stress limit and has been published in the Journal of Applied Physics [53].

Accurate measurements of the strength of materials at high strain rate are critical in predicting their response to the dynamic loading conditions present in these studies. X-ray diffraction provides a powerful technique for probing the structure of crystalline materials, enabling direct measurements of lattice strains and material strength. X-ray FELs, such as LCLS, are ideal x-ray sources to probe compressed states of matter with sufficient peak brightness for single shot measurements with $\sim$40 fs time resolution [54, 55]. The pulse duration of these x-ray pulses is shorter than the smallest phonon period in shocked systems, allowing lattice dynamics to be studied without temporal smearing. The monochromatic x-ray beams produced

by x-ray FELS require polycrystalline samples to produce Debye-Scherrer diffraction rings from a compressed lattice.

Diffraction from compressed crystalline materials has commonly been analyzed using a method originally presented by Singh [43] in the small-strain limit. For the highly strained conditions present in dynamic compression experiments, a method to model diffraction in the Voigt limit has been presented [56].

As discussed in Section 3.5.5, a Reuss limit model is particularly important for polycrystalline materials with elastic anisotropy, which have directionally dependent stress-strain relationships. In these cases, a distribution of strain states is present for a nonhydrostatic stress applied to the sample. This behavior is not included in Voigt limit models, which assume that the same strain tensor is applied to all crystallites, regardless of orientation within the sample. Additionally, the compression of polycrystalline materials consisting of multiple crystal structures with different elastic properties is better modeled in the Reuss limit, as illustrated in Figure 3.6.

Here, we present a method to calculate the diffraction pattern and lattice strains polycrystalline samples in the Reuss limit for highly stressed materials. This method takes the set of all initial crystallite orientations, defined by the initial texture of the sample, and applies the transformed stress tensor to each orientation before calculating the resulting diffraction pattern. With this method, we fit the applied stress tensor to diffraction data, enabling direct comparison to pressures measured experimentally or calculated using equation-of-state models. Examples illustrating the effect of probing geometry, deviatoric stresses, and sample texture on Debye-Scherrer diffraction patterns are given to show the versatility of this technique.

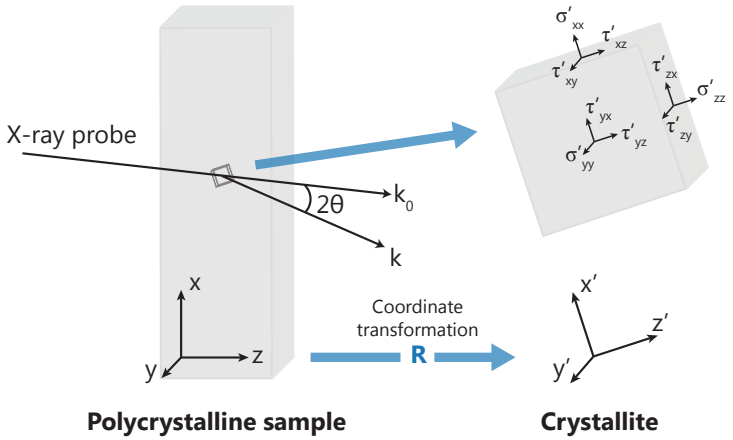

Figure 4.1: Definition of the coordinate systems used in this paper. The laboratory frame is unprimed and the coordinate system of the crystal lattice for a given crystallite within the sample is primed. The x-ray probe and diffracted wave vectors are $\mathbf{k}_0$ and $\mathbf{k}$ and the angle between them is defined as 2θ. The stress directions for the Cauchy stress tensor in the crystallite coordinate system, where shear stresses are nonzero after transformation from the laboratory frame, are also shown.

4.2 Application of the stress field

The critical component of the method presented here is the proper application of the stress tensor to each crystallite within the polycrystalline material. This requires the stress tensor, which is defined in the laboratory frame, to be properly transformed into the frame of each crystallite. To do this, we define three coordinate systems: the unprimed laboratory frame coordinates and the primed crystal lattice coordinate system as shown in Figure 4.1, as well as a diffraction coordinate system denoted by double primes described in the diffraction calculation section.

The applied stress tensor is defined in the laboratory frame by the Cauchy stress tensor, introduced in Section 3.5.1,

$$\sigma = \begin{pmatrix} \sigma_x & \tau_{xy} & \tau_{xz} \\ \tau_{yx} & \sigma_y & \tau_{yz} \\ \tau_{zx} & \tau_{zy} & \sigma_z \end{pmatrix}. \tag{4.1}$$

These stresses are illustrated in the crystallite coordinate system in Figure 4.1.

Transforming the stress tensor from the laboratory frame to the crystallite frame is required to correctly predict the lattice strains for materials with elastic anisotropy and enables the use of elastic constants to calculate lattice strains. A rotation matrix, **R**, defined between the two frames transforms the tensor to the crystallite frame. The Cauchy stress tensor is transformed between coordinate systems by

$$\sigma' = \mathbf{R}\sigma\mathbf{R}^T. \tag{4.2}$$

Here, we chose a rotation matrix using proper Euler angles and a z-y-z rotation,

$$\mathbf{R}(\alpha, \beta, \gamma) = \mathbf{R}_z(\gamma)\mathbf{R}_y(\beta)\mathbf{R}_z(\alpha), \tag{4.3}$$

where R_y and R_z are the standard rotation matrices about the y and z axes,

$$\mathbf{R}_y(\phi) = \begin{pmatrix} \cos\phi & 0 & \sin\phi \\ 0 & 1 & 0 \\ -\sin\phi & 0 & \cos\phi \end{pmatrix} \tag{4.4}$$

and

$$\mathbf{R}_z(\phi) = \begin{pmatrix} \cos\phi & -\sin\phi & 0 \\ \sin\phi & \cos\phi & 0 \\ 0 & 0 & 1 \end{pmatrix}. \tag{4.5}$$

where the angles between the coordinate systems depend on the orientation of each crystallite.

Calculating the lattice strains created by the stress tensor in the crystallite frame requires knowledge of the stress-strain relationship for the material. In principle, if this relationship is known for all stress states (including for all rotations) this method can be used to calculate the diffraction patterns for any stress. In practice, the stress-strain relationship is only known for specific conditions. In this chapter, we assume a known stress-strain relationship for the material under hydrostatic compression and calculate lattice strains for deviatoric stresses about the hydrostatic condition using elastic constants.

4.3 Diffraction calculation

For each compressed crystallite, the Laue diffraction condition determines which crystal planes will contribute to the diffraction signal. Working in reciprocal space, the reciprocal lattice vectors are given by

$$\mathbf{a}^* = \frac{2\pi}{V}\mathbf{b}' \times \mathbf{c}' \tag{4.6}$$

$$\mathbf{b}^* = \frac{2\pi}{V}\mathbf{c}' \times \mathbf{a}' \tag{4.7}$$

$$\mathbf{c}^* = \frac{2\pi}{V}\mathbf{a}' \times \mathbf{b}', \tag{4.8}$$

where $\mathbf{a}'$, $\mathbf{b}'$, and $\mathbf{c}'$ are crystal lattice vectors in real space (in the crystallite coordinate system) and V is the volume of the unit cell. The reciprocal lattice vector for a crystal plane with Miller indices (hkl) in the crystallite frame is defined as $\mathbf{G}' = h\mathbf{a}^* + k\mathbf{b}^* + l\mathbf{c}^*$ and d spacing of the crystal plane is given by $d = 2\pi/G'$.

As discussed in Section 2.3.2, the condition for Bragg scattering for a crystal plane with spacing d is given by $n\lambda = 2d\sin\theta_B$ and the Laue diffraction condition is given in the laboratory frame by $\mathbf{k} - \mathbf{k}_0 = \mathbf{G}$. The scattering intensity from

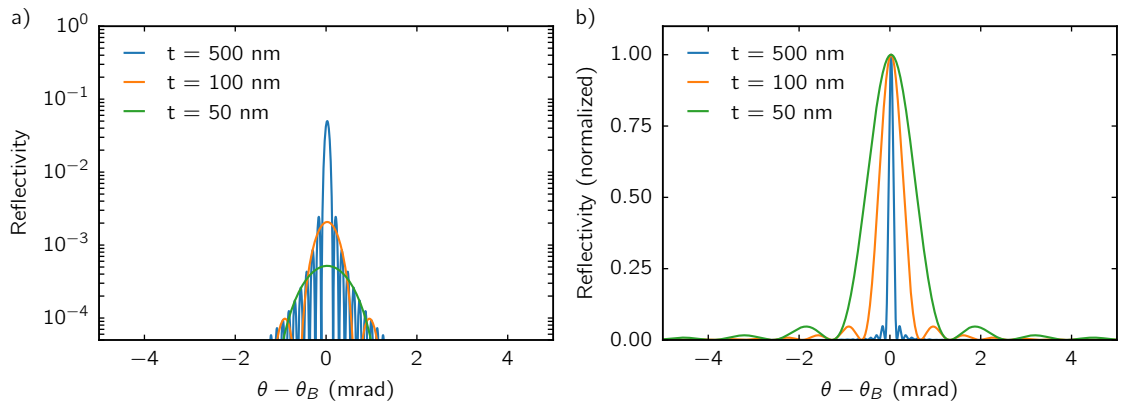

Figure 4.2: Rocking curves for diamond layers with thicknesses of 50, 100, and 500 nm for a 10 keV x-ray probe calculated using the XCRYSTAL package in XOP [4]. Thinner crystals have fewer layers to produce constructive interference, resulting in a) reduced reflectivity and b) increased FWHM for the diffraction peak.

a compressed diffraction plane is evaluated by sampling the rocking curve of the material at angle of incidence of the probe. The deviation from the ideal Bragg angle, $\Delta\theta_B$, is calculated by transforming $\mathbf{G}'$ to the laboratory frame ($\mathbf{G} = \mathbf{R}^T \cdot \mathbf{G}'$) and using the Bragg and Laue diffraction conditions, yielding

$$\Delta\theta_B = \arcsin\left(n\frac{G}{2k_0}\right) + \arcsin\left(n\frac{\mathbf{k}_0 \cdot \mathbf{G}}{k_0 G}\right). \tag{4.9}$$

Figure 4.2 shows example rocking curves for reflections from the (111) plane of uncompressed diamond at a probe energy at 10 keV, calculated using the XCRYSTAL package in XOP [4]. When the crystallite size is reduced the reflectivity of the plane decreases while the full width at half maximum (FWHM) of the diffraction peak increases. The diffracted in intensity for each plane is calculated by sampling these curves at the value given by Eq. (4.9). To improve the accuracy of the rocking curves, they should be calculated for the compressed unit cells. The spectral bandwidth and divergence of the probe source can be modeled in this step by sampling a distribution of $\mathbf{k}_0$ vectors.

Diffraction patterns can be visualized by plotting the intersection of the diffracted rays and the detector plane. For simplicity, we consider the plane normal to $\mathbf{k_0}$ at a distance L from the scattering point. The coordinates in the detector plane are denoted by double primes. Scattered wavevectors, $\mathbf{k}$, transformed into this frame are used to calculate the angular position around the diffraction ring, given by $\phi = \arctan(k''_y/k''_x)$. The diffraction pattern is converted to Cartesian coordinates using

$$x''/L = \tan 2\theta \cos\phi \tag{4.10}$$

$$y''/L = \tan 2\theta \sin\phi. \tag{4.11}$$

For the compressed crystallites contributing to the diffraction pattern, the lattice strains, diffraction angles, and diffracted intensities can be recorded.

4.4 Uniaxial compression

4.4.1 Strain calculation

Uniaxial compression is a common way to study materials at high pressure and is relevant to both diamond anvil cell and dynamic compression experiments. In uniaxial compression, off-diagonal stress tensor components in the laboratory frame can be disregarded and the Cauchy stress tensor is decomposed into hydrostatic and deviatoric components, as explained in Section 3.6.3,

$$\sigma = \sigma_{\mathbf{h}} + \sigma_{\mathbf{d}} = \begin{pmatrix} \sigma_h & 0 & 0 \\ 0 & \sigma_h & 0 \\ 0 & 0 & \sigma_h \end{pmatrix} + \begin{pmatrix} -t/3 & 0 & 0 \\ 0 & -t/3 & 0 \\ 0 & 0 & 2t/3 \end{pmatrix}. \tag{4.12}$$

The compression of the crystallites is calculated in two steps. First, we apply the hydrostatic stress component to all crystallites, scaling the crystal lattice by the compression calculated using a hydrostatic compression curve, which does not depend on crystallite orientation. For this step, each crystal lattice vector transforms as

$$\mathbf{v}_h' = \left(\frac{\rho_0}{\rho_h}\right)^{1/3} \mathbf{v}_0', \tag{4.13}$$

where $\mathbf{v_h}$ and $\mathbf{v_0}$ are the hydrostatically compressed and uncompressed lattice vectors and ρ_h and ρ_0 are the hydrostatically compressed and initial densities. For high-pressure conditions or materials with low strength, this will provide the majority of the compression of the crystal lattice. It is important to do this step before applying the deviatoric component, which requires the use of elastic constants and therefore should be treated as a perturbation on the compressed cell to minimize error.

Next, we apply the deviatoric component to the hydrostatically compressed unit cell. The resulting strains are calculated using elastic constants, which can be calculated using density functional theory (DFT) as a function of hydrostatic pressure. For a linear system, the lattice strains are calculated using

$$\sigma_d' = \mathbf{C}\epsilon_d' \tag{4.14}$$

where $\epsilon_\mathbf{d}'$ is the deviatoric strain tensor and $\mathbf{C}$ is the elastic stiffness tensor. For high-strength materials the deviatoric strains can be large and higher order elastic constants may be needed to properly model the system.

The strain tensor is applied to each crystal lattice vector in the hydrostatically compressed system by

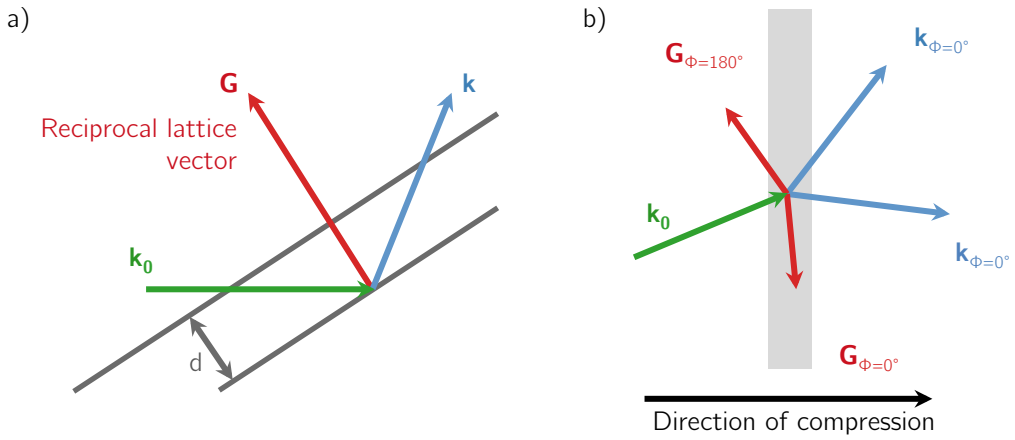

Figure 4.3: Diagram showing a) the direction of the reciprocal lattice vector, $\mathbf{G}$, which is normal to the diffracting planes in real space and b) the direction of $\mathbf{G}$ for diffraction observed at $\phi = 0°$ and $180°$. The uniaxial compression of lattice planes for materials with strength is proportional to $\mathbf{G} \cdot \hat{\mathbf{z}}$, resulting in higher compression at $\phi = 180°$ in this example.

$$\mathbf{v}' = \begin{pmatrix} 1+\epsilon'_{xx} & \epsilon'_{xy} & \epsilon'_{xz} \\ \epsilon'_{yx} & 1+\epsilon'_{yy} & \epsilon'_{yz} \\ \epsilon'_{zx} & \epsilon'_{zy} & 1+\epsilon'_{zz} \end{pmatrix}_d \mathbf{v}'_h \tag{4.15}$$

Combining the two steps, the lattice vectors transform following

$$\mathbf{v}' = \left(\frac{\rho_0}{\rho_h}\right)^{1/3} \left(\mathbf{C}^{-1}\sigma'_d\right) \mathbf{v}'_0. \tag{4.16}$$

4.4.2 Diffraction calculation

The direction of the probe vector in uniaxial compression experiments using a collimated x-ray source can be defined by a single parameter, χ, which is the angle between the direction of compression and the probe vector. In this case, the diffracted rays are transformed into the diffraction coordinate system by $\mathbf{k}'' = \mathbf{R}_y(-\chi) \cdot \mathbf{k}$.

For off-normal probing ($\chi \neq 0°$), the 2θ diffraction angle for a given plane can

vary as a function of ϕ. This dependence is a direct result of material strength and can be used to infer strength from diffraction measurements. Figure 4.3 shows a) the physical representation of the reciprocal lattice vector, G, which is normal to the diffraction plane and b) the direction of $\mathbf{G}$ for a given diffraction plane at $\phi = 0°$ and $180°$. If the uniaxial compression is along the z direction, the compression of a plane is proportional to $\mathbf{G} \cdot \hat{\mathbf{z}}$, which varies as a function of ϕ. In this example, it is clear that the planes contributing to diffraction at $\phi = 180°$ would be in a higher state of compression than those contributing to $\phi = 0°$ due to this effect. If a material has no strength compression is equal in all directions and this effect vanishes.

4.5 Example: shock compressed diamond

The response of diamond to shock compression is of particular interest to ICF because it is a candidate for the ablator material at NIF [57]. Diamond is also an interesting material to study because it has the highest strength of any elemental solid, and is thought to exist in large quantities in the ice layers of giant planets [58]. For these reasons, diamond has been the subject of a number of dynamic compression studies [38, 45, 59–61]. We consider the case of polycrystalline diamond uniaxially compressed to $\sigma_h = 200$ GPa probed with a collimated 10 keV x-ray probe to illustrate how this analysis is applied.

4.5.1 Coordinate transformation

First, we calculate the rotation matrix between the sample coordinate system and a crystallite with the vector $[hkl]'$ aligned along the z direction. Figure 4.7 shows this geometry and the orientations sampled. The rotation of the crystallite about this vector is given by the angle α, where we define $\alpha = 0$ when x' lies in the

xz plane, fully constraining the coordinate system without loss of generality. Given these conditions, the rotation angles between the two coordinate systems for cubic unit cells (such as diamond) are

$$\beta = \cos^{-1}\left(\frac{l}{\sqrt{h^2+k^2+l^2}}\right) \tag{4.17}$$

$$\gamma = \cos^{-1}\left(\frac{h}{\sqrt{h^2+k^2}}\right). \tag{4.18}$$

and α ranges from 0 to 2π radians to account for rotations of the crystallite about the $[hkl]'$ vector.

4.5.2 Lattice strain calculations

Here we assume a sample compressed to a mean stress of 200 GPa shocked in the z direction. The corresponding applied stress tensor is given by

$$\sigma = \begin{pmatrix} 200 & 0 & 0 \\ 0 & 200 & 0 \\ 0 & 0 & 200 \end{pmatrix} \text{GPa} + \begin{pmatrix} -t/3 & 0 & 0 \\ 0 & -t/3 & 0 \\ 0 & 0 & 2t/3 \end{pmatrix}, \tag{4.19}$$

where the uniaxial stress component, t, has been left as a variable to demonstrate how the deviatoric stress affects the diffraction pattern.

We assume the initial properties of polycrystalline diamond, $\rho_0 = 3.515$ g/cm^3 and $a_0 = 3.56683$ Å. Following the method described for uniaxial compression, we apply the hydrostatic component, which gives the new lattice parameter of the cell. Using the hydrostatic DFT results shown in Figure 4.4, the density is 4.55 g/cm^3, or a compression of 1.29, corresponding to a compressed lattice vector of $a = a_0(\rho_0/\rho)^{1/3} = 3.27$ Å.

Next, we apply the deviatoric stress tensor to the hydrostatically compressed di-

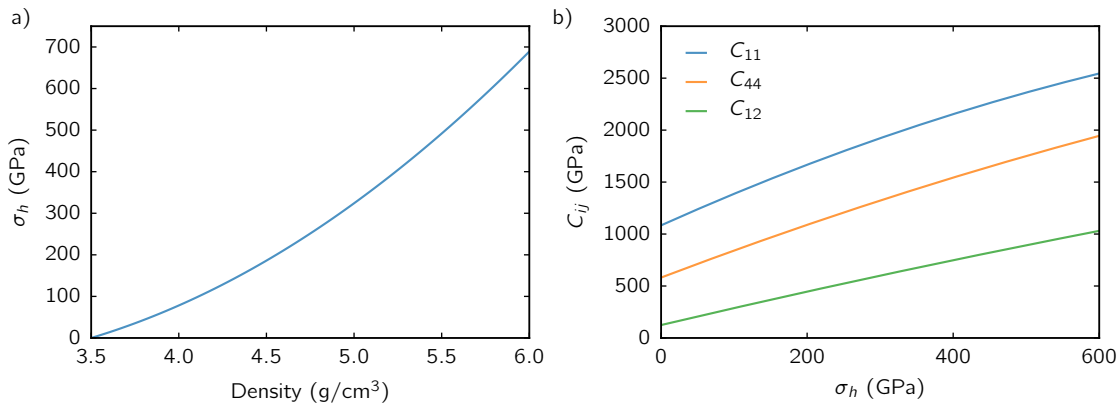

Figure 4.4: DFT calculations of the a) hydrostatic cold curve and b) elastic constants as a function of hydrostatic pressure for diamond. DFT calculations performed by Jan Vorberger.

amond crystallites. The symmetry of cubic crystal systems reduces the number of independent elastic constants to three: C_{11}, C_{12}, and C_{44}. The stress-strain relationship is thus

$$\begin{pmatrix} \sigma'_{xx} \\ \sigma'_{yy} \\ \sigma'_{zz} \\ \tau'_{yz} \\ \tau'_{zx} \\ \tau'_{xy} \end{pmatrix} = \begin{pmatrix} C_{11} & C_{12} & C_{12} & 0 & 0 & 0 \\ C_{12} & C_{11} & C_{12} & 0 & 0 & 0 \\ C_{12} & C_{12} & C_{11} & 0 & 0 & 0 \\ 0 & 0 & 0 & C_{44} & 0 & 0 \\ 0 & 0 & 0 & 0 & C_{44} & 0 \\ 0 & 0 & 0 & 0 & 0 & C_{44} \end{pmatrix} \begin{pmatrix} \epsilon'_{xx} \\ \epsilon'_{yy} \\ \epsilon'_{zz} \\ \gamma'_{yz} \\ \gamma'_{zx} \\ \gamma'_{xy} \end{pmatrix}. \tag{4.20}$$

The elastic constants from DFT as a function of hydrostatic pressure shown in Figure 4.4 can then be used to calculate the lattice stains and compressed lattice vectors. Accounting for shearing, the strained cubic unit cell is a parallelepiped, with a volume given by $V = \mathbf{a}' \cdot \mathbf{b}' \times \mathbf{c}'$ and the compression of the unit cell for each initial orientation can be calculated using $\rho/\rho_0 = a_0^3/V$.

4.5.3 Density functional theory calculations

The DFT calculations presented in this chapter were performed by Jan Vorberger and are not the work of the author. Here the details of the calculations are presented for completeness. The computation of the elastic constants of diamond at various hydrostatic pressures is performed using the DFT implementation as available in the package abinit [62]. All calculations were performed with a parallel implementation of abinit at the National Energy Research Scientific Computing Center (NERSC) [63]. Figure 4.4 shows the results of these calculations.

The actual calculation of the elastic constants relies on a linear response formalism [64]. We have used norm-conserving Troullier-Martins type pseudopotentials from the Fritz-Haber-Institute (FHI) database with four electrons taken into account explicitly [65]. The electronic wave function was represented using plane waves with a cutoff of $E_{cut} = 35$ Ha. The self-consistency loop for the electronic density was enforced to 10^{-18} in the residual of the potential and 10^{-20} in the wave function convergence, respectively. The exchange correlation potential was taken in PBE parametrization of the generalized gradient approximation [66]. Standard Monkhorst-Pack k-point sampling with $32 \times 32 \times 32$ k-points was invoked. The lattice constant was adjusted so as to give the desired hydrostatic pressure on the diamond unit cell consisting of two atoms (space group Fd$\bar{3}$m) before invoking the response function calculation of the elastic constants.

For diamond at σ_h = 200 GPa the values calculated were $C_{11} = 1670$ GPa, $C_{12} = 446$ GPa, and $C_{44} = 1090$ GPa.

4.5.4 Diffraction calculation

With the compressed lattice vectors defined, diffraction patterns can be calculated. Figure 4.5 shows examples of the diffraction patterns calculated for polycrystalline diamond with no texture under uniaxial compression with $\sigma_h = 200$ GPa

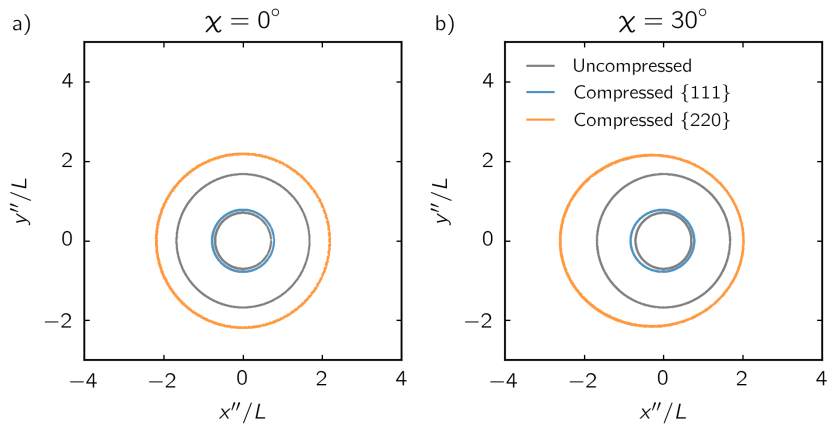

Figure 4.5: Debye-Scherrer diffraction patterns calculated for uniaxially compressed diamond with $\sigma_h = 200$ GPa and $t = 100$ GPa probed with a collimated 10 keV x-ray source a) aligned with the direction of compression ($\chi = 0°$) and b) at $30°$ off-normal. When $\chi \neq 0°$ the compression of the diffracting planes depends on ϕ and the diffraction pattern becomes asymmetric.

and $t = 100$ GPa probed with a collimated 10 keV x-ray source a) aligned with the direction of compression ($\chi = 0°$) and b) for $\chi = 30°$. When $\chi \neq 0°$ the compression of the diffracting planes depends on ϕ as a result of the distribution $\mathbf{G}$ vector orientations satisfying the diffraction condition.

Next, the diffraction is calculated with t as a parameter to show the effect of strength on Debye-Scherrer diffraction patterns. Figure 4.6 shows the calculated diffraction for diamond compressed to a hydrostatic pressure of 200 GPa and $t =$ 0, 50, and 100 GPa. When $t = 0$ (hydrostatic compression) all crystallites are compressed identically, resulting in a single 2θ diffraction angle with no ϕ dependence. When t is nonzero the compression of the crystallites depends on initial orientation, creating a ϕ dependence and broadening diffraction in 2θ. This broadening is a result of the distribution of strain states created by the anisotropic stress applied to the polycrystalline sample. The Voigt limit prediction is shown for the strain tensor calculated for the unrotated stress tensor using the DFT results. The strains used in the Voigt calculations are $\epsilon_z = \epsilon_x = 0.0937$ for $t = 0$ GPa, $\epsilon_z = 0.121$ and $\epsilon_x = 0.0805$

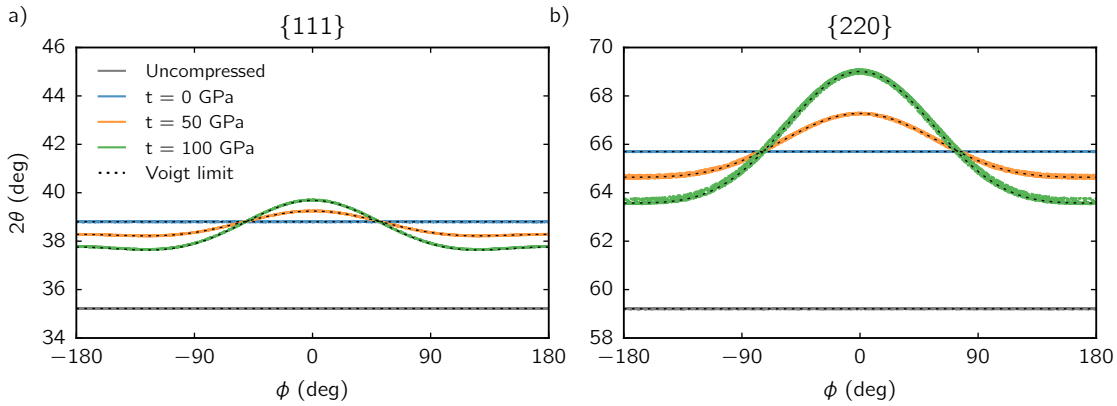

Figure 4.6: Diffraction calculations for polycrystalline diamond for $\sigma_h = 200$ GPa and t = 0, 50, and 100 GPa probed with 10 keV x-rays with $\chi = 30°$. 2θ plotted as a function of ϕ for a) $\{111\}$ and b) $\{220\}$ diffraction. The width of the peaks in 2θ broadens with increasing t as a result of the distribution of strain states created by the increasingly anisotropic stress on the range of initial crystallite orientations, which is not present in the Voigt limit prediction (dashed).

for $t = 50$ GPa, and $\epsilon_z = 0.148$ and $\epsilon_x = 0.0667$ for $t = 100$ GPa, where all strains are given in compression and it is assumed that the strains in the transverse directions are equal ($\epsilon_x = \epsilon_y$).

4.5.5 Texture effects

The texture of a polycrystalline material defines the distribution of crystallite orientations within the sample. Methods used to produce polycrystalline materials, such as chemical vapor deposition growth or rolling, often create characteristic textures. The properties of a crystalline material, such as strength and wave propagation, can be significantly affected by texture [67].

Including texture in the prediction of diffraction from highly strained polycrystalline materials has been explored in the Voigt limit [68]. Here we work in the Reuss limit, thereby including the effects of elastic anisotropy when calculating the response of each crystallite orientation within the sample. In doing so, we avoid having to measure or calculate the bulk and shear moduli for each texture case to

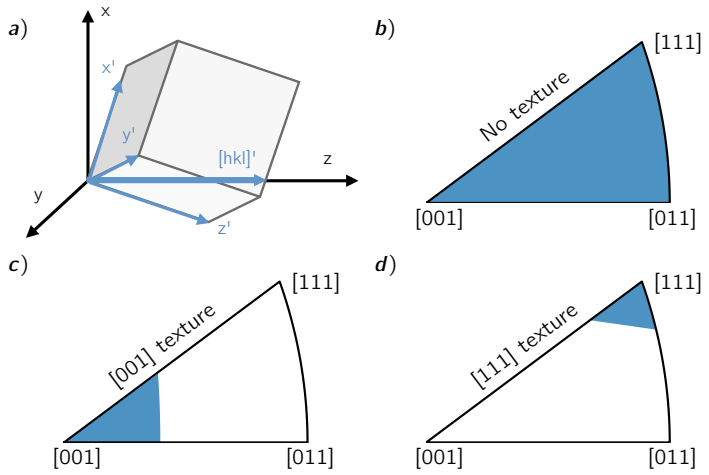

Figure 4.7: Crystallites with different initial orientations are sampled to calculate the diffraction from the polycrystalline sample. a) Each iteration calculates diffraction from a crystallite with lattice vector $[hkl]'$ aligned with z. Three texture cases were analyzed and their orientation distribution functions were represented by inverse pole figures. The three cases were: b) no texture, where all crystallite orientations are sampled equally, c) preferred [001] texture, and d) preferred [111] texture where the shaded regions represent the orientations included in each case.

accurately model the stress-strain relationship of the material. In this method, the elastic constants are calculated only once and can be applied to any texture case.

Material texture can be characterized using an orientation distribution function (ODF), defining the probability distribution of crystallite orientations. In this method, we use the ODF to weight the scattering intensity from each initial crystallite orientation. We define crystallite orientation by the $[hkl]'$ vector aligned with the surface normal, z.

The cubic symmetry of diamond reduces the possible crystallite orientations to the projection into a space bound by [001], [011], and [111] directions. Figure 4.7 shows inverse pole figures illustrating the three example textures examined in this study: b) no texture, defined by a completely random distribution of crystallite orientations, c) a sample with [001] texture, and d) a sample with [111] texture where the shaded regions indicate the initial orientations present in each texture case. The diffraction from the complete set of equivalent planes must be calculated when utilizing crystal symmetry to reduce the set of initial orientations. For example, diffraction from the $\{111\}$ family of planes in a cubic system must include diffraction from (111), $(11\bar{1})$, $(1\bar{1}1)$, $(\bar{1}11)$, etc.

Figure 4.8 shows diffraction from 10 keV probe x-rays at $\chi = 30^\circ$ for each of these texture cases with $\sigma_h = 200$ GPa and $t = 100$ GPa. Diffraction patterns are plotted in Cartesian coordinates for a) the [001] and b) [111] texture cases. These plots show gaps in the diffraction patterns, demonstrating the importance of knowing the initial texture of the sample when choosing detector locations. Diffraction from the $\{220\}$ planes is shown as a function of ϕ for each texture case as well as the Voigt limit for the untextured case, showing the differences in 2θ from the elastic anisotropy of diamond. The [111] texture case has a larger range of 2θ angles, suggesting that compressing diamond along the [111] direction creates a larger distribution of strains than when compressed along the [001] direction.

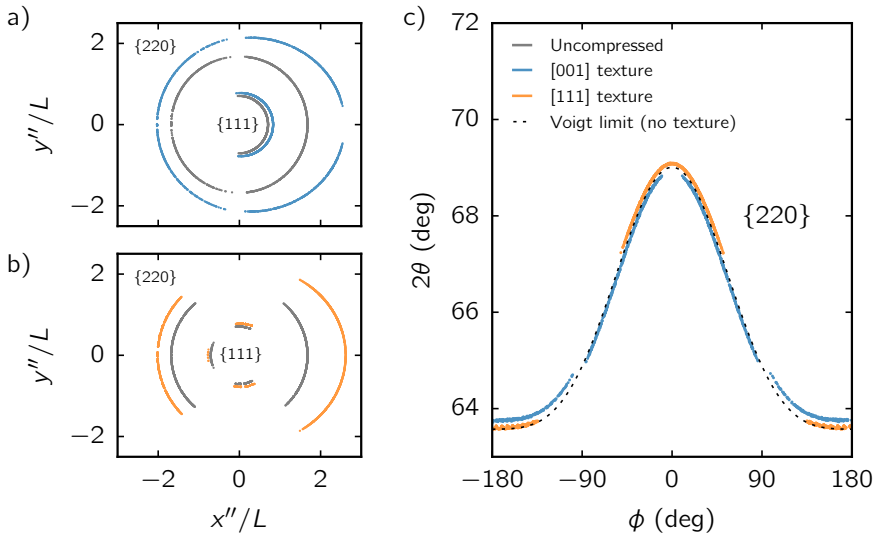

Figure 4.8: Diffraction patterns from {111} and {220} planes for polycrystalline diamond under uniaxial compression with $\sigma_h = 200$ GPa and $t = 100$ GPa probed with 10 keV x-rays at $\chi = 30°$ shown in detector coordinates for a) [001] sample texture and b) [111] sample texture and c) {220} diffraction plotted for both texture cases as a function of ϕ and the Voigt limit for the untextured case. The difference in 2θ for the two texture cases results from different final compression states for the initial textures.

4.5.6 Strength calculations

Material strength is an important material property that can be studied using dynamic compression. If the stress tensor applied to a material can be determined using time-resolved x-ray diffraction the strength is obtained by calculating t in Eq. (4.12). The deviations in 2θ scattering as a function of ϕ provide a direct measure of material strength, as illustrated in Figure 4.6. If the material is probed at $\chi = 0^\circ$, the Rankine-Hugoniot shock conditions can be used to supplement diffraction measurements to infer material strength.

Here, we consider a shock compression experiment where the time-resolved x-ray diffraction from the $\{111\}$ planes at a probing angle of $\chi = 0^\circ$ and the plastic deformation wave velocity are measured. Assuming known elastic precursor conditions (pressure and shock velocity), the Rankine-Hugoniot shock conditions can be used to calculate the post-shock stress of the plastic wave in the shock direction as a function of plastic wave velocity from Eq. (3.72)

$$\sigma_{z2} = \rho_0 D_1 u_1 + \rho_1 \left(D_2 - u_1\right)\left(u_2 - u_1\right). \tag{4.21}$$

Figure 4.9 shows the pressure-density curve for a plastic wave velocity of 16 km/s with elastic precursor conditions of D_1 = 20 km/s and σ_{z1} = 80 GPa, which have been previously measured in shock-compressed diamond [61]. The dashed line shows the elastic response of diamond and the solid line is defined by Eq (4.21).

The solid blue line in Figure 4.9 shows the hydrostatic behavior of diamond calculated using DFT. The hydrostatic response gives σ_h and Eq. (4.21) defines the stress in the shock direction, which is $\sigma_h + 2t/3$. These two stress values fully define the stress tensor in the laboratory frame given by Eq. (4.12) as a function of material density.

In the case of normal probe incidence ($\chi = 0^\circ$), 2θ has no ϕ dependence and the

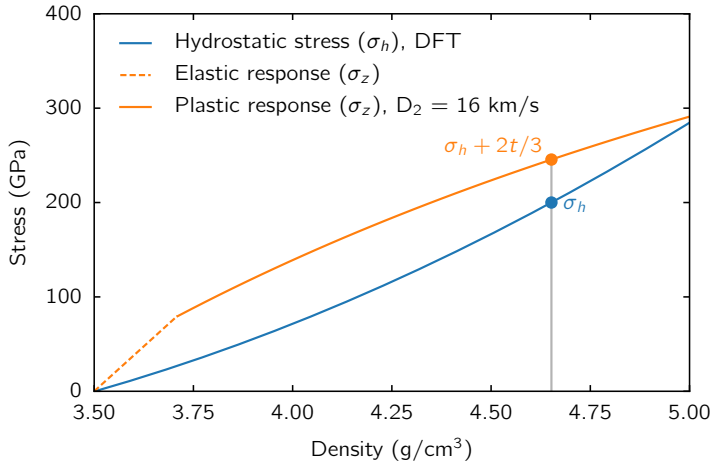

Figure 4.9: Pressure-density relationships for hydrostatically compressed diamond, calculated using DFT (blue) and planar shock Hugoniot calculations using Eq. (4.21) for an elastic precursor with $D_1 = 20$ km/s and $\sigma_{z1} = 80$ GPa and a plastic deformation wave with $D_2 = 16$ km/s (orange). For a given material density, σ_h and t are known and the stress tensor for uniaxial compression defined by Eq. (4.12) is fully defined.

Debye-Scherrer diffraction ring can be represented by a plot of scattered intensity as a function of 2θ. Figure 4.10 shows the mean 2θ diffraction angle for each density. The measured 2θ diffraction peak from the $\{111\}$ planes can be compared to Figure 4.10 and the material density can be inferred. The difference in density inferred with strength compared to hydrostatic compression can be rather large as illustrated by the example of a measured 2θ of $37.9°$, resulting in a 5.5% difference in density. The stress tensor applied to produce the inferred density state is known from Figure 4.9 and the yield strength and distribution of lattice strains can be calculated for the applied stress tensor. In this example we calculate the yield strength to be $\sigma_Y = t = 68$ GPa and $\sigma_h = 200$ GPa.

4.6 Conclusion

This chapter presented a method to calculate Debye-Scherrer diffraction patterns from highly stressed polycrystalline materials. Example diffraction patterns

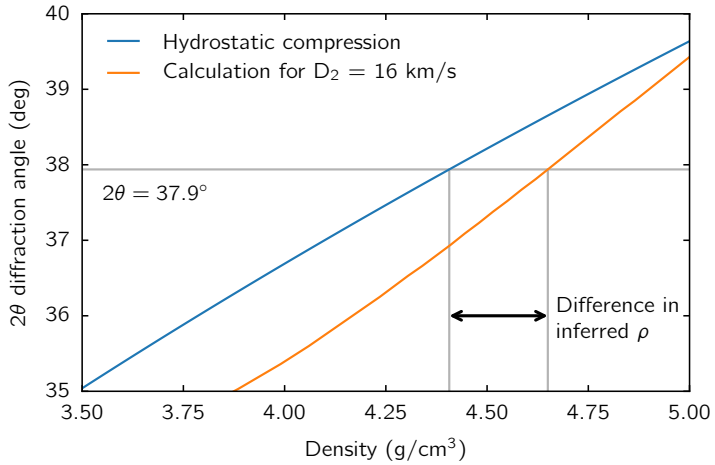

Figure 4.10: Calculated $\{111\}$ diffraction from polycrystalline diamond probed at 10 keV and $\chi = 0$ under hydrostatic compression (blue) and mean 2θ diffraction angles calculated for a plastic deformation wave velocity of $D_2 = 16$ km/s and an elastic precursor with $D_1 = 20$ km/s and $\sigma_{z1} = 80$ GPa (orange). The difference in inferred density for a measured 2θ of 37.9° with and without strength is illustrated.

for cases with different probe geometries, deviatoric stresses, and initial sample textures illustrate the robust nature of this method. Comparisons to the Voigt limit show where the Voigt and Reuss limits differ and the validity of these models could be tested. By working in the Reuss limit and applying stresses to all initial crystallite orientations, peak widths resulting from elastic anisotropy can be calculated. This flexible analysis predicts diffraction from materials with any texture and a wide variety of stress conditions in the Reuss limit.

This technique can be applied to the case of polycrystalline diamond under uniaxial compression. Using the elastic constants calculated with DFT and shock Hugoniot equations, we demonstrated how this analysis can calculate strength from diffraction measurements using data from a single diffraction plane. These results illustrate how strength can have a significant impact on material density inferred from diffraction measurements.

CHAPTER V

Dynamic strength measurements of shock-compressed diamond at LCLS

5.1 Introduction

Diamond is a candidate material for the ablator in ICF implosion capsules. Accurately modeling the initial compression phase of these implosions requires a detailed understanding of the strength of diamond. In particular, the behavior of shock-compressed diamond near the HEL is not well understood and additional data in this regime would be extremely useful to improve existing models and simulation codes. For this reason, an experiment was carried out at the MEC instrument at LCLS to study the behavior of shock-compressed polycrystalline diamond near the HEL. The experiment was conducted in May 2016, receiving VISAR-only preparation time to test the experimental configuration and two 12-hour x-ray shifts to collect diffraction data. This experiment was conducted shortly before the writing of this thesis, and thus this chapter will only describe the experimental platform developed to make strength measurements using x-ray diffraction and VISAR at LCLS and present preliminary results.

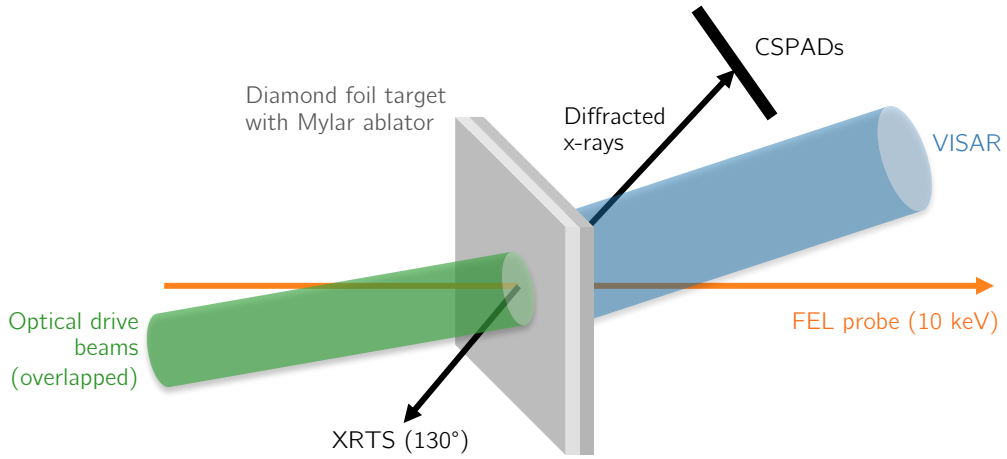

Figure 5.1: Experimental setup for the experiments conducted at MEC. The long pulse beams drove planar shocks into layered foil targets consisting of a Mylar ablator and polycrystalline diamond. CSPADs measured diffraction of the 10 keV probe from several crystallographic planes in diamond. VISAR measured shock and free-surface velocities and XRTS was fielded at a scattering angle of 130° to measure the temperature of the shocked diamond.

5.2 Experimental setup

The experiment was performed using the standard configuration for diffraction measurements at the MEC instrument. Figure 5.1 shows a schematic of the experimental setup. The two Nd:glass lasers at MEC were overlapped on the target to increase the drive intensity and smooth out spatial uniformities in the beam profiles. Both beams were 10 ns in duration in the second harmonic ($\lambda = 527$ nm) with a square temporal pulse shapes to drive a steady shock. Phase plates producing 150 and 250 μm focal spots were used to drive planar shocks with planar regions larger than the focal spot of the FEL. The 250 μm phase plates were used for low pressure shots and the 150 μm phase plates were used to extend the pressure range of the study. Typical shots had combined laser energies of $\sim$25 J, yielding irradiances up to 1.5×10^{13} W/cm^2.

The FEL was operated in SASE mode at 10 keV and tuned for maximum pulse energy of $\sim$2 mJ, corresponding to a pulse duration of $\sim$50 fs. The FEL was 30°

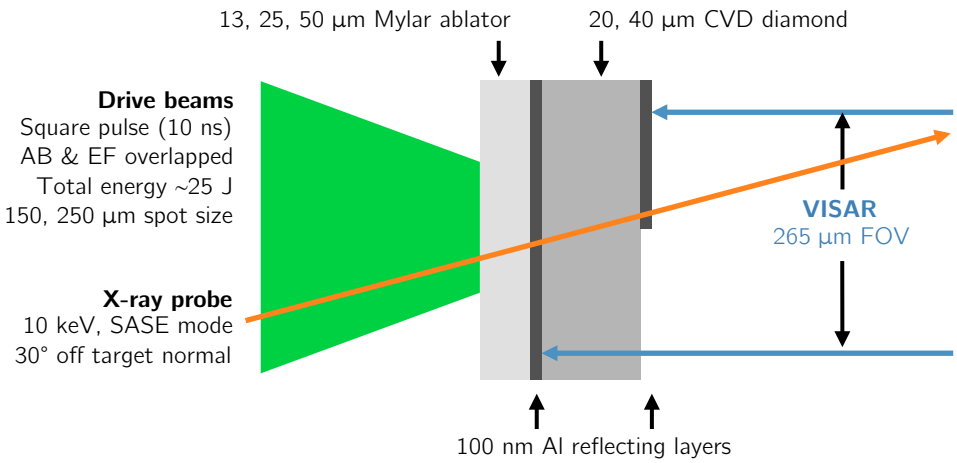

Figure 5.2: Schematic of the target design used in the MEC experiments. Two 10 ns laser beams irradiated a Mylar ablator to drive planar shocks with varying intensities. 10 keV x-rays from LCLS probed the compressed diamond layers and an internal aluminum reflector was used for shock timing with VISAR with a field of view (FOV) of 265 μm. A half-aluminized rear surface provided a second timing fiducial to measure the shock transit time through the diamond layer for each shot.

off-normal from the target surface ($\chi = 30°$), allowing strength to be inferred from variations in diffraction angle as a function of ϕ, as illustrated in Figure 4.6. The spot size of the FEL was varied from 10–50 μm, depending on the expected extent of the planar shock region for each drive condition.

5.2.1 Target design

The targets consisted of polycrystalline diamond, a Mylar ablator, and one or two thin layers of 100nm aluminum to act as reflecting surfaces for the VISAR beam. The diamond foils were provided by Applied Diamond Inc. and were synthesized using chemical vapor deposition (CVD). This experiment used diamond foils with thicknesses of 20 and 40 μm to measure shock velocities using transit times over the two lengths. Figure 5.3 shows an example scanning electron microscope (SEM) image of the CVD diamond. The SEM measurements show that the average grain size less than 50 nm.

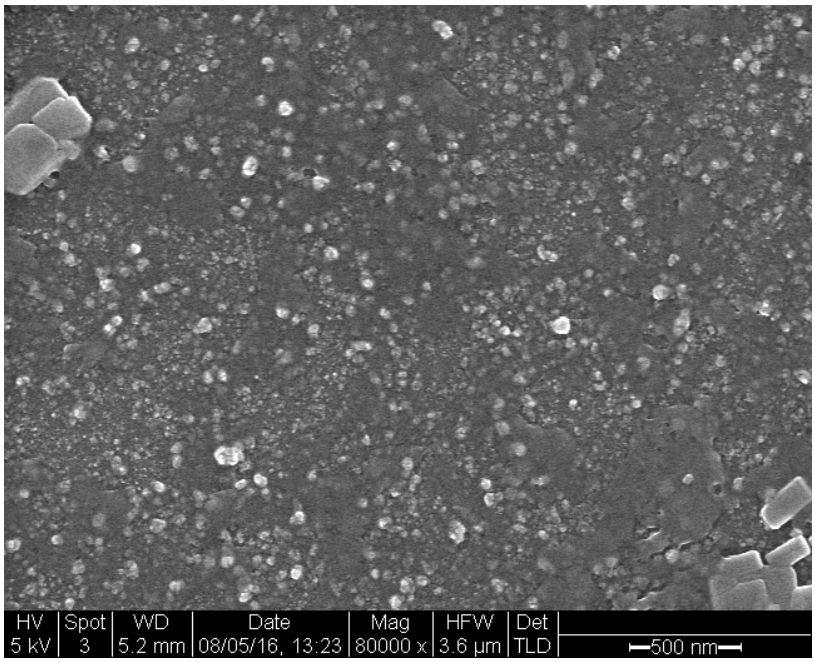

Figure 5.3: Scanning electron microscope image showing the surface of a polycrystalline diamond foil supplied by Applied Diamond Inc. Analysis of this image yields an average grain size of less than 50 nm in diameter. Image taken by Lauren Barmore.

The purpose of the Mylar ablator was to reduce the amplitude of the small-scale structure in the focal spot created by the phase plates. Three ablator thicknesses were chosen: 13, 25, and 50 μm, where the thicker ablators provided more time for the shock front to anneal, while the thinner ablators produced a larger planar shock region in the diamond. The width of the planar region required by the x-ray probe sets a maximum thickness of the ablator and diamond foil. The angle at which the edges converge is typically assumed to be 45° [69]. Figure 5.4 shows the predicted width of the planar shock front using 150 and 250 μm phase plates assuming converging angles of $45°$ and $60°$ for the Mylar ablator thicknesses. From this analysis, it is evident that the 150 μm phase plate should not be used with the 50 μm ablator, as the shock is no longer planar when it reaches the rear surface, even in the case of a 45° converging angle.

Aluminum layers added to the targets served as reflecting surfaces for the VISAR

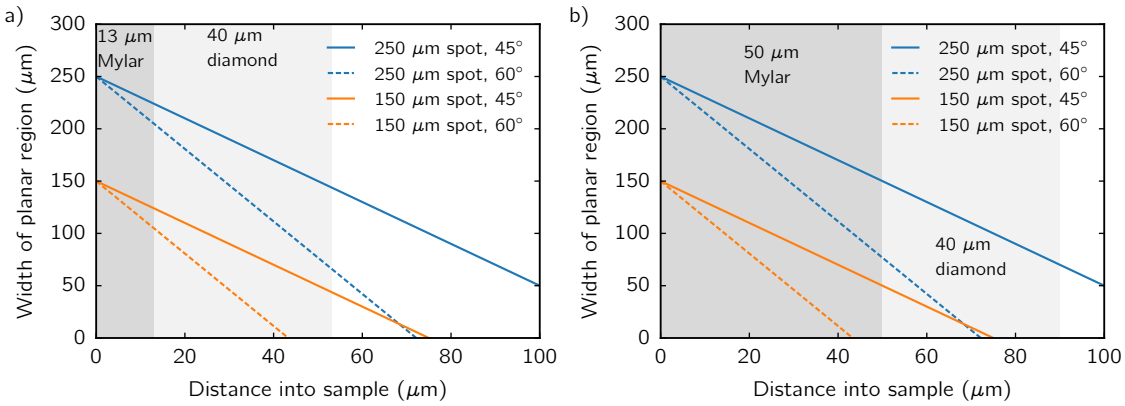

Figure 5.4: Predicted widths of the planar regions for shocks driven with 150 and 250 μm phase plates for a) 13 μm and b) 50 μm Mylar ablators. Widths are plotted in each case for the converging angles of 45° and 60°. This analysis shows that the 150 μm phase plates do not provide a large enough drive to be used with the 50 μm Mylar ablator targets.

diagnostic. Each target had a 100 nm layer of Al between the Mylar ablator and the diamond foil to precisely measure the time at which the shock entered the diamond. This layer was also used to measure shock planarity during VISAR-only shifts to determine the required Mylar thickness for each drive condition. Many targets included a 100 nm Al layer covering half the rear surface of the diamond to measure the shock breakout time. The half layer was oriented such that edge was perpendicular to the VISAR imaging direction, as shown in Figure 5.2, imaging both reflecting surfaces for each shot.

5.2.2 Diagnostics

The primary diagnostics for the experiment were Cornell-SLAC Pixel Array Detectors (CSPADs) [70, 71], placed around the target to detect scattered x-rays over the range $2\theta = 25°$ to $100°$. This coverage area of the CSPADs included diffraction from the {111}, {220}, and {311} planes in diamond using the 10 keV probe. Figure 5.5 shows predicted Debye-Scherrer diffraction patterns for $\sigma_h = 200$ GPa and $t = 0$ and 100 GPa, where the shaded regions indicate the coverage of the CSPADs.

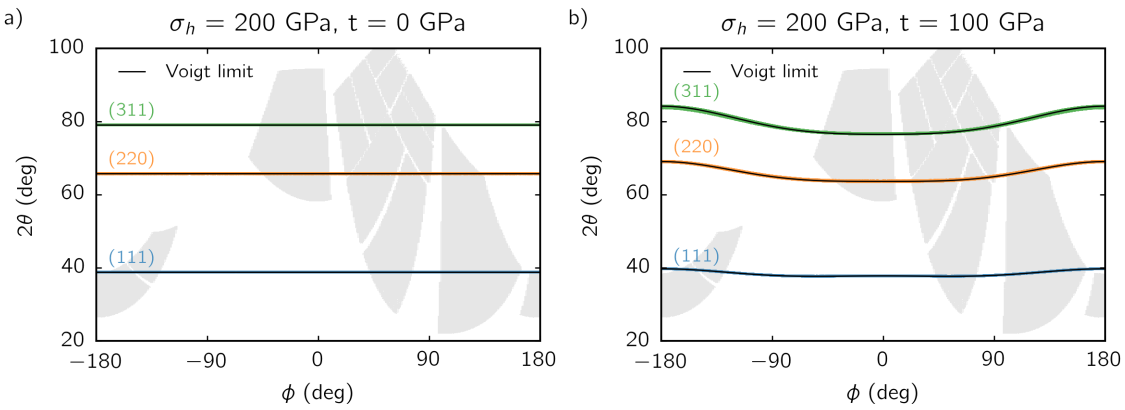

Figure 5.5: Calculated Debye-Scherrer diffraction patterns for compressed diamond from the (111), (220), and (311) planes for $\sigma_h = 200$ GPa and a) $t = 0$ GPa (hydrostatic compression) and b) $t = 100$ GPa. The shaded regions show the area covered by the CSPADs in the standard configuration. The colored lines are calculated in the Reuss limit using the method described in Chapter IV and the solid black lines show the corresponding Voigt limit calculations.

Low energy x-rays produced by the ablation plasma were attenuated by placing 100 μm of aluminum over each CSPAD.

The standard VISAR setup at MEC provided shock timing and free-surface velocity measurements. Two VISAR streak cameras (V1 and V2) used 10 ns sweep windows and fused silica etalons of thicknesses 8.087 and 5.072 mm. Photodiodes measured the pulse shapes and energies of the drive beams using leakage through mirrors after the final amplifiers.

The XRTS spectrometer measured scattering at 130° with 200 μm Be, 2.5 μm Al, and 27 μm polyimide filtering. The XRTS used a curved HOPG (Highly Oriented Pyrolitic Graphite) crystal in the von Hamos geometry. XRTS was included as an additional diagnostic to measure the temperature of the shocked diamond. This information can be used in future DFT simulations to quantify the effect of the increased temperature in the plastic wave.

5.3 Hydrodynamic simulations

HYADES simulations provided estimates of the pressures and densities achievable using the available drive conditions. Figure 5.6 shows an example HYADES run, predicting compressed densities around 5 g/cm^3 and pressures approaching 300 GPa. This simulation assumed a drive intensity of 60% the actual drive intensity, which has been shown to be a good value to compare HYADES simulations to experimental data of planar shocks [72]. This value will clearly depend on a number of factors, but here we are mostly interested in the approximate conditions we will achieve in the experiment. Additionally, HYADES is a hydrodynamic code and does not account for strength effects, as seen by the lack of an elastic precursor in the simulation. These simulations predict pressure gradients that increase as the shock propagates through the diamond layers. Pressure gradients are modeled by integrating diffraction calculations from a distribution of stress states, weighting contributions from each state appropriately. This gradient could be reduced by carefully tuning the drive pulse shape, increasing the intensity over time to maintain a constant driving pressure.

5.4 Results

5.4.1 VISAR data

Figure 5.7 shows an example of the VISAR results obtained using a target with a half-aluminized rear surface. At t_1 the shock enters the diamond layer, changing the reflecting surface from the first Al layer to the rear surface of the diamond. The diamond has a lower reflectivity than Al, reducing the interference effect and lowering the contrast in the fringes. The top half of the image is not changed at t_1 because the rear-surface Al is not affected. The elastic wave reaches the rear surface at t_2, accelerating the surface and causing a fringe shift. Slightly later, at t_3,

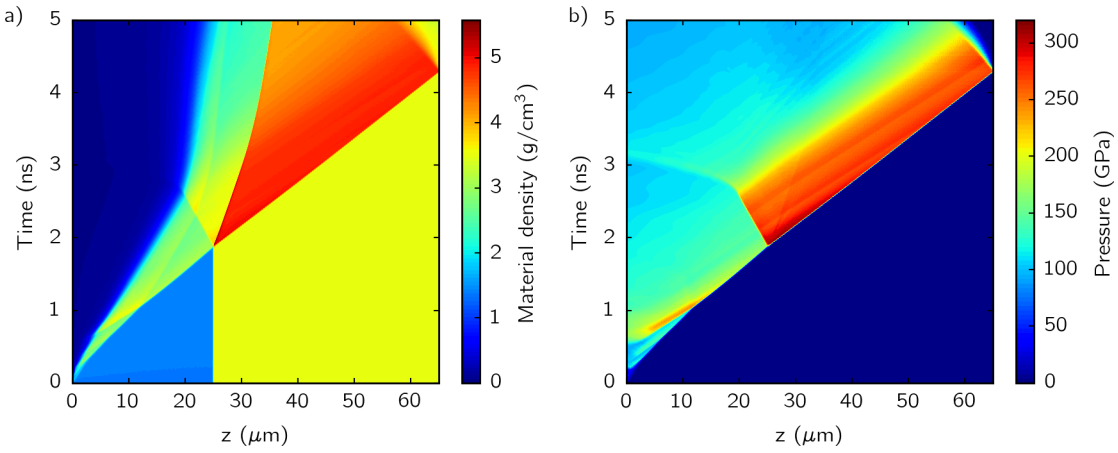

Figure 5.6: Example HYADES simulation of shock-compressed diamond with a Mylar ablator. The simulation modeled a target irradiated using the 150 μm phase plates and for the case of a 25 μm Mylar ablator and 40 μm diamond foil. The contour plots show the results for a) material density and b) pressure as a function of time.

the plastic wave reaches the rear surface, creating a release wave and destroying the reflecting surface.

After a few shots it became apparent that the half-aluminized surface was not needed to obtain a transit time measurement because the breakout time was easily measured by the change in reflectivity at t_1. We concluded that it would be more beneficial to see the full extent of the shock entering the diamond and the majority of the shots were taken with a slight offset towards the bare diamond side to remove the aluminized surface from the VISAR field of view.

Figure 5.8 shows example VISAR data and calculated free-surface velocity histories for two runs, showing a) a low-pressure run with only an elastic wave and b) a high-pressure shot with an elastic wave followed by a plastic wave. The loss of reflectivity when the shock enters the diamond causes the noise in the free-surface velocity around $t = 3$ ns for the low-pressure data and is not a real surface velocity. These data provide transit time measurements, yielding shock velocities that can be used to calculate strength as described in Section 4.5.6. Both runs shown are

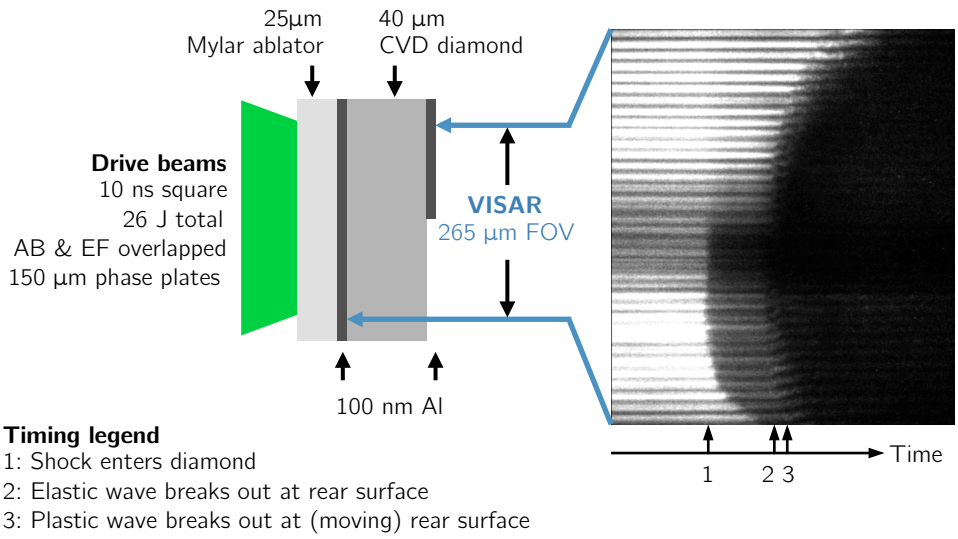

Figure 5.7: Example VISAR trace for a target with both layers of aluminum. The VISAR image shows three important times used to characterize the shock: 1) the initial loss of reflectivity on the bottom half of the image when the shock enters the diamond, 2) the loss of reflectivity in the top half when the elastic precursor reaches the rear surface, which can also be detected in the bottom half by the shift in the fringes, and 3) a second shift in the fringes on the bottom half when the plastic wave overtakes the elastic wave.

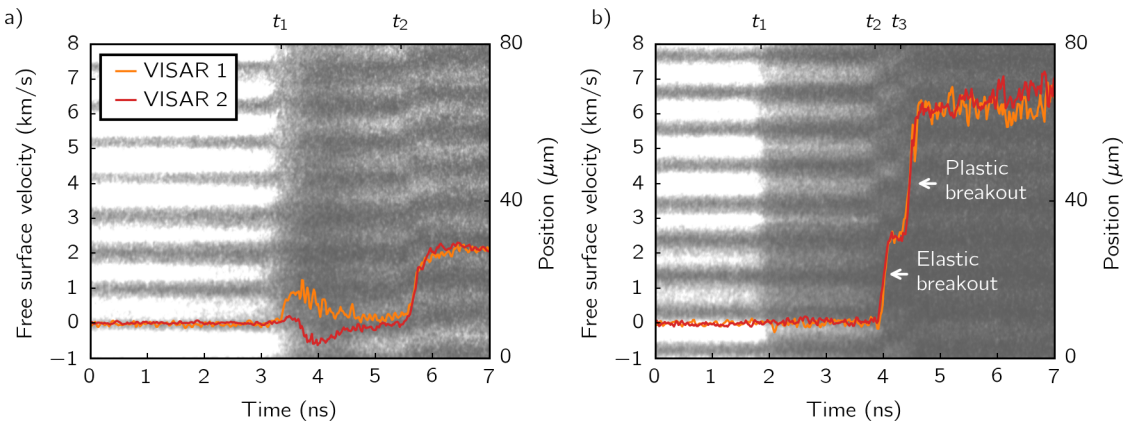

Figure 5.8: Example VISAR data and calculated free-surface velocities for runs with drive pressures a) below and b) above the HEL. The breakout times are labeled on the top of each figure, where t_1 corresponds to the shock entering the diamond, t_2 is the elastic wave breakout time, and t_3 is the plastic wave breakout time. When the drive pressure is below the HEL only the elastic wave is present. Above the HEL, crystal failure creates a plastic wave that propagates behind the elastic wave, creating a two wave structure. VISAR analysis by Emma McBride.

for targets with 25 μm Mylar ablators and 40 μm diamond foils. As expected, the transit time of the shock through the Mylar ablator is longer for the lower drive pressure while the elastic transit time through the diamond layers is nearly identical (the elastic wave velocity should be independent of drive pressure). These results show that the conditions of shock-compressed diamond were probed above and below the HEL.

5.5 X-ray scattering results

Figure 5.9 shows example x-ray diffraction data recorded by the CSPADs, plotted in 2θ-ϕ space. The initial analysis of the data is done in the Voigt limit, which is shown to be a good approximation by the fitting in Figure 4.6 for uniaxially compressed diamond. Voigt limit calculations followed the method presented by Higginbotham and McGonegle [56]. The data were fit by varying the strains in the shock

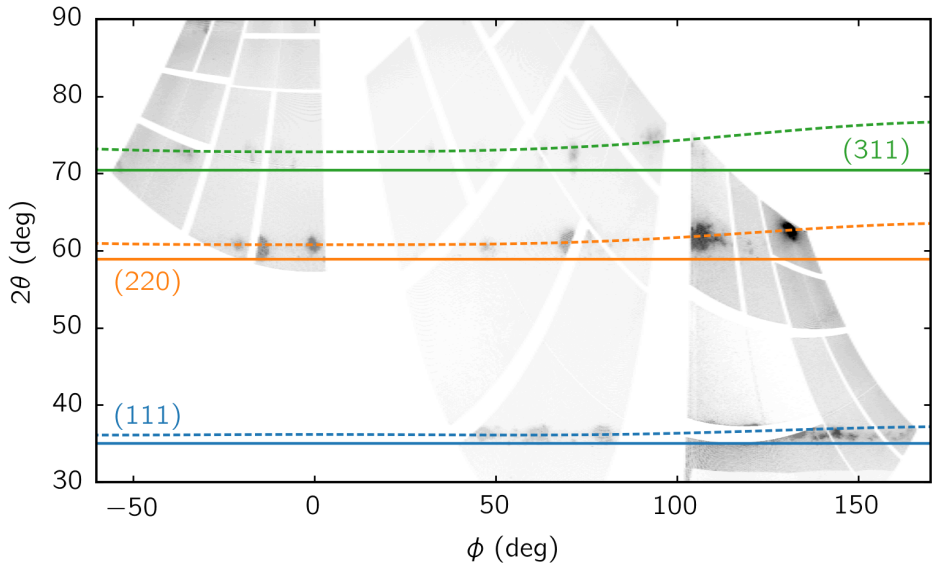

Figure 5.9: Example x-ray diffraction data, showing shock-compressed diamond with fitting curves plotted in the Voigt limit. The solid curves correspond to the diffraction angles of uncompressed diamond and the dashed curves are calculated for a compressed lattice in the Voigt limit. The strains in the shock and transverse directions used in these calculations are 0.078 and 0.028, respectively.

and transverse directions and minimizing the error in the fit for each diffraction line using least squares analysis. The diffraction angles for uncompressed (solid) diamond and a compressed (dashed) cell in the Voigt limit with strains in the shock and transverse directions of $\epsilon_{zz} = 0.078$ and $\epsilon_{xx} = 0.028$, respectively, are plotted. The compression of the sample with these strains is given by

$$\frac{\rho}{\rho_0} = \frac{1}{(1-\epsilon_{zz})(1-\epsilon_{xx})^2} = 1.15. \tag{5.1}$$

The density of the compressed diamond is 4.03 g/cm^3, corresponding a hydrostatic pressure of 84 GPa using the DFT calculations in Section 4.5.3. From the same calculations, the elastic constants for diamond at this hydrostatic pressure are $C_{11} = 1340$ GPa, $C_{12} = 262$ GPa, and $C_{44} = 801$ GPa. To estimate the deviatoric strain we work with engineering strain and write the hydrostatic and deviatoric

strains as

$$\begin{pmatrix} \epsilon_{xx} & 0 & 0 \\ 0 & \epsilon_{xx} & 0 \\ 0 & 0 & \epsilon_{zz} \end{pmatrix} = \begin{pmatrix} \epsilon_h & 0 & 0 \\ 0 & \epsilon_h & 0 \\ 0 & 0 & \epsilon_h \end{pmatrix} + \begin{pmatrix} -\epsilon_d/3 & 0 & 0 \\ 0 & -\epsilon_d/3 & 0 \\ 0 & 0 & 2\epsilon_d/3 \end{pmatrix}, \tag{5.2}$$

from which one finds

$$\epsilon_h = (\epsilon_{zz} + 2\epsilon_{xx})/3 \tag{5.3}$$

$$\epsilon_d = \epsilon_{zz} - \epsilon_{xx}. \tag{5.4}$$

Next, we calculate the deviarotic stress using $\sigma_{\mathbf{d}} = \mathbf{C}\epsilon_{\mathbf{d}}$, where the deviatoric stresses are given by $\sigma_{zz} = 2t/3$ and $\sigma_{xx} = -t/3$. These equations lead to an expression for the yield strength

$$\sigma_Y = t = (C_{11} - C_{12})(\epsilon_{zz} - \epsilon_{xx}). \tag{5.5}$$

Plugging in the values from the fit gives a yield strength of $\sigma_Y = 54$ GPa and a stress in the shock direction of $\sigma_z = 120$ GPa, which compares well with previous results [61]. These values are quoted without uncertainties and are presented only to demonstrate the application of the analysis described in the preceding chapters.

A more rigorous fitting procedure will be used to improve the results and quantify the error of the x-ray diffraction measurements. Eq. (5.5) does not depend on C_{44} as a consequence of working in the Voigt limit, which assumes elastic isotropy where $C_{44} = (C_{11} - C_{12})/2$, or equivalently, $A = 1$. The diffraction data will be fit in the Reuss limit to account for the effects of elastic anisotropy and compared to Voigt limit calculations to compare the models. X-ray diffraction data will be used in conjunction with the VISAR data to constrain the stress state of the compressed

diamond.

5.6 Conclusion

This chapter presented the design and initial results from an experiment to measure the strength of shock-compressed diamond near the HEL. This chapter discussed design considerations, including drive conditions and target design, and presented initial results from x-ray diffraction and VISAR. Measurements were made for driving pressures above and below the HEL. Careful analysis will be required to obtain high-precision measurements of the strength of diamond near the HEL. These results will shed light on the dominant failure mechanisms in diamond and can be used to improve predictive capabilities of simulation codes used to model ICF implosions with diamond ablators.

CHAPTER VI

X-ray fluorescence measurements of shock-compressed foams

6.1 Introduction

This chapter presents experiments demonstrating the use of XRF to measure ion density profiles, ionization state populations, and electron temperatures in shocked aerogel foams, conducted at the Trident laser facility. A paper on these experiments has been published in the Review of Scientific Instruments [52] and a detailed paper describing the spectral analysis of K-α fluorescence has been accepted for publication in the Journal of Applied Physics [73].

Low-density foams are attractive materials for scaled laboratory astrophysics experiments [74] because they can be produced in a wide range of densities. EOS measurements of shocked foams have been made using shock timing experiments [75–77], x-ray absorption spectroscopy [78], spectrally resolved x-ray scattering [51], velocity interferometry [79, 80], and streaked optical pyrometry [80].

XRF [81] is capable of measuring material properties in a wide range of conditions, ranging from chemical properties at ambient conditions [28] to experiments at HED. In the context of HED experiments, imaging of XRF was first proposed to diagnose hydrodynamic experiments at large-scale laser facilities [82]. It was sub-

sequently demonstrated using a pinhole imaging system [83], and more recently to infer fast-electron transport in fast-ignition targets [84]. Spectral analysis of XRF has been used to measure radiative heating [85] and infer temperatures of metals directly irradiated by high-intensity short-pulse lasers [86–90]. The experiments presented in this chapter combine these useful aspects of XRF to simultaneously measure ion density, ionization state distributions, and electron temperatures in shocked foams.

XRF has several properties that make it a useful measurement technique for HED systems. First, XRF measurements provide significantly higher signal levels than x-ray scattering measurements, as photoelectric absorption dominates x-ray interaction cross sections in the few to tens of keV energy range, as explained in Section 2.3.1. Next, XRF involves two photon energies: the probe x-ray energy used to produce electron vacancies and the resulting XRF energy. The probe x-ray energy is chosen to be above an atomic absorption edge and is readily absorbed by the target material. Meanwhile, the XRF energy is below the absorption edge and easily escapes the target. For example, the mean free paths of the V He-α probe and Ti K-α XRF x-rays (at 5.2 and 4.5 keV, respectively) in the uncompressed foam used in this experiment are 7.7 mm and 20.8 mm, respectively.

Furthermore, XRF spectra are not sensitive to small variations in the probe spectrum, provided the x-ray energy is above the absorption edge of interest. Unlike x-ray Thomson scattering [29], which interprets energy shifts in inelastic x-ray scattering, XRF spectra depend only on the energy of atomic transitions. Thus, the bandwidth and energy of the probe x-rays affect the absorption of the probe, but not the XRF spectrum. This property of XRF allows for a wider range of probe sources to be used and does not require x-ray sources with narrow spectral bandwidths.

Despite its useful properties, XRF has two significant requirements that must

be met for it to be used as a diagnostic technique in HED experiments. First, the material must contain a sufficient quantity of the element producing XRF, which may require doping the material with a suitable tracer element. The conditions inferred from XRF measurements will correspond to the tracer element, which may not be in equilibrium with the bulk material. Second, inferring temperature from XRF requires the tracer element to be partially ionized. At low ionization states the shift in the XRF energies will be negligible and at very high ionization states He-like and H-like emission will dominate the XRF spectrum.

6.2 X-ray fluorescence imaging

X-ray radiography is the standard diagnostic to image hydrodynamic experiments at HED. Radiography is best suited to diagnose experiments in simple geometries, where the structures are either two-dimensional or the three-dimensional structure can be reconstructed from path-integrated measurements. For geometrically complex targets, hydrodynamic structures are obscured by path-integrated measurements, limiting the usefulness of radiography. Imaging complex geometries with high spatial resolution requires a technique capable of measuring local conditions.

One method to probe internal structure is to use a technique that only produces signal from a specific region within the target. For example, if a target is probed with a sheet of x-rays, the resulting scattering or emission from the exposed layer can be imaged without three-dimensional effects degrading the resolution of the measurement. Figure 6.1 shows this concept for the case of a hemispherical target. X-ray radiography integrates the density along the line-of-sight through the target, while a technique utilizing a sheet of x-rays will only produce signal from a layer of the target. In this case, the probe x-rays produce XRF, which is imaged perpendicular to the exposed layer.

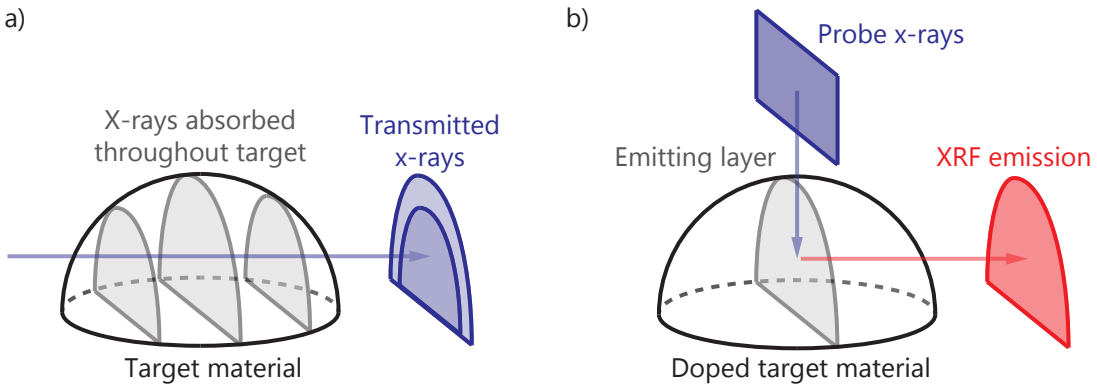

Figure 6.1: Comparison of a a) path-integrated measurement and b) a measurement from a specific region within a target. In this case, a hemispherical target is probed with a transmission diagnostic, such as x-ray radiography, and XRF imaging. XRF emission from a thin layer exposed to a sheet probe x-rays and imaged normal to the sheet to optimize spatial resolution.

Suter *et al.* [82] previously explored two methods to produce XRF from a localized region within a target: doping the target uniformly and collimating the probe x-ray source or confining the tracer material to the desired region of the target and irradiating the entire target with a probe x-ray source. Both methods are essentially equivalent, but we chose the former option for these experiments because the localization of dopant within the target material is more challenging than collimating an x-ray source. Additionally, interfaces created by doping a specific region of a target can affect the hydrodynamic evolution of the system.

6.3 Expected signal levels

The XRF signal from a volume element within a target can be estimated by accounting for x-ray attenuation and the experimental geometry. The number of detected XRF photons, γ_{det}, from a volume element with length dx is given by

$$\gamma_{det} = N_p e^{-\alpha_p x_p} \left(1 - e^{-\alpha_{p,pe} dx}\right) f_{K\alpha} e^{-\alpha_f x_f} \eta_{sys}, \tag{6.1}$$

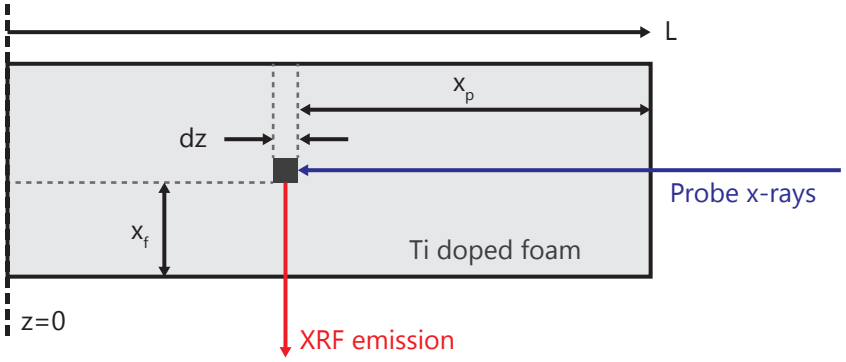

Figure 6.2: Diagram showing the dimensions used to calculate the signal levels for XRF. Probe x-rays enter the target from the right and are absorbed by the Ti-doped foam over a length x_p. The photoelectric absorption in the volume element dx creates K-shell vacancies, resulting in XRF emission. The XRF emission travels a distance x_f through the foam along the path to the detector.

where N_p is the number of probe x-rays produced, $e^{-\alpha x}$ is the absorption of x-rays by the target material with attenuation coefficient α over distance x, where the subscripts p and f refer to the probe and fluorescence x-rays respectively, $f_{K\alpha}$ is the fraction of excited atoms decaying via K-α fluorescence, and η_{sys} is a factor to account for the geometry of the system and various losses in the system. Figure 6.2 shows the dimensions used in this calculation for the simple case of a shock tube.

It is important that the photoelectric absorption term, $1 - e^{-\alpha_{p,pe} dx}$, only uses the photoelectric absorption attenuation coefficient and the density of the tracer element, while the other absorption terms account for all absorption and scattering mechanisms for all elements in the target. We estimate the number of probe x-ray photons, N_p, with energy E_γ produced by a laser-irradiated backlighter using

$$N_p = \left(\frac{E_L}{E_\gamma}\right) \eta_\gamma. \tag{6.2}$$

where E_L is the energy of laser and η_γ is the conversion efficiency of the source. The system loss parameter, η_{sys}, accounts for the fraction of probe x-rays reaching the volume element (ignoring absorption), the collection efficiency of the detector,

and any losses due to filtering

$$\eta_{sys} = \left(\frac{\Omega_{elem}}{4\pi}\right)\left(\frac{\Omega_{det}}{4\pi}\right) t_f, \tag{6.3}$$

where Ω_{elem} is the solid angle of the volume element as seen by the probe source, Ω_{det} is the solid angle of the detector as seen from the element, and t_f is the transmission of all filters in the system. The probability of radiative decay for each element is tabulated in the literature [1]. For Ti with a K-shell vacancy the probability of K-α emission is 0.17.

6.3.1 Pump-dopant pair selection

Optimizing the XRF signal requires careful selection of the tracer element and probe x-ray energy. Lower-Z backlighters provide more probe photons at the cost of a reduced mean free path within the target. As a result, the density and spatial extent of the target set a lower bound on the probe x-ray energy. The mean free path of the pump x-rays is calculated using the mass absorption coefficient for the bulk material, tabulated in the XCOM database [91], and the target density. The mean free path is given by

$$\bar{l}_p = \frac{1}{\mu_p \rho}, \tag{6.4}$$

where μ_p is the mass attenuation coefficient at the energy of the probe x-rays and ρ is material density. The probe x-ray energy should be chosen such that the mean free path is large compared to the spatial extent of the region to be probed to prevent significant attenuation of the probe. The tracer element should be the highest-Z material with the K-edge below the probe x-ray energy to maximize photoabsorption of the probe and thus require the lowest density of dopant in the target material. As shown in Figure 2.3, the binding energy of K-shell electrons increases with ion-

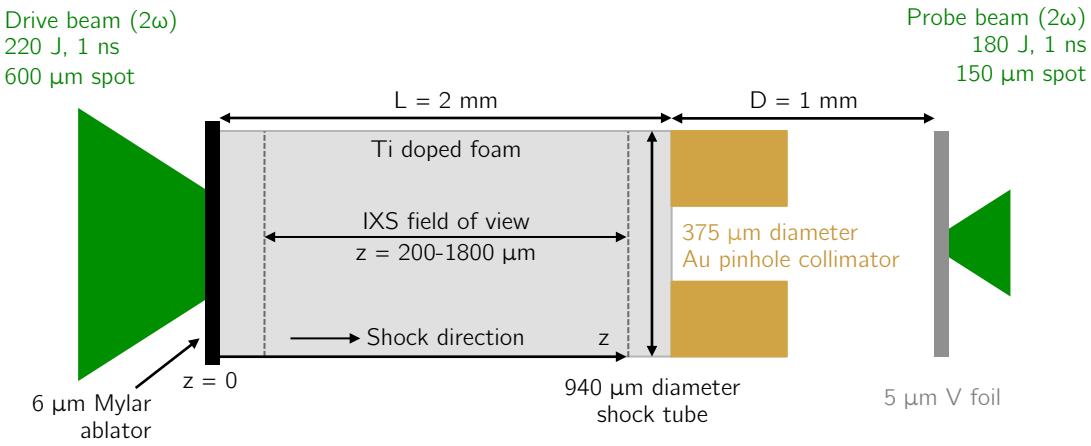

Figure 6.3: Schematic of the targets used in this experiment. The drive beam irradiated a Mylar ablator to drive a shock in the Ti aerogel foam. The probe beam irradiated a V foil to produce He-α x-rays at 5.2 keV. A gold pinhole collimator with a diameter of 375 μm restricted the volume of the target exposed to probe x-rays for a limited number of shots. The IXS provided spatially resolved spectral measurements of Ti K-α emission along the axis of the shock tube.

ization state, requiring higher probe energies for ionized materials.

This study measured Ti K-α emission using a V He-α source to create K-shell vacancies in Ti. The V He-α x-ray energy is 5.2 keV is and K-shell binding energy for unionized Ti is 4.966 keV. The K-α doublet energies for unionized Ti are 4.505 and 4.511 keV. In this analysis, we assume that the mass attenuation coefficients for photoelectric absorption are unaffected by the conditions in the shocked foam. This is justified because the bound K and L shell electrons in the Ti and Si atoms dominate the photoelectric absorption cross section for 4.5–5.2 keV.

6.4 Experimental setup

In this experiment, shown schematically in Figure 6.3, a 1 ns, 220 J beam at 2ω (527 nm) from the Trident laser system drove a shock in a cylindrical foam target, compressing and heating the foam. The laser was focused, using a random phase

plate (RPP), to a 600 μm spot on a 6-μm-thick Mylar ablator on the drive side of the target. The ablator prevented direct irradiation of the low-density foam. The foam targets were 2000 μm in length and 940 μm in diameter, inside a polyimide tube with a 53 μm wall thickness.

A 1 ns, 180 J, 527 nm laser beam focused to 150 μm using a RPP irradiated a 5 μm V foil 1.0 mm from the foam on the side opposite of the drive in order to produce a bright He-α x-ray source. A small number of targets included a gold collimator with a 375 μm diameter pinhole placed between the foam and the V foil to restrict the region exposed to the probe x-rays.

6.5 Target design

6.5.1 Ti-doped foams

Two types of foams were used in these experiments: 3.4 mg/cm^3 Ti-doped aerogel foams and 195 mg/cm^3 Ti-doped CRF foams. The low material density and relatively high fraction of Ti in these foams produced bright XRF emission when exposed to probe x-rays. All results presented in this chapter are from the aerogel foams with the exception of the spatial profiles showing the effect of the collimator.

The Ti-doped aerogel foams consisted of a 1.0 mg/cm^3 SiO_2 scaffolding coated with 2.4 mg/cm^3 of TiO_2 for a total density of 3.4 mg/cm^3. The detailed characterization of these the aerogel foams can be found in a separate publication [92], where this experiment used foams coated using 30 atomic layer deposition cycles. Because the Ti is uniformly distributed on the scale of the spatial resolution of the detector, the XRF intensity directly correlates to material density. The low density of the aerogel foams enabled temperatures in the postshock material to be high enough to observe shifts in the Ti K-α emission from the ionized material. Rutherford Backscattering Spectrometry (RBS) measurements provided the relative atomic

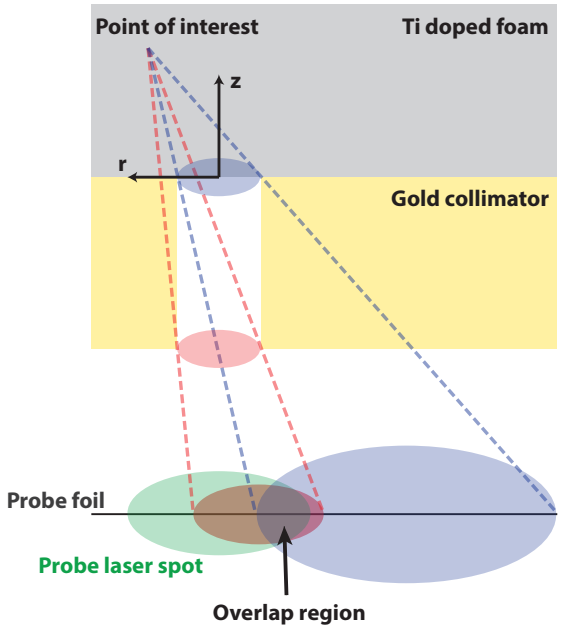

Figure 6.4: The probe intensity reaching a point in the foam target is proportional to the area of the probe foil with direct line-of-sight to the point. This area is equal to the overlap of the projected collimator apertures and the laser focal spot on the foil.

fractions of $TiO_2/SiO_2 = 1.8$ in the aerogel foams, corresponding to a mass ratio of 2.4. The Ti-doped CRF foams were composed of 190 mg/cm^3 CRF with 5 mg/cm^3 Ti dispersed throughout the material.

6.5.2 Collimator

A 375 μm diameter pinhole collimator restricted the region of the foam irradiated by the probe for a limited number of shots to demonstrate the ability to selectively probe the tube axis. The probe intensity is proportional to the area of the probe laser spot on the V foil with direct line-of-sight to each point in the foam. For an arbitrary point in the foam, this area is calculated by projecting the aperture on each side of the collimator onto the foil plane and calculating the overlap area, A_{ovl}, of the projection both apertures and the laser spot, as shown in Figure 6.4.

The pump intensity at each point in the foam, neglecting absorption, is given by

$$\frac{I_{pump}(r,z)}{I_0} = \frac{R_s^2}{R_s^2 + (L + D - z)^2} \left(\frac{A_{ovl}}{\pi R_s^2} \right) \tag{6.5}$$

where I_0 is the intensity of the probe emission, R_s is the radius of the probe emission area, defined by the laser spot on the foil, and Figure 6.3 defines the other dimensions. The first term in Eq. (6.5) assumes a Lambertian emission profile from the probe x-ray source and is only strictly valid on axis, but is sufficient to estimate the intensity in this case. Figure 6.5 shows calculated probe intensities at each point in the foam for a 375 μm diameter pinhole collimator and for no collimator. Below each contour plot is a lineout showing the total probe flux through the tube along the axis, calculated by performing a radial integral of the intensity. As expected, the probe intensity is constant for most of the shock tube with the collimator, while it quickly decays with no collimator.

6.6 Imaging x-ray spectrometer

The primary diagnostic on the experiment was an imaging x-ray spectrometer (IXS) [93], which measured spatially resolved spectra along the axis of the shock tube. This diagnostic used a toroidally bent Ge(400) crystal with radii of curvature of 400 and 200 mm in the spectral and imaging directions, respectively. The crystal was placed 139.9 mm from target chamber center. X-rays were detected using Fuji BAS-SR image plate located 388.8 mm from the crystal, satisfying the imaging condition for the crystal optic with a magnification of 2.78 centered at the Ti K-α energy of 4.5 keV.

The spectral dispersion of the IXS was calibrated using the Ti K-α doublet and the spectral resolution of 2.1 eV was calculated by fitting a Voigt profile to the Ti K-α doublet produced by unshocked material. Transmission of line emission from laser-irradiated Sc foils through Au grids with 35 μm bar thickness and 125 μm

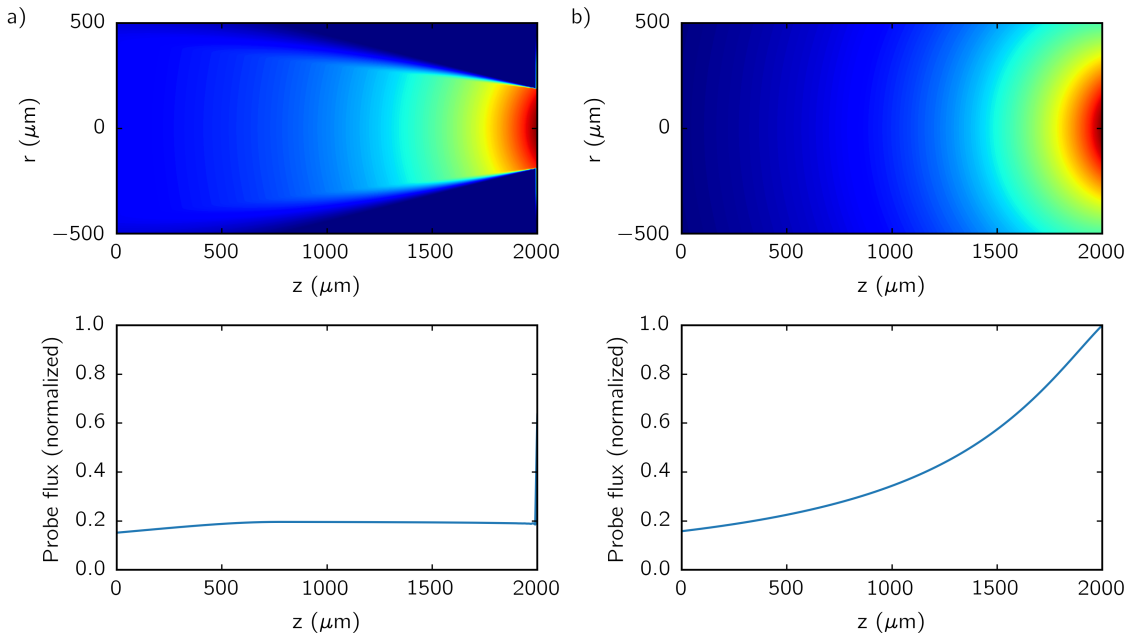

Figure 6.5: Calculations showing the probe intensity for each point in the shock tube for a probe x-ray source created by a 150 μ spot at $z = 3000$ μm for the cases of a) a 375 μm pinhole collimator and b) no collimator. Below each contour plot is a lineout of the integrated probe flux through the shock tube along the axis. The collimated has a constant flux for much of the length of the tube, while the flux with no collimator quickly decays as the probe radiation escapes out the walls of the tube.

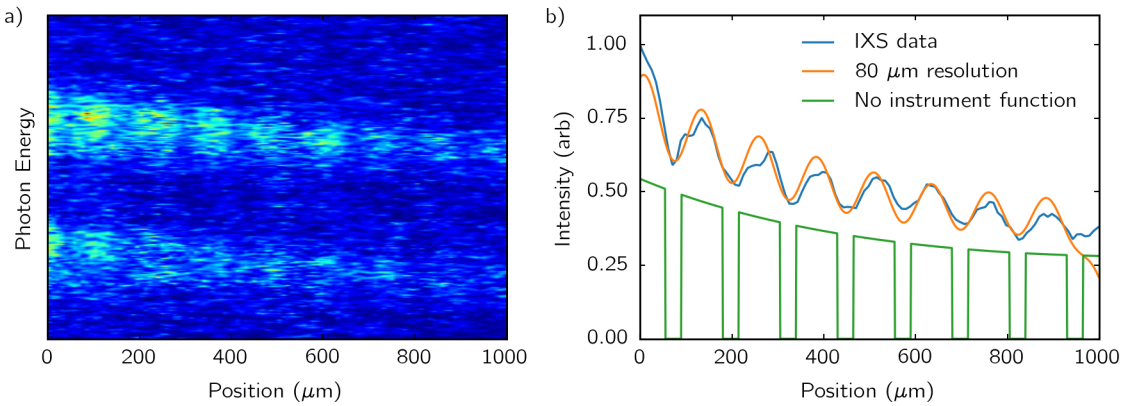

Figure 6.6: a) Raw IXS data for an Au grid with 35 μm bar thickness and 125 μm pitch backlit by emission from a laser-irradiated Sc foil and b) a calibrated spatial lineout of the IXS data with a fit for an ideal grid with 80 μm spatial resolution. The transmission of an ideal grid was convolved with a Gaussian instrument function with a FWHM of 80 μm to produce the fit.

pitch determined the spatial resolution. Spatial profiles measured using these grids were fit using a Gaussian instrument function to determine the spatial resolution of 80 μm. Figure 6.6 shows raw IXS data for the backlit Sc foil and the fit to the transmission of the grid used to define the instrument function of the IXS.

6.7 Simulations

HYADES [94], a Lagrangian radiation hydrodynamic model with laser absorption and electron heat conduction, simulated the experimental conditions for each target design. The simulations helped guide the experimental design and were used to set the probe delays for the initial shots. The simulations also provided an estimation of the decay of the shock velocity over time to account for temporal smearing over the 1 ns duration of the probe. After tuning Hyades to match the measured shock location at 15 ns, the simulated velocity at that time is 60 μm/ns. On this basis, we estimate the motion blurring in 1 ns at a time of 15 ns to be 60 μm. This effect was included in the modeling of the spatial information by integrating the

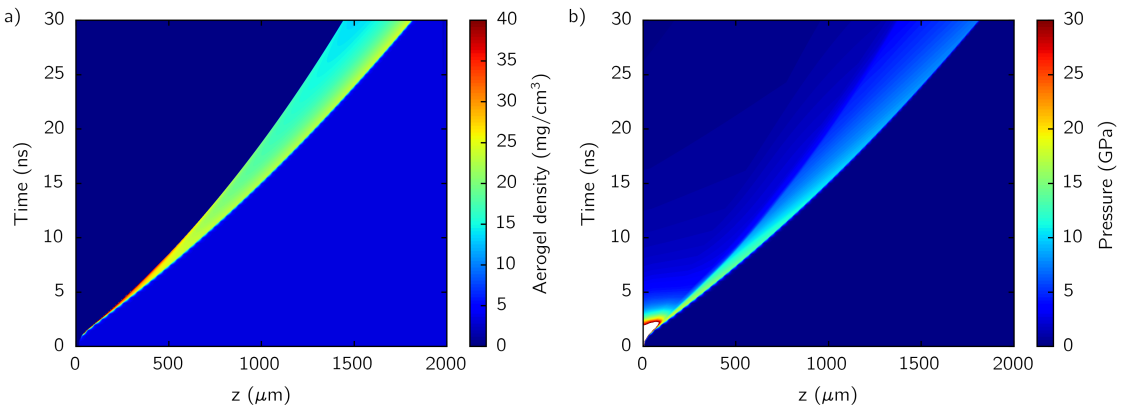

Figure 6.7: HYADES results for Ti-doped aerogel foam after tuning the drive intensity to match the measured shock position at $t = 15$ ns, showing a) material density and b) pressure as a function of time. From these calculations the shock velocity was estimated to be 60 μm/ns at $t = 15$ ns.

shock profiles with 1 μm steps. The total signal was then normalized to the intensity of the unshocked region. Figure 6.7 shows the simulated a) material density and b) pressure for the aerogel target.

6.8 Experimental results

The IXS provided simultaneous density and K-α emission measurements of the shocked foam. Figure 6.8 shows an overview of the XRF data obtained from a single measurement.

6.8.1 Unshocked region

The initial density of the foam was measured using the spatial data from the IXS in the unshocked region from z = 1200–1700 μm, as illustrated in the inset of Figure 6.6. For the targets without a collimator, fits to the unshocked data determined ρ_0. The calculated XRF signal as a function of z is given by

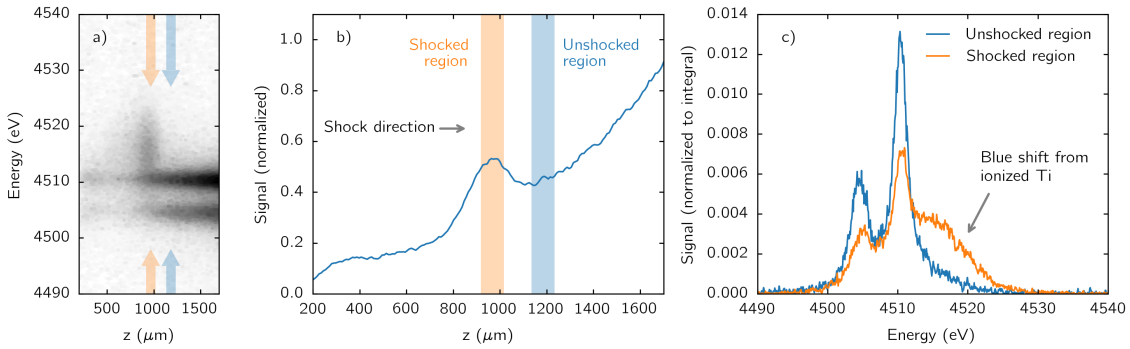

Figure 6.8: a) Raw image plate data from the IXS showing the shifted spectrum at the shock interface, b) the spatial lineout summing over spectral components at t = 15 ns, and c) the spectral data for the two regions highlighted in the spatial lineout showing the shifted K-α fluorescence in the shocked foam as compared to the Ti in the unshocked foam.

$$\frac{I}{I_0} = \exp\left[-\mu\rho_0(L-z)\right]\left(\frac{R_s^2}{R_s^2+(L+D-z)^2}\right), \tag{6.6}$$

The first term accounts for attenuation of the probe x-rays by the foam and the second term accounts for the distance from the probe source. Once again, this formula is strictly valid only on the axis of the shock tube, but the experimental geometry makes this a reasonable approximation.

At the probe energy of 5.2 keV the total mass attenuation coefficient of the foam is μ_p = 322.0 cm^2/g. The density of the unshocked foam was found to be $\rho_0 = 4.1 \pm 1.5$ mg/cm^3, where the error bars represent the maximum deviations from the best fit deemed plausible by the authors, as shown in Figure 6.9. Knowing the mass ratio of the TiO_2 and SiO_2 from RBS measurements, we conclude that the foam used in this experiment consisted of 1.2 $\pm$ 0.4 mg/cm^3 SiO_2 and 2.9 $\pm$ 1.1 mg/cm^3 TiO_2. The density calculated using this technique agrees with the density measured during foam production of 3.4 mg/cm^3 within error.

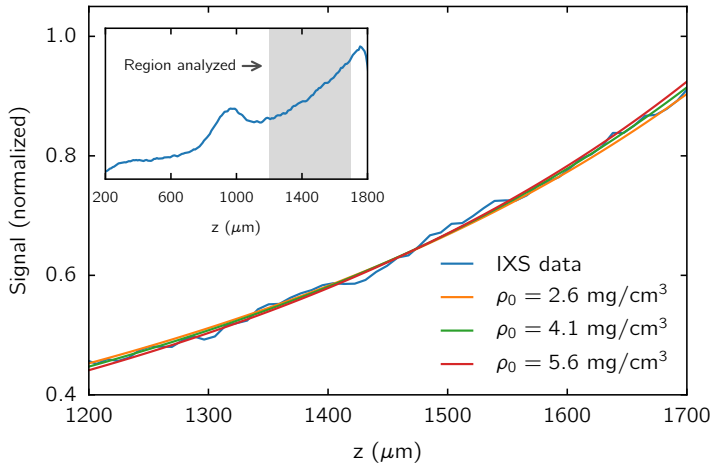

Figure 6.9: Results of fitting Eq. 6.6 to the unshocked region of the spatially resolved data (illustrated in the inset), yielding an initial foam density of $\rho_0 = 4.1 \pm 1.5$ mg/cm^3.

6.8.2 Driven foams

The IXS provides an integrated measurement of all material in a spatial element (dz) along the axis of the shock tube. The shock profile produced by the 600 μm drive beam was expected to be curved and only approximate a planar shock near the axis of the tube, with the width of the planar region decreasing as the shock propagates. To account for this effect, the XRF signal was calculated using a simple two-region model, consisting of a shocked inner region and an unshocked outer region. We assume a strong shock profile with no release for the shocked aerogel foam. This model was used because the mass of the 6-μm-thick ablator was greater than the total mass of the shocked aerogel at the time it was probed. This suggests that the ablator density was still greater than the shocked aerogel density and acted as a piston compressing the foam.

The inset of Figure 6.11 shows the contributions to the XRF signal from each of the two regions. As predicted by the piston model, only the outer, unshocked region contributes to the signal well behind the shock front ($z < 700$ μm). This feature allowed the fraction of unshocked material to be determined and it was found that

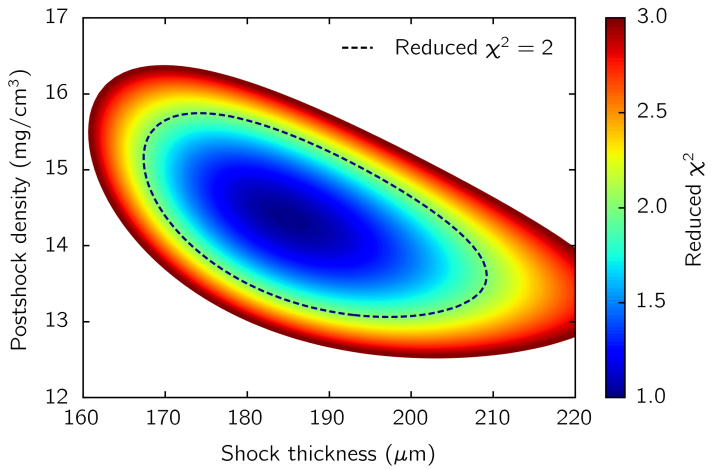

Figure 6.10: Reduced χ^2 values for a range of shock thicknesses and postshock densities for z = 850–1500 μm. The quoted uncertainty in the postshock density was calculated by requiring $\chi^2 < 2$, as shown by the dashed contour, yielding $\rho_1 = 14.4 \pm 1.3$ mg/cm^3.

74% of the signal came from the unshocked region.

The peak in the spatial data was fit by varying the width (in z) of the shocked region and postshock density. Bounds were set on the postshock material density by fitting the spatial profile in the range $z = 850 - 1500$ μm using reduced χ^2 analysis. This region was chosen to fit shock front and minimize the error from the edge effects of the curved shock front. The reduced χ^2 (χ^2_r) value for each fit was calculated using

$$\chi^2_r = \frac{1}{\nu} \sum_i \frac{(s_i - f_i)^2}{\sigma^2}, \tag{6.7}$$

where s_i and f_i are the values for the signal and fit at each measured position, σ^2 is the variance of the signal, and ν is the number of degrees of freedom in the fit. Here, we estimate the variance from signal fluctuations in the unshocked region ($z = 1250 - 1750$ μm) and assumed to be constant and the degrees of freedom is equal to the number of data points in the fit region minus the number of fit parameters (shock thickness, postshock density, and estimated variance). Figure

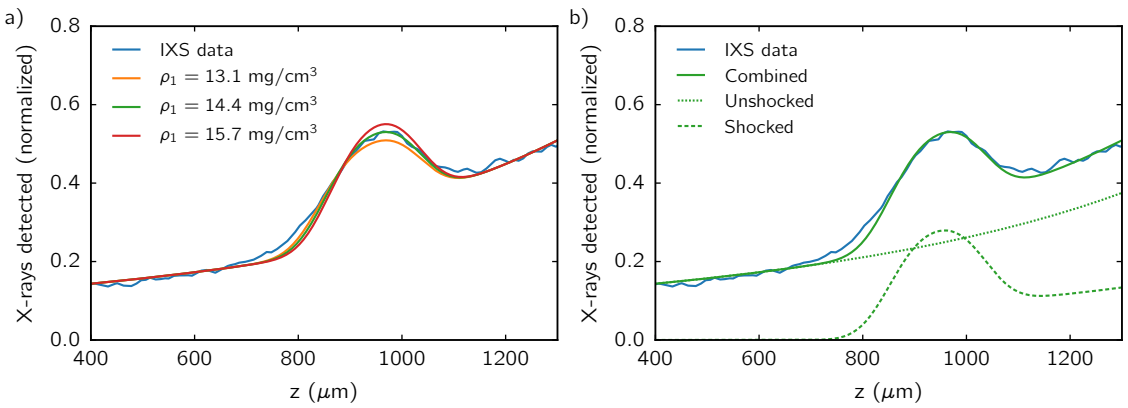

Figure 6.11: a) Fits to the spatial data at the shock location at t = 15 ns. XRF signals from strong shock density profiles with contributions from unshocked material are plotted for $\rho_1 = 14.4 \pm 1.3$ mg/cm^3. b) XRF signal contributions from the shocked and unshocked regions.

6.10 shows the value of χ_r^2 for a range of postshock densities and shock thicknesses. The global minimum corresponds to the best fit at $\rho_1 = 14.4$ mg/cm^3 and a shock thickness of 185 μm. The error bounds on the postshock density were set by plotting the contour of $\chi_r^2 = 2$, yielding $\rho_1 = 14.4 \pm 1.3$ mg/cm^3.

Figure 6.11 shows the calculated spatial signal and the measured postshock density of $\rho_1 = 14.4 \pm 1.3$ mg/cm^3. The calculated signals for the upper and lower bounds of the density with the corresponding shock thicknesses determined by the $\chi_r^2 = 2$ contour for these densities are also plotted. The slight disagreement between the fit and the IXS data in the region behind the shock is most likely a result of the simple two-region model not accounting for additional material on the edges of the curved shock front. This measurement could be significantly improved by selectively probing the planar shock region by using a collimator [51] or by probing with an x-ray FEL.

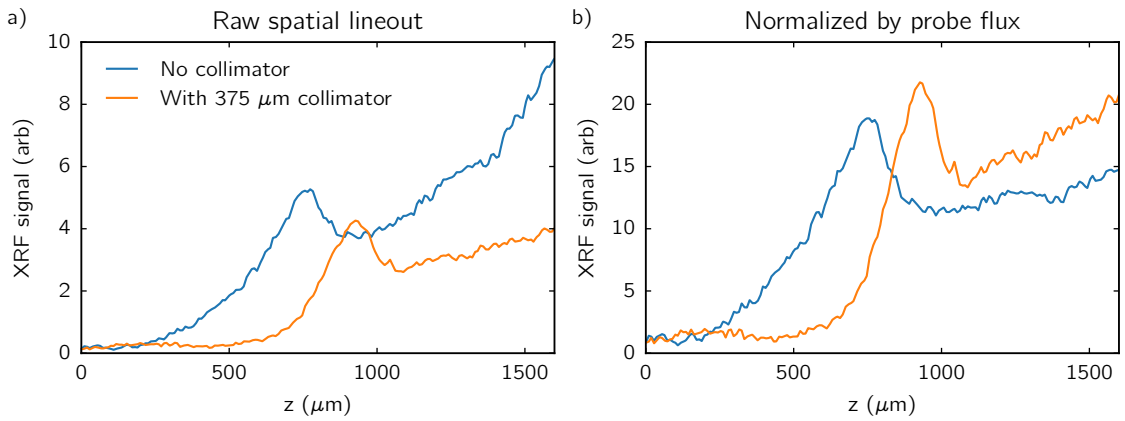

Figure 6.12: Spatial lineouts of XRF data for runs with and without a 375 μm gold collimator to restrict the region exposed to probe x-rays. a) Raw data and b) data normalized by the fluxes calculated in Figure 6.5 (only accounting for geometrical effects and not absorption) are shown. The width of the shocked layer is much narrower with the collimator because the edge effects near the walls of the shock tube do not contribute to the XRF signal.

6.8.3 Selectively probing the tube axis

Figure 6.12 shows A comparison of spatial XRF signals obtained with and without a collimator for Ti-doped CRF foam. The improvement in spatial resolution is clear when the raw spatial lineouts are normalized by the probe fluxes calculated in Section 6.5.2. The edges effects are not present in the shot with a 375 μm collimator and the shock front is much narrower. The density of the Ti-doped CRF resulted in low postshock temperatures and no shifts in the Ti K-α spectra were measured, preventing temperature measurements for targets with a collimator. These results demonstrate the ability to restrict the probed region using a collimator. For a 2D imaging diagnostic, a slit collimator can create a sheet of x-rays to image the hydrodynamic evolution of the system. This ability to selectively probe specific regions is a useful property of XRFI that may enable complex geometries to be imaged with high resolution.

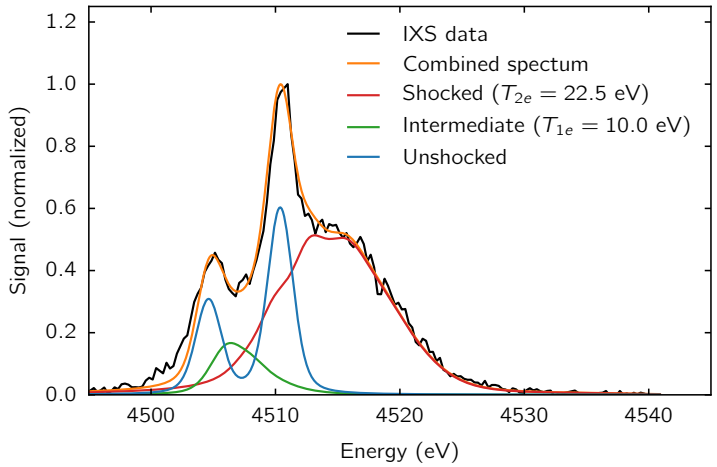

Figure 6.13: Spectral fitting results for shock heated aerogel using spectra from CRETIN [5] simulations. Contributions from three regions were used to model the curved shock produced in this experiment. Although three regions are required to accurately model the full range of the IXS spectral data, the shocked region dominates the line shape in the range of 4515–4540 eV.

6.8.4 Inferring T_e from K-α spectra

CRETIN [5] calculated the K-α spectra for the density and temperatures reached in this experiment. CRETIN is a multi-species atomic kinetics and radiation code, which provided a self-consistent model for spectral emission from the shocked region. Screened-hydrogenic atomic models [95] were used for Si and O, while more detailed atomic data for Ti were calculated using the Flexible Atomic Code (FAC) [96]. The atomic model for Ti incorporated data describing all singly and doubly excited states within each ionization state up to a maximum principal quantum number of 8, averaged over configurations while maintaining a spectral resolution of 1 eV. The detailed atomic data for Ti used in these calculates were provided by Howard Scott.

Calculations of XRF spectra were performed for a range of electron temperatures and material densities to fit the IXS spectral data in the heated region. To fit XRF spectra, we include contributions from the shocked and unshocked regions,

as well as a small component from material at an intermediate temperature to account for edge effects in the curved shock front. Properly fitting the spectra in the 4500–4510 eV range requires the addition of the intermediate component, but has a negligible effect on the spectra in the 4515–4540 eV range where the contribution from the hottest region dominates. These three regions are labeled 0, 1, and 2 for the unshocked, intermediate, and shocked regions, respectively.

Figure 6.13 shows the spectral contributions from the three regions along with the combined fit to the IXS data, where an electron temperature of $T_{1e} = 10.0$ eV in the intermediate region produced the best fit. In reality, this intermediate region consists of material at a range of temperatures, but this simple model is reasonable considering the small spectral contribution of this region.

For the conditions present in this experiment, the mean ionization state increases with decreasing density. This requires the lower and upper bounds on the electron temperature to be calculated at the lower and upper density bounds, respectively. Using this method, the post-shock electron temperature was found to be $T_{2e} = 22.5 \pm 2.5$ eV. Figure 6.14 shows the results of the spectral fitting, with the relative ionization state populations present in each condition shown in the inset.

This fit could be improved by probing a more homogeneous region in the material. The 80 μm integration region, set by the spatial resolution of the IXS, and the curved shock front result in a measurement from a range of densities and temperatures. Here we have made an attempt to account for these effects with a three-region model, but high-precision EOS measurements should probe a homogeneous region in the system.

6.9 Evaluation of postshock conditions

The state of matter reached in the postshock material is determined by calculating the Coulomb coupling parameter and the degeneracy parameter from Section

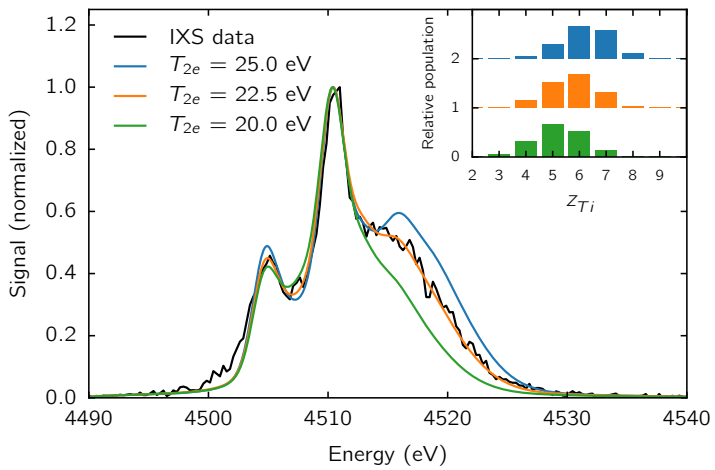

Figure 6.14: Ti K-α fluorescence from shock-heated aerogel using CRETIN [5] used to infer an electron temperature in the post-shock material of $T_{2e} = 22.5 \pm 2.5$ eV. Bounds on electron temperature were set by fitting to measurements from the IXS. The inset shows the relative ionization states of Ti present in each case. The spectra for the upper and lower electron temperature bounds were calculated at the upper and lower bounds of material densities.

1.1. These parameters are functions of free electron density and temperature, which are calculated from the IXS measurements and CRETIN simulations. The free electron density is $n_e = 1.5 \times 10^{21}$ cm^{-3} and the temperature is $T = 22.5$ eV, where it is assumed that the electrons and ions are in thermodynamic equilibrium. These values give

$$\Gamma_{ee} = 0.12 \quad \text{and} \quad \Theta = 47, \tag{6.8}$$

which describe a state of matter that is weakly coupled and non-degenerate, and thus not WDM. Reaching WDM conditions in a similar experiment would require a higher free electron density and would require using tracer elements with higher XRF energies. Such experiments could be performed at the Omega laser facility or at NIF, where significantly higher laser energies are available to drive stronger shocks and produce sufficiently bright probe sources at higher x-ray energies.

6.10 Conclusion

The experiments presented in this chapter demonstrated the ability to use XRF to simultaneously measure ion density profiles, ionization-state distributions, and electron temperatures of shocked foams. Fits to spatial data from an imaging x-ray spectrometer provided measurements of the initial and post-shock foam density. Spectral data constrained the Ti ionization-state distribution and electron temperature using K-α spectra calculated with CRETIN. XRF measurements provide a high-brightness diagnostic tool for shock-compression experiments. Combined with other diagnostic techniques, XRF measurements can improve EOS models for shocked materials.

CHAPTER VII

Conclusions and future directions

This thesis described two experiments and a theoretical model to study the properties of compressed matter using time-resolved x-ray diagnostics. Each project contributes in some way to the advancement of the ICF program, whether in the form of improved EOS measurements, modeling capabilities, or diagnostics for HED conditions. Beyond the scope of ICF, the properties of materials at HED are important to other fields, including planetary interiors and astrophysical dynamics. The vastly different properties of the materials studied in these experiments — solid diamond vs. low-density aerogel foam — speaks to the versatility of x-ray diagnostics. To conclude, a brief summary of each topic presented in this thesis is provided along with possible future directions.

7.1 Modeling x-ray diffraction from shocked materials

Chapter IV described a method to model x-ray diffraction patterns from highly-stressed polycrystalline materials. The method presented is formulated in the Reuss limit, where all crystallites within a polycrystalline sample are exposed to a single stress tensor defined in the laboratory frame. Unlike the Voigt limit, where a single strain tensor is applied, the Reuss limit accounts for the effects of elastic anisotropy. Example diffraction patterns were shown to illustrate the effects of sample texture

and material strength.

The validity of the Voigt and Reuss limits remains an open question in the dynamic compression community for materials with high strength. Although the examples presented in Chapter IV do not show a significant difference between the two models for diamond, materials with more pronounced anisotropic elasticity could be investigated to compare the two models. The availability of models in both limits enables such cases to be identified. Experiments investigating these cases will improve our understanding of the stress-strain relationship at grain boundaries in polycrystalline materials under dynamic compression.

Regarding the Reuss limit, the work presented in this thesis assumed that the deviations from the hydrostatic condition are small perturbations, justifying the use of elastic coefficients. The effect of nonlinear elasticity can be included to extend the range of states this technique can accurately model.

7.2 Dynamic strength of polycrystalline diamond

Chapter V presented the design and initial results from an experiment to study the behavior polycrystalline diamond under shock compression. This chapter focused on the experimental design and discussed various considerations to consider when planning a shock-compression experiment. An example diffraction pattern and an initial fit in the Voigt limit were shown to compare the measurements to previously published data on the yield strength of diamond. Further analysis will improve the accuracy of these measurements and quantify their uncertainty. Fits in the Reuss and Voigt limits will be compared to conditions inferred from VISAR data. With strains approaching 10%, nonlinear elastic constants will likely be needed to accurately model the stresses in the shocked diamond. The results obtained from these experiments will shed light on the failure mechanisms of diamond near the Hugoniot elastic limit.

7.3 X-ray fluorescence imaging and spectroscopy

Chapter VI demonstrated a technique to measure the EOS of shock-compressed foams using XRF. The experiments conducted at the Trident laser facility required only a few hundred joules of laser energy to drive shocks into foam targets and measure the conditions using XRF with high brightness. Density profiles were obtained using an imaging spectrometer to infer the compression of the shocked material and spectral analysis combined with spectroscopic modeling provided ionization state and electron temperature data. EOS models for shocked materials can use these data to improve the predictive capabilities of codes for future HED physics experiments.

Future studies using XRF could be conducted at larger laser facilities, such as Omega or NIF, where significantly higher drive pressures can drive planar shocks creating WDM. With the additional laser energy available at these facilities, shocks with larger drive areas can be created and probed using a collimated source to remove edge effects from the measurements. Alternatively, shocks can be probed by an x-ray free electron laser to achieve the same result.

The high brightness and ability to selectively probe specific regions of a target using XRF make it a promising diagnostic for HED experiments in complex geometries. One example is the study of hydrodynamic instabilities in a diverging explosion [97]. Such an experiment could be diagnosed by exposing a thin layer of the target to probe radiation and placing the imaging diagnostic normal to the probed plane. 2D images with high signal-to-noise could be obtained by using a spherical crystal x-ray optic, such as the Cu K-α spherical crystal imaging diagnostic currently available at OMEGA [98].

APPENDIX

APPENDIX A

High-dynamic range XRTS measurements of rare gas clusters

Atomic clusters can serve as ideal model systems for exploring ultrafast ($\sim$100 fs) laser-driven ionization dynamics of dense matter on the nanometer scale. Resonant absorption of optical laser pulses enables heating to temperatures on the order of 1 keV at near solid density conditions. To date, direct probing of transient states of such nano plasmas was limited to coherent x-ray imaging. Here we present the first measurement of spectrally-resolved incoherent x-ray scattering from clusters, enabling measurements of transient temperature, densities, and ionization. Single-shot x-ray Thomson scatterings signals were recorded at 120 Hz using a crystal spectrometer in combination with a single-photon counting and energy-dispersive pnCCD. A precise pump laser collimation scheme enabled recording near background-free scattering spectra from Ar clusters with an unprecedented dynamic range of more than 3 orders of magnitude. Such measurements are important for understanding collective effects in laser-matter interactions on femtosecond timescales, opening new routes for the development of schemes for their ultrafast control.

A.1 Introduction

Atomic clusters readily absorb intense laser radiation due to their extremely large cross section [99, 100], resulting in the emission of high energy electrons [101], ions [102] and x-rays. Previous measurements of ionization dynamics in such nano plasmas relied on the analysis of final reaction products and direct probing of transient nano plasmas was limited to coherent x-ray imaging [103]. Here we present a proof-of-principle experiment using incoherent XRTS to measure electron velocity distributions in clusters, which will ultimately enable time-resolved measurements of temperature, ionization, and collective electron dynamics on $<$100 fs time scales.

The small Thomson scattering cross section ($\sigma_T = 6.65\times10^{-25}$cm^2) in combination with the low average particle density in cluster jets poses a particular challenge for XRTS measurements. Being in the single photon counting regime, efficient mitigation of background signals is required. Furthermore, mid- or high-Z elements require high-dynamic range spectra to resolve inelastic Compton scattering near the strong elastic scattering component. Here we describe the setup for the infrared (IR) laser driven experiment and present the measurement of a high-dynamic range, near background-free XRTS spectrum from Ar clusters using an energy-dispersive pnCCD detector [104] in single-photon counting mode to integrate up to 200,000 shots.

A.2 Experimental setup

The experiment was conducted using the LAMP endstation at the AMO instrument [105, 106] at the Linac Coherent Light Source (LCLS) [107]. The clusters were created using an Even-Lavie source [108] with nozzle diameter of 150 μm and opening angle of 40°, operated at room temperature with a backing pressure

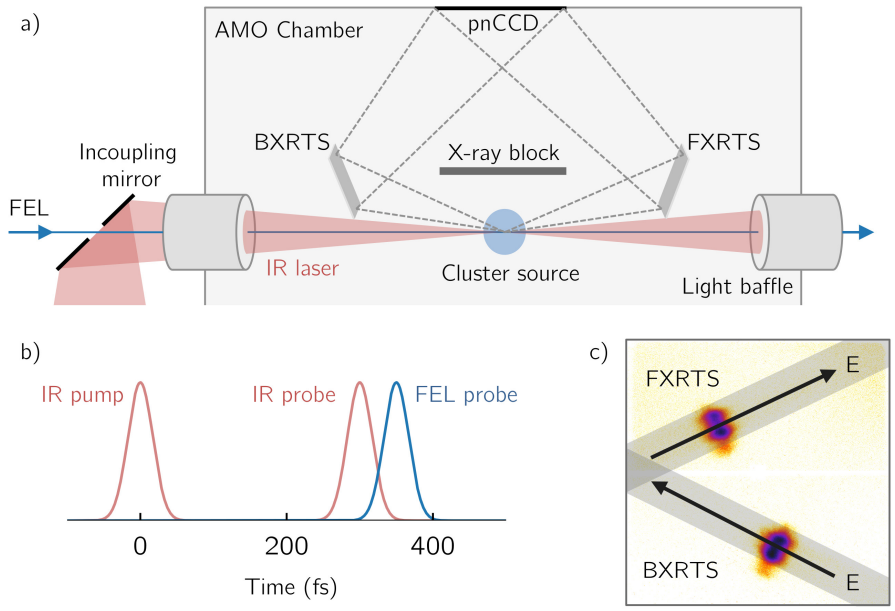

Figure A.1: a) Experimental geometry, b) pump-probe timing of IR pulses and FEL probe, and c) example raw pnCCD data showing the active regions of the detector for the forward (FXRTS) and backward (BXRTS) scattering spectra. Arrows indicate the respective energy axis of each spectra.

of 80 bar. Based on common scaling, we expect argon clusters, Ar_N, of mean size $N = 60,000$ and atomic density of $n_{at} \sim 10^{17}$ cm^{-3} in the jet at 2 mm from the nozzle.

Figure A.1 shows a schematic of the experimental setup. The gas clusters are manipulated using a pump-probe system with two 40 fs IR pulses at 800 nm from a Ti:Sapphire laser system with intensities up to 10^{15} W/cm^2. The free electron laser (FEL) was operated at 1811 eV to measure XRTS spectra from Ar. An incoupling mirror with a central hole for the FEL probe to pass through was used to make the IR and FEL beams colinear, interacting with the clusters 2 mm from the nozzle where the diameter of the cluster jet was $\sim$1 mm. The relative delay between the pump and probe IR pulses was set using a mechanical delay stage and the IR-FEL timing was measured for each shot using a spectrally-encoded time tool system [109].

Two cylindrically curved PET (002) crystal spectrometers measured XRTS of the FEL probe in forward (FXRTS) and backward (BXRTS) scattering geometries

at scattering angles of 28° and 152°, respectively. The details of the spectrometer design, setup, and characterization are described in detail in a separate publication [110].

Single photon counting was enabled by the low noise pnCCD detector [104]. Two layers of aluminized polyimide film (700 nm polyimide + 100 nm Al each) were used to stop optical light and an x-ray block was in the direct line-of-sight between pnCCD and interaction region. Background was further reduced by the use of light baffles to limit diffuse IR reflections within the chamber.

A.3 Removal of IR laser background

Figure A.2 shows a histogram of detected pixel intensity values, measured in analog digital units (ADU), normalized by the number of shots for each run. Three runs are presented to show the contribution of each source: a dark run, an IR only run, and an IR + FEL run, containing 8,280, 12,067, and 190,784 shots, respectively. The histogram shows that the IR laser contributes the vast majority of the signal, $\sim$0.1 IR photons/pixel/shot, but this contribution can be easily removed by setting a minimum threshold above $\sim$500 ADU. The scattered x-ray peak is located above 1800 ADU, where a minimum threshold is set to remove additional background as shown in the inset, where the counts per shot are shown on a linear scale. A small peak appears near 1750 ADU, which is most likely Al K-α fluorescence at 1486 eV from the pnCCD filtering or other Al components in the chamber. In addition to the XRTS measurements made by the pnCCD, the slope of the histogram data can be used to infer a temperature for the hot plasma.

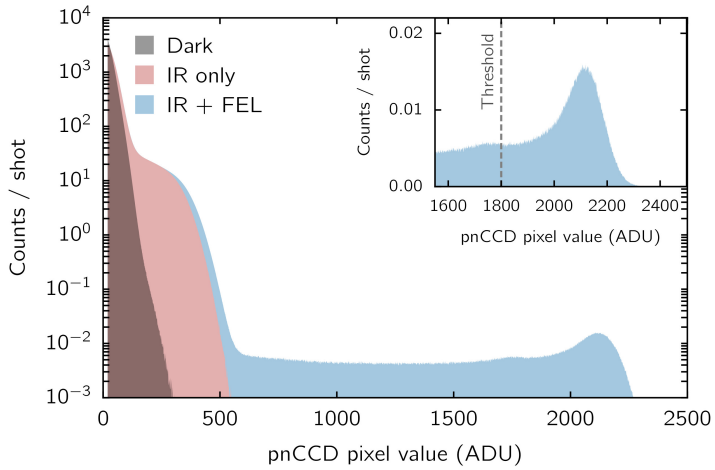

Figure A.2: Histogram of pnCCD ADU values for a dark run, an IR only run, and an IR + FEL run to show the contributions from each source. Counts from scattered x-rays are shown in the inset with the threshold used to remove background.

A.4 FEL energy jitter correction

The FEL at LCLS has an RMS photon energy jitter of $\sim 0.1\%$ at 1.8 keV. These variations reduce the spectral resolution of scattering measurements when integrating over many shots by convoluting the output spectrum with this distribution. This broadening can be avoided by measuring the centroid of the input spectrum for each shot.

To make this correction, the energy of the electrons before the undulator was recorded for each shot, which is directly correlated to the photon energy of the FEL. A contour plot of the measured BXRTS spectral intensity as a function of electron energy is shown in the inset of Figure A.3. The peak of the scattered intensity, which is dominated by elastic scattering, as a function of electron energy, was fit using a linear regression with the best fit line shown in the inset of Figure A.3, with $E_{\text{photon}}(eV) = 604.9 E_{e^-}(\text{GeV}) - 2027$.

To remove the effect of electron energy jitter the photon energy of each detected photon was corrected according to this formula and centered at 1811 eV. This cor-

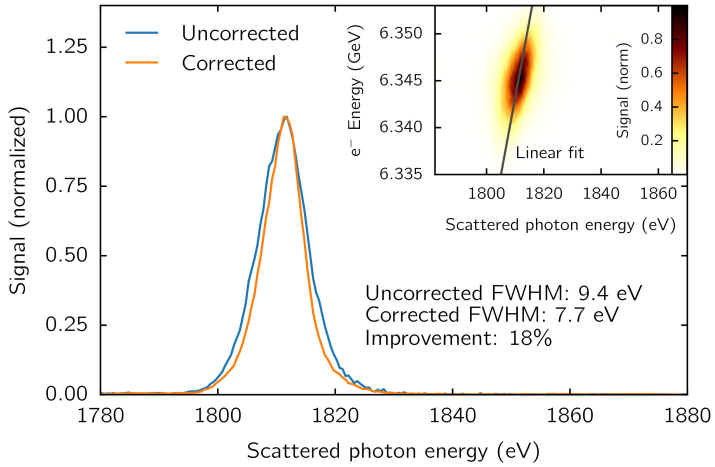

Figure A.3: Comparison of scattering spectra with and without input photon energy correction. The elastic peak of the scattering is a linear as a function of electron energy (inset), which can be used to correct for variations in probe photon energy.

rection reduced the full width at half maximum of the BXRTS spectrum by 18% (1.7 eV) as shown in Figure A.3.

A.5 High throughput data collection

A key requirement of this experiment was the ability to collect data at a high repetition rate to obtain scattering spectra with sufficient signal to noise. The experiment was conducted at 120 Hz, allowing the ∼150,000 shots required to obtain high-quality spectra to be obtained in 20-minute runs. By creating reduced data set files containing only the relevant parameters for each event, manageable files with files sizes ∼0.1% of the full data set were used for rapid analysis. These files contained key parameters such as the IR and FEL energies, timing information, and the pixel coordinate and ADU value for each detected photon.

Psana, the Python interface to the LCLS data system, was used to process the data. Each event produced ∼10 MB of data between the pnCCD image, time tool image, IR laser diagnostics, and other relevant parameters such as event identifiers

and stage positions. At 120 Hz, this translates to ∼72 GB/min or ∼1.4 TB per 20-minute run. In order to expedite analysis, selected pieces of the data were written to HDF5 files, while the full data set was written to the SLAC storage servers. For example, rather than save each pnCCD image to the HDF5 file, only the pixel coordinates and intensity of detected photons were saved. These reduced files were ∼140 MB per 20-minute run, or 0.1% of the full data set.

A.6 XRTS spectrum from cold argon clusters

Figure 4 shows the result for an XRTS spectrum from argon clusters at a scattering angle of 152°, integrated over 175,000 shots. On average, 1 photon is detected within the spectral window shown in Figure 4 every 2 shots. For this measurement the FEL was defocused to a 200 μm spot, delivering 0.25 mJ per shot onto the target. We estimate that on average an energy of 0.2 eV per atom is absorbed in the clusters, which can thus be considered cold. The data are shown on an absolute scale based on spectrometer efficiency and its spectral sensitivity [110]. The spectral bandwidth of 10 eV was chosen as it is close to the spectral resolution of the measurement (7.7 eV). The spectrum is fit using elastic scattering from bound electrons and an inelastic scattering contribution from ionization of M-shell electrons [111], where the ratio of elastic to inelastic scattering of 215 is found in the data. There is some uncertainty on the exact FEL spectrum in the lower wings of the elastic scattering profile. Here we assumed exponential functions that are consistent with the slope at high elastic scattering signal levels. This assumption might explain the deviation of the data from the fit at energies above 1835 eV. The noise floor for this measurement is almost four orders of magnitude below the peak signal. Because of the near background-free measurement, the noise floor could be further lowered by increasing the number of shots used for signal integration.

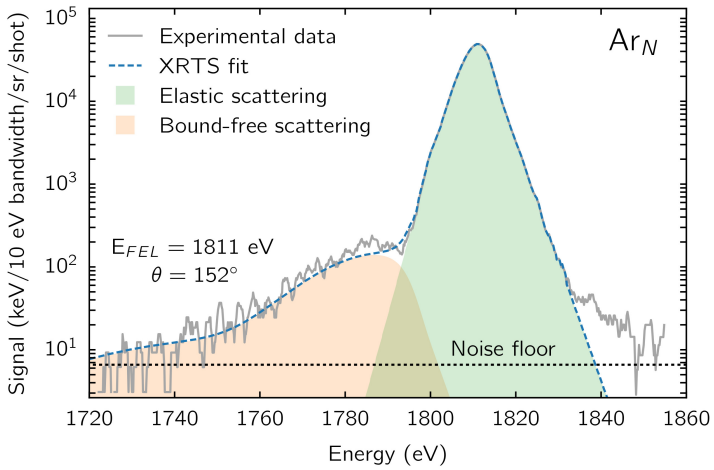

Figure A.4: Scattering spectrum at $\theta = 152°$ and fit from unheated Ar clusters demonstrating the ability to measure elastic and inelastic features with high-dynamic range using single photon counting and a high repetition rate system.

A.7 Conclusion

We have presented a proof-of-principle experiment to measure x-ray Thomson scattering from a cluster jet target at LCLS. Background signals were successfully mitigated by selecting a narrow range of ADU values from the energy-dispersive pnCCD detector. Despite a very low count rate, we demonstrated the ability to measure high-dynamic range scattering spectra with a clear inelastic scattering component from Ar clusters. XRTS spectra collected from laser-heated clusters will be analyzed using the method presented here to investigate the behavior of heated clusters on ultrafast timescales. These results show great promise for future experiments that will use XRTS to study laser-driven ionization and relaxation dynamics in clusters with sub-100 fs time resolution.

BIBLIOGRAPHY

BIBLIOGRAPHY

[1] N. Broll. Quantitative x-ray fluorescence analysis. Theory and practice of the fundamental coefficient method. *X-Ray Spectrometry*, 15(4):271–285, 1986.

[2] J. R. Asay and M. Shahinpoor. *High-pressure shock compression of solids*. Springer, 1993.

[3] R. P. Johnson. Results of Trident beam characterization 8/14/95 – 8/18/95. Technical Report P-24: 97-U-065, Los Alamos National Laboratory, 1997.

[4] M. Sanchez del Rio and R. J. Dejus. XOP v2.4: recent developments of the x-ray optics software toolkit. *Proceedings of SPIE*, 8141:814115, 2011.

[5] H. A. Scott. Cretin – radiative transfer capability for laboratory plasmas. *Journal of Quantitative Spectroscopy and Radiative Transfer*, 71(2–6):689–701, 2001.

[6] K. M. Ferrière. The interstellar environment of our galaxy. *Reviews of Modern Physics*, 73:1031–1066, 2001.

[7] I.-J. Sackmann, A. I. Boothroyd, and K. E. Kraemer. Our Sun. III. Present and future. *The Astrophysical Journal*, 418:457–468, 1993.

[8] J. D. Lindl, P. Amendt, R. L. Berger, S. G. Glendinning, S. H. Glenzer, S. W. Haan, R. L. Kauffman, O. L. Landen, and L. J. Suter. The physics basis for ignition using indirect-drive targets on the National Ignition Facility. *Physics of Plasmas*, 11(2):339–491, 2004.

[9] T. Guillot. Interiors of giant planets inside and outside the solar system. *Science*, 286(5437):72–77, 1999.

[10] S. Stanley and J. Bloxham. Convective-region geometry as the cause of Uranus' and Neptune's unusual magnetic fields. *Nature*, 428(6979):151–153, 2004.

[11] G. Kopp and J. L. Lean. A new, lower value of total solar irradiance: Evidence and climate significance. *Geophysical Research Letters*, 38(1):L01706, 2011.

[12] W. L. Barr, R. W. Moir, and G. W. Hamilton. Experimental results from a beam direct converter at 100 kV. *Journal of Fusion Energy*, 2(2):131–143, 1982.

[13] L. Coblentz. ITER Council endorses updated schedule focused on First Plasma. Press release, June 2016.

[14] J. Nuckolls, L. Wood, A. Thiessen, and G. Zimmerman. Laser compression of matter to super-high densities: Thermonuclear (CTR) applications. *Nature*, 239(5368):139–142, 1972.

[15] O. A. Hurricane, D. A. Callahan, D. T. Casey, E. L. Dewald, T. R. Dittrich, T. Döppner, M. A. Barrios Garcia, D. E. Hinkel, L. F. Berzak Hopkins, P. Kervin, J. L. Kline, S. L. Pape, T. Ma, A. G. MacPhee, J. L. Milovich, J. Moody, A. E. Pak, P. K. Patel, H.-S. Park, B. A. Remington, H. F. Robey, J. D. Salmonson, P. T. Springer, R. Tommasini, L. R. Benedetti, J. A. Caggiano, P. Celliers, C. Cerjan, R. Dylla-Spears, D. Edgell, M. J. Edwards, D. Fittinghoff, G. P. Grim, N. Guler, N. Izumi, J. A. Frenje, M. Gatu Johnson, S. Haan, R. Hatarik, H. Herrmann, S. Khan, J. Knauer, B. J. Kozioziemski, A. L. Kritcher, G. Kyrala, S. A. Maclaren, F. E. Merrill, P. Michel, J. Ralph, J. S. Ross, J. R. Rygg, M. B. Schneider, B. K. Spears, K. Widmann, and C. B. Yeamans. The high-foot implosion campaign on the National Ignition Facility. *Physics of Plasmas*, 21(5):056314, 2014.

[16] National Nuclear Security Administration. 2015 Review of the Inertial Confinement Fusion and High Energy Density Science Portfolio. Technical Report DOE/NA-0040, U. S. Department of Energy, 2016.

[17] P. K. Spiegel. The first clinical x-ray made in America–100 years. *American Journal of Roentgenology*, 164(1):241–243, 1995.

[18] J. Workman and G. A. Kyrala. Scaling of x-ray K-shell sources from laser-solid interactions. *Applications of x rays generated from lasers and other bright sources II*, 4504:168–179, 2001.

[19] C. Pellegrini, A. Marinelli, and S. Reiche. The physics of x-ray free-electron lasers. *Reviews of Modern Physics*, 88:015006, 2016.

[20] C. Bostedt, S. Boutet, D. M. Fritz, Z. Huang, H. J. Lee, H. T. Lemke, A. Robert, W. F. Schlotter, J. J. Turner, and G. J. Williams. Linac Coherent Light Source: The first five years. *Reviews of Modern Physics*, 88:015007, 2016.

[21] J. Amann, W. Berg, V. Blank, F. J. Decker, Y. Ding, P. Emma, Y. Feng, J. Frisch, D. Fritz, J. Hastings, Z. Huang, J. Krzywinski, R. Lindberg, H. Loos, A. Lutman, H. D. Nuhn, D. Ratner, J. Rzepiela, D. Shu, Y. Shvyd'ko, S. Spampinati, S. Stoupin, S. Terentyev, E. Trakhtenberg, D. Walz, J. Welch, J. Wu, A. Zholents, and D. Zhu. Demonstration of self-seeding in a hard-x-ray free-electron laser. *Nature Photonics*, 6(10):693–698, 2012.

[22] B. Nagler, B. Arnold, G. Bouchard, R. F. Boyce, R. M. Boyce, A. Callen, M. Campell, R. Curiel, E. Galtier, J. Garofoli, E. Granados, J. Hastings, G. Hays, P. Heimann, R. W. Lee, D. Milathianaki, L. Plummer, A. Schropp,

A. Wallace, M. Welch, W. White, Z. Xing, J. Yin, J. Young, U. Zastrau, and H. J. Lee. The Matter in Extreme Conditions instrument at the Linac Coherent Light Source. *Journal of Synchrotron Radiation*, 22(3):520–525, 2015.

[23] S. H. Glenzer, L. B. Fletcher, E. Galtier, B. Nagler, R. Alonso-Mori, B. Barbrel, S. B. Brown, D. A. Chapman, Z. Chen, C. B. Curry, F. Fiuza, E. Gamboa, M. Gauthier, D. O. Gericke, A. Gleason, S. Goede, E. Granados, P. Heimann, J. Kim, D. Kraus, M. J. MacDonald, A. J. Mackinnon, R. Mishra, A. Ravasio, C. Roedel, P. Sperling, W. Schumaker, Y. Y. Tsui, J. Vorberger, U. Zastrau, A. Fry, W. E. White, J. B. Hasting, and H. J. Lee. Matter under extreme conditions experiments at the Linac Coherent Light Source. *Journal of Physics B: Atomic, Molecular and Optical Physics*, 49(9):092001, 2016.

[24] R. P. Drake. *High-Energy-Density Physics*. Shock Wave and High Pressure Phenomena. Springer Berlin Heidelberg, 2006.

[25] D. Coster and R. D. L. Kronig. New type of Auger effect and its influence on the x-ray spectrum. *Physica*, 2(1):13–24, 1935.

[26] W. Bambynek, B. Crasemann, R. W. Fink, H.-U. Freund, H. Mark, C. D. Swift, R. E. Price, and P. V. Rao. X-ray fluorescence yields, Auger, and Coster-Kronig transition probabilities. *Reviews of Modern Physics*, 44:716–813, 1972.

[27] M. O. Krause. Atomic radiative and radiationless yields for K and L shells. *Journal of Physical and Chemical Reference Data*, 8(2):307–327, 1979.

[28] P. Glatzel and U. Bergmann. High resolution 1s core hole x-ray spectroscopy in 3d transition metal complexes—electronic and structural information. *Coordination Chemistry Reviews*, 249(1–2):65–95, 2005.

[29] S. H. Glenzer and R. Redmer. X-ray Thomson scattering in high energy density plasmas. *Reviews of Modern Physics*, 81:1625–1663, 2009.

[30] F. Coppari, R. F. Smith, J. H. Eggert, J. Wang, J. R. Rygg, A. Lazicki, J. A. Hawreliak, G. W. Collins, and T. S. Duffy. Experimental evidence for a phase transition in magnesium oxide at exoplanet pressures. *Nature Geoscience*, 6(11):926–929, 2013.

[31] A. E. Gleason, C. A. Bolme, H. J. Lee, B. Nagler, E. Galtier, D. Milathianaki, J. Hawreliak, R. G. Kraus, J. H. Eggert, D. E. Fratanduono, G. W. Collins, R. Sandberg, W. Yang, and W. L. Mao. Ultrafast visualization of crystallization and grain growth in shock-compressed SiO2. *Nature Communications*, 6:8191, 2015.

[32] D. Kraus, A. Ravasio, M. Gauthier, D. Gericke, J. Vorberger, S. Frydrych, J. Helfrich, L. Fletcher, G. Schaumann, B. Nagler, B. Barbrel, B. Bachmann,

E. Gamboa, S. Goede, E. Granados, G. Gregori, H. Lee, P. Neumayer, W. Schumaker, T. Doeppner, R. Falcone, S. Glenzer, and M. Roth. Nanosecond formation of diamond and lonsdaleite by shock compression of graphite. *Nature Communications*, 7:10970, accepted for publication, 2016.

[33] Y. B. Zel'dovich and Y. P. Raizer. *Physics of shock waves and high-temperature hydrodynamic phenomena*. Dover, 2002.

[34] J. W. Swegle and D. E. Grady. Shock viscosity and the prediction of shock wave rise times. *Journal of Applied Physics*, 58(2):692–701, 1985.

[35] S. Lyon and J. Johnson. SESAME: the Los Alamos National Laboratory equation of state database. *Los Alamos National Laboratory, Los Alamos, NM, LA-UR-92-3407*, 1992.

[36] P. Vinet, J. Ferrante, J. R. Smith, and J. H. Rose. A universal equation of state for solids. *Journal of Physics C: Solid State Physics*, 19(20):L467, 1986.

[37] P. Vinet, J. Ferrante, J. H. Rose, and J. R. Smith. Compressibility of solids. *Journal of Geophysical Research: Solid Earth*, 92(B9):9319–9325, 1987.

[38] D. K. Bradley, J. H. Eggert, R. F. Smith, S. T. Prisbrey, D. G. Hicks, D. G. Braun, J. Biener, A. V. Hamza, R. E. Rudd, and G. W. Collins. Diamond at 800 GPa. *Physical Review Letters*, 102:075503, 2009.

[39] C. M. Zener. *Elasticity and Anelasticity of Metals*. University of Chicago Press, Chicago, 1948.

[40] T. H. Courtney. *Mechanical Behavior of Materials*. Waveland Press, 2nd edition, 2005.

[41] W. Voigt. *Lehrbuch der kristallphysik*. Leipzig, Berlin, B.G. Teubner, 1928.

[42] A. Reuss. Berechnung der Fließgrenze von Mischkristallen auf Grund der Plastizitätsbedingung für Einkristalle. *Journal of Applied Mathematics and Mechanics*, 9(1):49–58, 1929.

[43] A. K. Singh. The lattice strains in a specimen (cubic system) compressed nonhydrostatically in an opposed anvil device. *Journal of Applied Physics*, 73(9):4278–4286, 1993.

[44] Y. Kato, K. Mima, N. Miyanaga, S. Arinaga, Y. Kitagawa, M. Nakatsuka, and C. Yamanaka. Random phasing of high-power lasers for uniform target acceleration and plasma-instability suppression. *Physical Review Letters*, 53:1057–1060, 1984.

[45] R. F. Smith, J. H. Eggert, R. Jeanloz, T. S. Duffy, D. G. Braun, J. R. Patterson, R. E. Rudd, J. Biener, A. E. Lazicki, A. V. Hamza, J. Wang, T. Braun, L. X. Benedict, P. M. Celliers, and G. W. Collins. Ramp compression of diamond to five terapascals. *Nature*, 511(7509):330–333, 2014.

[46] L. M. Barker and R. E. Hollenbach. Laser interferometer for measuring high velocities of any reflecting surface. *Journal of Applied Physics*, 43(11):4669–4675, 1972.

[47] L. M. Barker. The development of the VISAR, and its use in shock compression science. *AIP Conference Proceedings*, 505(1):11–18, 2000.

[48] B. E. Warren. *X-ray diffraction*. Dover, 1990.

[49] J. S. Wark, R. R. Whitlock, A. Hauer, J. E. Swain, and P. J. Solone. Shock launching in silicon studied with use of pulsed x-ray diffraction. *Physical Review B*, 35:9391–9394, 1987.

[50] U. Zastrau, E. J. Gamboa, D. Kraus, J. F. Benage, R. P. Drake, P. Efthimion, K. Falk, R. W. Falcone, L. B. Fletcher, E. Galtier, M. Gauthier, E. Granados, J. B. Hastings, P. Heimann, K. Hill, P. A. Keiter, J. Lu, M. J. MacDonald, D. S. Montgomery, B. Nagler, N. Pablant, A. Schropp, B. Tobias, D. O. Gericke, S. H. Glenzer, and H. J. Lee. Tracking the density evolution in counter-propagating shock waves using imaging x-ray scattering. *Applied Physics Letters*, 109(3):031108, 2016.

[51] E. Gamboa, P. Keiter, R. Drake, K. Falk, D. Montgomery, and J. Benage. Spatially-resolved x-ray scattering measurements of a planar blast wave. *High Energy Density Physics*, 11:75–79, 2014.

[52] M. J. MacDonald, P. A. Keiter, D. S. Montgomery, M. M. Biener, J. R. Fein, K. B. Fournier, E. J. Gamboa, S. R. Klein, C. C. Kuranz, H. J. LeFevre, M. J.-E. Manuel, J. Streit, W. C. Wan, and R. P. Drake. Demonstration of x-ray fluorescence imaging of a high-energy-density plasma. *Review of Scientific Instruments*, 85(11):11E602, 2014.

[53] M. J. MacDonald, J. Vorberger, E. J. Gamboa, R. P. Drake, S. H. Glenzer, and L. B. Fletcher. Calculation of Debye-Scherrer diffraction patterns from highly stressed polycrystalline materials. *Journal of Applied Physics*, 119(21):215902, 2016.

[54] M. Gauthier, L. B. Fletcher, A. Ravasio, E. Galtier, E. J. Gamboa, E. Granados, J. B. Hastings, P. Heimann, H. J. Lee, B. Nagler, A. Schropp, A. Gleason, T. Döppner, S. LePape, T. Ma, A. Pak, M. J. MacDonald, S. Ali, B. Barbrel, R. Falcone, D. Kraus, Z. Chen, M. Mo, M. Wei, and S. H. Glenzer. New experimental platform to study high density laser-compressed matter. *Review of Scientific Instruments*, 85(11):11E616, 2014.

[55] L. B. Fletcher, H. J. Lee, T. Döppner, E. Galtier, B. Nagler, P. Heimann, C. Fortmann, S. LePape, T. Ma, M. Millot, A. Pak, D. Turnbull, D. A. Chapman, D. O. Gericke, J. Vorberger, T. White, G. Gregori, M. Wei, B. Barbrel, R. W. Falcone, C. C. Kao, H. Nuhn, J. Welch, U. Zastrau, P. Neumayer, J. B. Hastings,

and S. H. Glenzer. Ultrabright x-ray laser scattering for dynamic warm dense matter physics. *Nature Photonics*, 9(4):274–279, 2015.

[56] A. Higginbotham and D. McGonegle. Prediction of Debye-Scherrer diffraction patterns in arbitrarily strained samples. *Journal of Applied Physics*, 115(17):174906, 2014.

[57] A. J. MacKinnon, N. B. Meezan, J. S. Ross, S. Le Pape, L. Berzak Hopkins, L. Divol, D. Ho, J. Milovich, A. Pak, J. Ralph, T. Döppner, P. K. Patel, C. Thomas, R. Tommasini, S. Haan, A. G. MacPhee, J. McNaney, J. Caggiano, R. Hatarik, R. Bionta, T. Ma, B. Spears, J. R. Rygg, L. R. Benedetti, R. P. J. Town, D. K. Bradley, E. L. Dewald, D. Fittinghoff, O. S. Jones, H. R. Robey, J. D. Moody, S. Khan, D. A. Callahan, A. Hamza, J. Biener, P. M. Celliers, D. G. Braun, D. J. Erskine, S. T. Prisbrey, R. J. Wallace, B. Kozioziemski, R. Dylla-Spears, J. Sater, G. Collins, E. Storm, W. Hsing, O. Landen, J. L. Atherton, J. D. Lindl, M. J. Edwards, J. A. Frenje, M. Gatu-Johnson, C. K. Li, R. Petrasso, H. Rinderknecht, M. Rosenberg, F. H. Séguin, A. Zylstra, J. P. Knauer, G. Grim, N. Guler, F. Merrill, R. Olson, G. A. Kyrala, J. D. Kilkenny, A. Nikroo, K. Moreno, D. E. Hoover, C. Wild, and E. Werner. High-density carbon ablator experiments on the National Ignition Facility. *Physics of Plasmas*, 21(5):056318, 2014.

[58] M. Ross. The ice layer in Uranus and Neptune - diamonds in the sky. *Nature*, 292(5822):435–436, 1981.

[59] K.-i. Kondo and T. J. Ahrens. Shock compression of diamond crystal. *Geophysical Research Letters*, 10(4):281–284, 1983.

[60] M. D. Knudson, M. P. Desjarlais, and D. H. Dolan. Shock-wave exploration of the high-pressure phases of carbon. *Science*, 322(5909):1822–1825, 2008.

[61] R. S. McWilliams, J. H. Eggert, D. G. Hicks, D. K. Bradley, P. M. Celliers, D. K. Spaulding, T. R. Boehly, G. W. Collins, and R. Jeanloz. Strength effects in diamond under shock compression from 0.1 to 1 TPa. *Physical Review B*, 81:014111, 2010.

[62] X. Gonze, B. Amadon, P.-M. Anglade, J.-M. Beuken, F. Bottin, P. Boulanger, F. Bruneval, D. Caliste, R. Caracas, M. Côté, T. Deutsch, L. Genovese, P. Ghosez, M. Giantomassi, S. Goedecker, D. Hamann, P. Hermet, F. Jollet, G. Jomard, S. Leroux, M. Mancini, S. Mazevet, M. Oliveira, G. Onida, Y. Pouillon, T. Rangel, G.-M. Rignanese, D. Sangalli, R. Shaltaf, M. Torrent, M. Verstraete, G. Zerah, and J. Zwanziger. ABINIT: First-principles approach to material and nanosystem properties. *Computer Physics Communications*, 180(12):2582–2615, 2009.

[63] F. Bottin, S. Leroux, A. Knyazev, and G. Zerah. Large-scale ab initio calculations based on three levels of parallelization. *Computational Materials Science*, 42(2):329–336, 2008.

[64] D. R. Hamann, X. Wu, K. M. Rabe, and D. Vanderbilt. Metric tensor formulation of strain in density-functional perturbation theory. *Physical Review B*, 71:035117, 2005.

[65] M. Fuchs and M. Scheffler. Ab initio pseudopotentials for electronic structure calculations of poly-atomic systems using density-functional theory. *Computer Physics Communications*, 119(1):67–98, 1999.

[66] J. P. Perdew, K. Burke, and M. Ernzerhof. Generalized gradient approximation made simple. *Physical Review Letters*, 77:3865–3868, 1996.

[67] H.-R. Wenk and P. V. Houtte. Texture and anisotropy. *Reports on Progress in Physics*, 67(8):1367, 2004.

[68] D. McGonegle, D. Milathianaki, B. A. Remington, J. S. Wark, and A. Higginbotham. Simulations of in situ x-ray diffraction from uniaxially compressed highly textured polycrystalline targets. *Journal of Applied Physics*, 118(6):065902, 2015.

[69] D. C. Swift and R. G. Kraus. Properties of plastic ablators in laser-driven material dynamics experiments. *Physical Review E*, 77:066402, 2008.

[70] P. Hart, S. Boutet, G. Carini, M. Dubrovin, B. Duda, D. Fritz, G. Haller, R. Herbst, S. Herrmann, C. Kenney, N. Kurita, H. Lemke, M. Messerschmidt, M. Nordby, J. Pines, D. Schafer, M. Swift, M. Weaver, G. Williams, D. Zhu, N. van Bakel, and J. Morse. The CSPAD megapixel x-ray camera at LCLS. *Proceedings of SPIE*, 8504, 2012.

[71] S. Herrmann, S. Boutet, B. Duda, D. Fritz, G. Haller, P. Hart, R. Herbst, C. Kenney, H. Lemke, M. Messerschmidt, J. Pines, A. Robert, M. Sikorski, and G. Williams. CSPAD-140k: A versatile detector for LCLS experiments. *Nuclear Instruments and Methods in Physics Research A*, 718:550–553, 2013.

[72] E. J. Gamboa. *Spatially-resolved x-ray scattering experiments*. PhD thesis, University of Michigan, 2013.

[73] M. J. MacDonald, P. A. Keiter, D. S. Montgomery, H. A. Scott, M. M. Biener, J. R. Fein, K. B. Fournier, E. J. Gamboa, G. E. Kemp, S. R. Klein, C. C. Kuranz, H. J. LeFevre, M. J.-E. Manuel, W. C. Wan, , and R. P. Drake. Spatially resolved density and ionization measurements of shocked foams using x-ray fluorescence. *Journal of Applied Physics*, 2016 (in press).

[74] D. Ryutov, R. P. Drake, J. Kane, E. Liang, B. A. Remington, and W. M. Wood-Vasey. Similarity criteria for the laboratory simulation of supernova hydrodynamics. *The Astrophysical Journal*, 518(2):821, 1999.

[75] N. C. Holmes, H. B. Radousky, M. J. Moss, W. J. Nellis, and S. Henning. Silica at ultrahigh temperature and expanded volume. *Applied Physics Letters*, 45(6):626–628, 1984.

[76] N. C. Holmes. Equation-of-state measurements of low-density materials. *Review of Scientific Instruments*, 62(8):1990–1994, 1991.

[77] M. Koenig, A. Benuzzi, F. Philippe, D. Batani, T. Hall, N. Grandjouan, and W. Nazarov. Equation of state data experiments for plastic foams using smoothed laser beams. *Physics of Plasmas*, 6(8):3296–3301, 1999.

[78] D. Hoarty, A. Iwase, C. Meyer, J. Edwards, and O. Willi. Characterization of laser driven shocks in low density foam targets. *Physical Review Letters*, 78:3322–3325, 1997.

[79] M. D. Knudson and R. W. Lemke. Shock response of low-density silica aerogel in the multi-Mbar regime. *Journal of Applied Physics*, 114(5):053510, 2013.

[80] K. Falk, C. A. McCoy, C. L. Fryer, C. W. Greeff, A. L. Hungerford, D. S. Montgomery, D. W. Schmidt, D. G. Sheppard, J. R. Williams, T. R. Boehly, and J. F. Benage. Temperature measurements of shocked silica aerogel foam. *Physical Review E*, 90:033107, 2014.

[81] R. Tertian and F. Claisse. *Principles of quantitative x-ray fluorescence analysis*. Heyden, 1982.

[82] L. J. Suter, O. L. Landen, and J. I. Koch. Prospects for fluorescence based imaging/visualization of hydrodynamic systems on the National Ignition Facility. *Review of Scientific Instruments*, 70(1):663, 1999.

[83] N. E. Lanier, C. W. Barnes, R. Perea, and W. Steckle. Feasibility of fluorescence-based imaging of high-energy-density hydrodynamics experiments. *Review of Scientific Instruments*, 74(3):2169, 2003.

[84] L. C. Jarrott, M. S. Wei, C. McGuffey, A. A. Solodov, W. Theobald, B. Qiao, C. Stoeckl, R. Betti, H. Chen, J. Delettrez, T. Doppner, E. M. Giraldez, V. Y. Glebov, H. Habara, T. Iwawaki, M. H. Key, R. W. Luo, F. J. Marshall, H. S. McLean, C. Mileham, P. K. Patel, J. J. Santos, H. Sawada, R. B. Stephens, T. Yabuuchi, and F. N. Beg. Visualizing fast electron energy transport into laser-compressed high-density fast-ignition targets. *Nature Physics*, 12(5):499–504, 2016.

[85] D. J. Hoarty, C. C. Smith, E. L. Clark, J. M. Foster, S. G. Gales, G. Magelssen, J. Workman, W. M. Wood, S. Caldwell, R. Chrien, J. Sandoval, T. Sedillo, P. Walsh, B. Carpenter, S. Compton, and T. Perry. Fluorescence spectroscopy as a diagnostic of the radiation environment in high energy density experiments. *Review of Scientific Instruments*, 75(10):3655, 2004.

[86] G. Gregori, S. B. Hansen, R. Clarke, R. Heathcote, M. H. Key, J. King, R. I. Klein, N. Izumi, A. J. Mackinnon, S. J. Moon, H.-S. Park, J. Pasley, N. Patel, P. K. Patel, B. A. Remington, D. D. Ryutov, R. Shepherd, R. A. Snavely, S. C. Wilks, B. B. Zhang, and S. H. Glenzer. Experimental characterization of a

strongly coupled solid density plasma generated in a short-pulse laser target interaction. *Contributions to Plasma Physics*, 45(3-4):284–292, 2005.

[87] S. Hansen, a. Faenov, T. Pikuz, K. Fournier, R. Shepherd, H. Chen, K. Widmann, S. Wilks, Y. Ping, H. Chung, a. Niles, J. Hunter, G. Dyer, and T. Ditmire. Temperature determination using Kα spectra from M-shell Ti ions. *Physical Review E*, 72(3):036408, 2005.

[88] S. N. Chen, G. Gregori, P. K. Patel, H.-K. Chung, R. G. Evans, R. R. Freeman, E. Garcia Saiz, S. H. Glenzer, S. B. Hansen, F. Y. Khattak, J. A. King, A. J. Mackinnon, M. M. Notley, J. R. Pasley, D. Riley, R. B. Stephens, R. L. Weber, S. C. Wilks, and F. N. Beg. Creation of hot dense matter in short-pulse laser-plasma interaction with tamped titanium foils. *Physics of Plasmas*, 14(10):102701, 2007.

[89] P. Neumayer, H. Lee, D. Offerman, E. Shipton, A. Kemp, A. Kritcher, T. Döppner, C. Back, and S. Glenzer. Isochoric heating of reduced mass targets by ultra-intense laser produced relativistic electrons. *High Energy Density Physics*, 5(4):244–248, 2009.

[90] U. Zastrau, A. Sengebusch, P. Audebert, E. Brambrink, R. Fäustlin, T. Kämpfer, E. Kroupp, R. Loetzsch, Y. Maron, H. Reinholz, G. Röpke, E. Stambulchik, I. Uschmann, and E. Förster. High-resolution radial Kα spectra obtained from a multi-keV electron distribution in solid-density titanium foils generated by relativistic laser–matter interaction. *High Energy Density Physics*, 7(2):47–53, 2011.

[91] M. Berger, J. Hubbell, S. Seltzer, J. Chang, J. Coursey, R. Sukumar, D. Zucker, and K. Olsen. XCOM: Photon cross sections database, 2012.

[92] M. M. Biener, J. Biener, Y. M. Wang, S. J. Shin, I. C. Tran, T. M. Willey, F. N. Pérez, J. F. Poco, S. a. Gammon, K. B. Fournier, A. W. van Buuren, J. H. Satcher, and A. V. Hamza. Atomic layer deposition-derived ultra-low-density composite bulk materials with deterministic density and composition. *ACS applied materials & interfaces*, 5(24):13129–13134, 2013.

[93] E. J. Gamboa, D. S. Montgomery, I. M. Hall, and R. P. Drake. Imaging x-ray crystal spectrometer for laser-produced plasmas. *Journal of Instrumentation*, 6(04):P04004, 2011.

[94] J. T. Larsen and S. M. Lane. HYADES—A plasma hydrodynamics code for dense plasma studies. *Journal of Quantitative Spectroscopy and Radiative Transfer*, 51(1-2):179–186, 1994.

[95] H. Scott and S. Hansen. Advances in NLTE modeling for integrated simulations. *High Energy Density Physics*, 6(1):39–47, 2010.

[96] M. F. Gu. The flexible atomic code. *Canadian Journal of Physics*, 86(5):675–689, 2008.

[97] M. J. Grosskopf, R. P. Drake, C. C. Kuranz, A. R. Miles, J. F. Hansen, T. Plewa, N. Hearn, D. Arnett, and J. C. Wheeler. Modeling of multi-interface, diverging, hydrodynamic experiments for the National Ignition Facility. *Astrophysics and Space Science*, 322(1):57–63, 2008.

[98] C. Stoeckl, G. Fiksel, D. Guy, C. Mileham, P. M. Nilson, T. C. Sangster, M. J. Shoup, and W. Theobald. A spherical crystal imager for OMEGA EP. *Review of Scientific Instruments*, 83(3):033107, 2012.

[99] T. Ditmire, R. A. Smith, J. W. G. Tisch, and M. H. R. Hutchinson. High intensity laser absorption by gases of atomic clusters. *Physical Review Letters*, 78:3121–3124, 1997.

[100] T. Fennel, K.-H. Meiwes-Broer, J. Tiggesbäumker, P.-G. Reinhard, P. M. Dinh, and E. Suraud. Laser-driven nonlinear cluster dynamics. *Reviews of Modern Physics*, 82:1793–1842, 2010.

[101] T. Fennel, T. Döppner, J. Passig, C. Schaal, J. Tiggesbäumker, and K.-H. Meiwes-Broer. Plasmon-enhanced electron acceleration in intense laser metal-cluster interactions. *Physical Review Letters*, 98:143401, 2007.

[102] T. Döppner, T. Fennel, T. Diederich, J. Tiggesbäumker, and K. H. Meiwes-Broer. Controlling the coulomb explosion of silver clusters by femtosecond dual-pulse laser excitation. *Physical Review Letters*, 94:013401, 2005.

[103] C. Bostedt, E. Eremina, D. Rupp, M. Adolph, H. Thomas, M. Hoener, A. R. B. de Castro, J. Tiggesbäumker, K.-H. Meiwes-Broer, T. Laarmann, H. Wabnitz, E. Plönjes, R. Treusch, J. R. Schneider, and T. Möller. Ultrafast x-ray scattering of xenon nanoparticles: Imaging transient states of matter. *Physical Review Letters*, 108:093401, 2012.

[104] L. Strüder, S. Epp, D. Rolles, R. Hartmann, P. Holl, G. Lutz, H. Soltau, R. Eckart, C. Reich, K. Heinzinger, C. Thamm, A. Rudenko, F. Krasniqi, K.-U. Kühnel, C. Bauer, C.-D. Schröter, R. Moshammer, S. Techert, D. Miessner, M. Porro, O. Hälker, N. Meidinger, N. Kimmel, R. Andritschke, F. Schopper, G. Weidenspointner, A. Ziegler, D. Pietschner, S. Herrmann, U. Pietsch, A. Walenta, W. Leitenberger, C. Bostedt, T. Möller, D. Rupp, M. Adolph, H. Graafsma, H. Hirsemann, K. Gärtner, R. Richter, L. Foucar, R. L. Shoeman, I. Schlichting, and J. Ullrich. Large-format, high-speed, X-ray pnCCDs combined with electron and ion imaging spectrometers in a multipurpose chamber for experiments at 4th generation light sources. *Nuclear Instruments and Methods in Physics Research A*, 614(3):483–496, 2010.

[105] D. J. Bozek. AMO instrumentation for the LCLS X-ray FEL. *European Physical Journal*, 169(1):129–132, 2009.

[106] K. R. Ferguson, M. Bucher, J. D. Bozek, S. Carron, J.-C. Castagna, R. Coffee, G. I. Curiel, M. Holmes, J. Krzywinski, M. Messerschmidt, M. Minitti, A. Mitra, S. Moeller, P. Noonan, T. Osipov, S. Schorb, M. Swiggers, A. Wallace, J. Yin, and C. Bostedt. The Atomic, Molecular and Optical Science instrument at the Linac Coherent Light Source. *Journal of Synchrotron Radiation*, 22(3):492–497, 2015.

[107] P. Emma, R. Akre, J. Arthur, R. Bionta, C. Bostedt, J. Bozek, A. Brachmann, P. Bucksbaum, R. Coffee, F. J. Decker, Y. Ding, D. Dowell, S. Edstrom, A. Fisher, J. Frisch, S. Gilevich, J. Hastings, G. Hays, P. Hering, Z. Huang, R. Iverson, H. Loos, M. Messerschmidt, A. Miahnahri, S. Moeller, H. D. Nuhn, G. Pile, D. Ratner, J. Rzepiela, D. Schultz, T. Smith, P. Stefan, H. Tompkins, J. Turner, J. Welch, W. White, J. Wu, G. Yocky, and J. Galayda. First lasing and operation of an angstrom-wavelength free-electron laser. *Nature Photonics*, 4(9):641–647, 2010.

[108] U. Even. Pulsed supersonic beams from high pressure source: Simulation results and experimental measurements. *Advances in Chemistry*, 2014:636042, 2014.

[109] M. Harmand, R. Coffee, M. R. Bionta, M. Chollet, D. French, D. Zhu, D. M. Fritz, H. T. Lemke, N. Medvedev, B. Ziaja, S. Toleikis, and M. Cammarata. Achieving few-femtosecond time-sorting at hard x-ray free-electron lasers. *Nature Photonics*, 7(3):215–218, 2013.

[110] E. Gamboa, B. Bachmann, D. Kraus, M. MacDonald, M. Bucher, S. Carron, R. Coffee, R. Drake, J. Emig, K. Ferguson, S. Glenzer, T. Gorkhover, S. Hau-Riege, J. Krzywinski, A. Levitan, K.-H. Meiwes-Broer, T. Osipov, T. Pardini, C. Peltz, S. Skruszewicz, C. Bostedt, T. Fennel, and T. Döppner. Dual crystal x-ray spectrometer at 1.8 keV for high repetition-rate single-photon counting spectroscopy experiments. *Journal of Instrumentation*, 11(08):P08015, 2016.

[111] G. Gregori, S. H. Glenzer, F. J. Rogers, S. M. Pollaine, O. L. Landen, C. Blancard, G. Faussurier, P. Renaudin, S. Kuhlbrodt, and R. Redmer. Electronic structure measurements of dense plasmas. *Physics of Plasmas*, 11(5):2754–2762, 2004.